

***PHOTON FACTORY
ACTIVITY REPORT***

1986

#4



NATIONAL LABORATORY FOR HIGH ENERGY PHYSICS, KEK

PHOTON FACTORY ACTIVITY REPORT

1 9 8 6



Editorial Board

ANAMI Shozo

KITAMURA Hideo

SAKABE Noriyoshi*

(*Chief editor)

KEK Progress Report 86-3

©National Laboratory for High Energy Physics, 1987

KEK Reports are available from

Technical Information Office

National Laboratory for High Energy Physics

Oho-machi, Tsukuba-gun

Ibaraki-Ken, 305

JAPAN

Phone : 0298-64-1171

Telex : 3652-534 (Domestic)

(0) 3652-534 (International)

Cable : KEKOH0

You can jump to the article by clicking its title.

Contents

Preface	5
Outline of the Photon Factory	
1. Introduction	10
2. Plan of the facility	10
3. Organization and staff	10
4. Budget	15
5. Operation time and proposal	15
6. List of Proposals	18
6.1 Proposals accepted by Program Advisory Committee	
6.2 Proposals accepted for charged beam time assessment	
7. PF seminars, meetings and publications	28
Injector Linac Department	
1. Introduction	33
2. Operation of the positron beam	35
2.1 Outline of operation	
2.2 The positron generator	
2.3 Positron acceleration in the PF 2.5-GeV linac	
2.4 Injection to the AR	
2.5 Beam switchover	
2.6 Further improvement of the positron beam	
3. Electron Linac	38
3.1 Operational status of microwave source	
3.2 Phase control	
3.3 Developments	
4. Positron Generator	47
4.1 Progress of the beam acceleration	
4.2 Injection system	
4.3 Control system	
Light source Department	
1. Introduction	55
2. Storage ring	56
2.1 Operation	
2.2 Storage of positron beam	
2.3 Beam studies	
2.4 Improvements of the vacuum system and their results	
2.5 Beam monitoring	
2.6 Control	
3. Beam channel	75
3.1 General	
3.2 New beam channels	
4. Insertion devices	78
4.1 General	
4.2 Operation of B02 undulator	
4.3 Superconducting vertical wiggler	
Instrumentation Department	
1. Beam lines and optics	87
1.1 Beam lines	
1.2 Optics	
1.3 Summary of X-ray beam lines and optics	94
1.4 Summary of VUV/soft X-ray beam lines and optics	95
2. List of apparatus	96
User's short reports	
1. Content for experimental progress reports	100
2. Experimental progress reports	114
Author index	333
Subject index	336
List of publications	340

PREFACE

The Photon Factory was commissioned in 1982 as a facility dedicated to use of synchrotron radiation; then, TRISTAN, a positron-electron collider, was constructed at full scale. TRISTAN began to operate in the middle of October 1986: the world's highest-energy electron and positron collisions were achieved at an energy of 25.5 GeV on October 24, 10 days after its test operation started. The distinctive feature of KEK's plan is that projects involving both high-energy physics and the use of synchrotron radiation were considered as an inclusive plan from the start. Both projects have proceeded in close relation, including the exchange of accelerator crew members as well as scientific ideas. This relationship has led to economic and scientific mutual benefits.

During the past three years, efforts of the Photon Factory (PF) staff have been concentrated on the stable operation of the accelerator, construction of beam lines and development of instrumentation for use of synchrotron radiation. The accelerator crew has achieved stable machine operation; 30 % of the total operation hours has been devoted to a study of the machine itself.

The total operation time was limited by the FY-1986 budget to 2800 hours, an increase of 200 hours over that of the previous fiscal year. The number of users (from many universities and governmental institutes) has amounted to 1300 registrations; 253 of the proposed experiments were under way during 1986. Participation from industry has become popular. During FY-1985 a total of 1238 station-hours were devoted to 24 experiments which were carried out by participants during 1108 man-days.

The joint research programs between KEK and such industrial companies as Fujitsu, Hitachi, Mitsubishi, Nippon Electric Company (NEC), Sanyo, Shin-Nittetsu, Sony and Toshiba were also expanded: five programs were executed in 1984, eight in 1985, and now fifteen programs are running involving such subjects as the characterization of semiconductor materials, surface-structure analyses, photochemical reactions, trace impurity analyses, and in-situ observations of crystal growth defects.

Such a busy experimental schedule has been carried out smoothly under the leadership of the new director of the Instrumentation Department, Professor Hiroshi Iwasaki, who moved from Tohoku University. Reflecting the busy program, the number of staff members increased to 78 during 1986 (62 in 1984, 68 in 1985).

The fourth annual users' meeting was held with more than 250 participants on November 7 and 8, 1986. Six invited papers and 156 poster-sessions papers were presented.

We are now at a point at which we can consider an improvement of the performance and future plans of the PF. Improvement of the

machine is under way according to the following strategy: (1) stabilization of beam positions, (2) low-emittance operation of the ring, (3) insertion of undulators and multipole-wigglers, and (4) storage of positrons in the ring (test operation was undertaken at the end of 1985). The linear accelerator is now supplying a positron beam with a current of 10 mA at 2.5 GeV for TRISTAN experiments. To operate the PF ring with positrons at a sufficiently high current, the injection rate will be increased in the near future.

From their experiences with the PF ring, most of the users are now seeking high-brilliance light sources in all spectral ranges. Workshop on future plans were held three times during 1986 which included hot discussions concentrated on demands for next-generation machines. Especially, needs for powerful hard X-ray sources are rapidly increasing. Therefore, an accumulation ring (6-8 GeV) for the TRISTAN has been planned to be used for this purpose. Two beam lines with undulators will be constructed during 1987 to 1988 in the experimental hall located in the north-east section of the ring and will serve for the study of Compton scattering, magnetic scattering, structure analyses under high pressures, surface and interface structures and so on. This project involves an improvement of the emittance for the ring. Such experiences involving the 6- GeV ring are expected to be useful for the development of new machines.

It was with great sorrow that we received news that Professor T. Sagawa of Tohoku University, a member of the Advisory Council for the PF, passed away on September 27 of 1986. He had been one of the most prominent leaders since the beginning of the PF project. On behalf of all the PF staff members and users, I would like to express our deep appreciation for his contribution and regret for his death.

We would like to acknowledge the cooperation of visitors from laboratories abroad: Prof. A. Bianconi from the University of Rome, Prof. R. Chehab from the University of Paris-Sud, Dr. M. Kuriyama from NBS and Dr. J.-P. M. Pouget from CNRS. Their valuable interactions with the PF staff have been greatly appreciated.

The 3rd International Conference on X-Ray and VUV Synchrotron Radiation Instrumentation, SRI-88, will be held at the end of August, 1988, at Tsukuba. This conference will serve as a forum for future plans as well as new developments in synchrotron radiation instrumentation. All scientists and engineers working with synchrotron radiation around the world are welcome to Tsukuba.



Jun-ichi Chikawa
Director

Outline of the Photon Factory

History of Photon Factory

- 1971 KEK was established and the construction of a 12-GeV proton synchrotron was started. The Crystallography Group organized a workshop on "High Power X-ray Generators", high-energy storage rings were found to be the most powerful. This group requested the cooperation of the High Energy Accelerator Group.
- 1972 The High Energy Accelerator Group of the Institute for Nuclear Study of the University of Tokyo (INS) started to design electron accelerators, including X-ray and stretcher rings. During the preliminary design period, the project called "Photon Factory" (PF) was selected.
- 1973 The PF community was organized. KEK started a TRISTAN workshop.
- 1974 The Science Council of Japan recommended to the government the establishment of the PF.
- 1975 The PF community requested the cooperation of KEK.
- 1976 The 12-GeV KEK proton synchrotron was commissioned.
- 1977 The Feasibility Study Committee for the PF was established at KEK.
- 1978 The government approved the PF construction at KEK.
- 1979 A ground-breaking ceremony was held in January.
- 1981 The linac produced its first beam with an energy of 0.5 GeV. The TRISTAN Project was approved at KEK and the construction of the Accumulation Ring (AR) started.
- 1982 In March, the linac energy was increased to 2.5 GeV and the PF ring stored 2.5-GeV electron beams. In July, experiments using SR (synchrotron radiation) were commissioned. The construction of the main ring (30 GeV) of TRISTAN started.
- 1983 A PF undulator with 120 poles was commissioned. The TRISTAN accumulation ring stored and accelerated electrons to 6 GeV.
- 1983 A PF superconducting vertical wiggler was commissioned.
- 1985 The first SR channel was installed in the AR. The positron source was completed. The linac accelerated positrons to 2.5 GeV. The injection of positrons into both the AR and the PF ring was successful.
- 1986 The SR channel of the AR was commissioned.

OUTLINE OF THE PHOTON FACTORY

1. INTRODUCTION

The Photon Factory (PF) is a national synchrotron radiation research facility affiliated with the National Laboratory for High Energy Physics, or KEK, operated by the Ministry of Education, Science and Culture. It comprises a 2.5-GeV electron linear accelerator, 2.5-GeV electron storage ring as a dedicated light source, and beam-lines and experimental stations for exploiting synchrotron radiation, in studies involving such fields as physics, chemistry, biology, medical science, pharmacology, geology and lithography. All of the facilities for synchrotron radiation research are open to scientists from universities and research institutes belonging to the government, public organizations, private enterprises and those of foreign countries. Institutions affiliated with the Ministry of Education, Science and Culture are given the highest priority as users. Applications from other organizations are also admitted with or without charge, depending upon the category of their objectives.

The Photon Factory is located at the northern most end of the Tsukuba Science City, about 60 km north-east of Tokyo. Here, many governmental research institutes are assembled within an area equivalent to down-town Tokyo, forming a unique community of modern science and technology.

2. PLAN OF THE FACILITY

A plan which includes the accelerator complex is shown in Fig. 1. A long housing for the 450-m linear accelerator is connected to the storage ring building through a 150-m underground beam-transport tunnel. A view of the experimental hall is shown in Fig. 2, including the magnet arrangement of the ring. Twelve beam lines are in operation and three lines are under construction. Thirty four experimental stations are available for users.

The yearly increases in the number of beam channels from the beginning of the PF are listed in Table 1. Fifteen of the channels have already been used (Fig. 2). Beam lines BL5 and BL19, for which channels have already been built, are waits to start the construction of hutches now under construction.

Table 1 Yearly account of beam channels

Period	Number of Beam Channels			Total
	PF	Institute	Industry	
FY1981	6	0	0	6
FY1982	8	0	0	8
FY1983	8	0	1	9
FY1984	8	1	2	11
FY1985	10	1	4	15
FY1986	12	1	4	17

Beam lines BL1, BL8, BL9 and BL17 were constructed by Nippon Telephone and Telegram (NTT), Hitachi Corporation, Nippon Electric Company (NEC) and Fujitsu Corporation LABS, respectively. BL7A and BL7B were built by the Research Center for Spectrochemistry (RCS), the University of Tokyo. The other beam lines were constructed by the PF's own fund.

3. ORGANIZATION AND STAFF

The organizational structure of KEK is shown in Fig. 3. The PF consists of three departments: Injector Linac, Light Source and Instrumentation. Details concerning the organizational structure and the staff of the PF are shown in Fig. 4. Also, the number of staff and visiting scientist from the beginning of the PF are listed in Table 2.

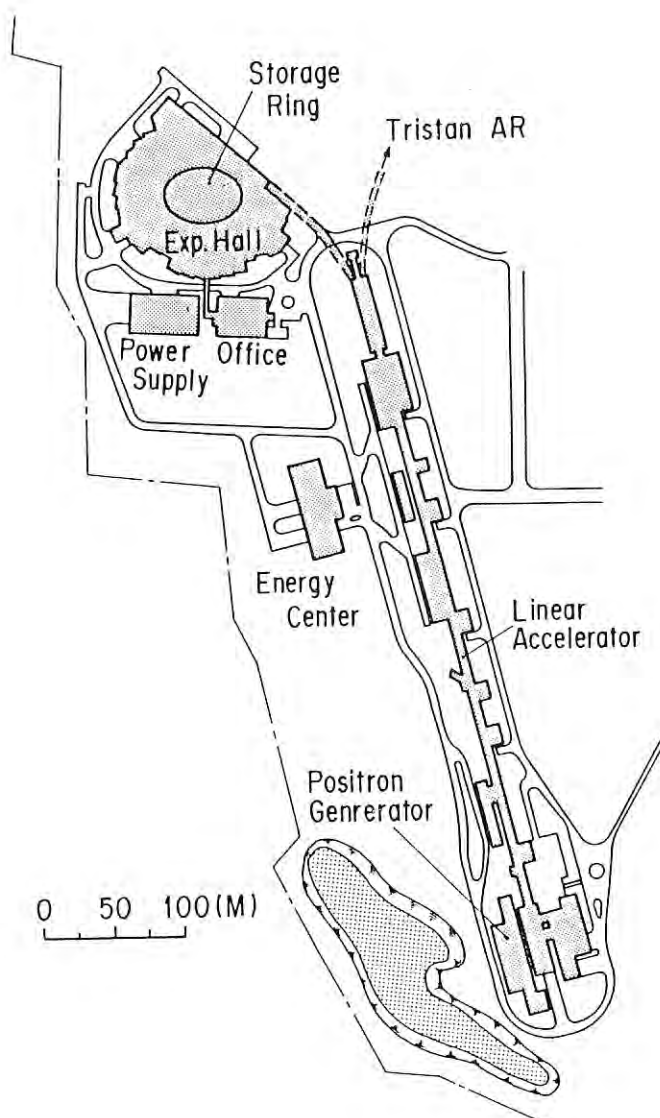
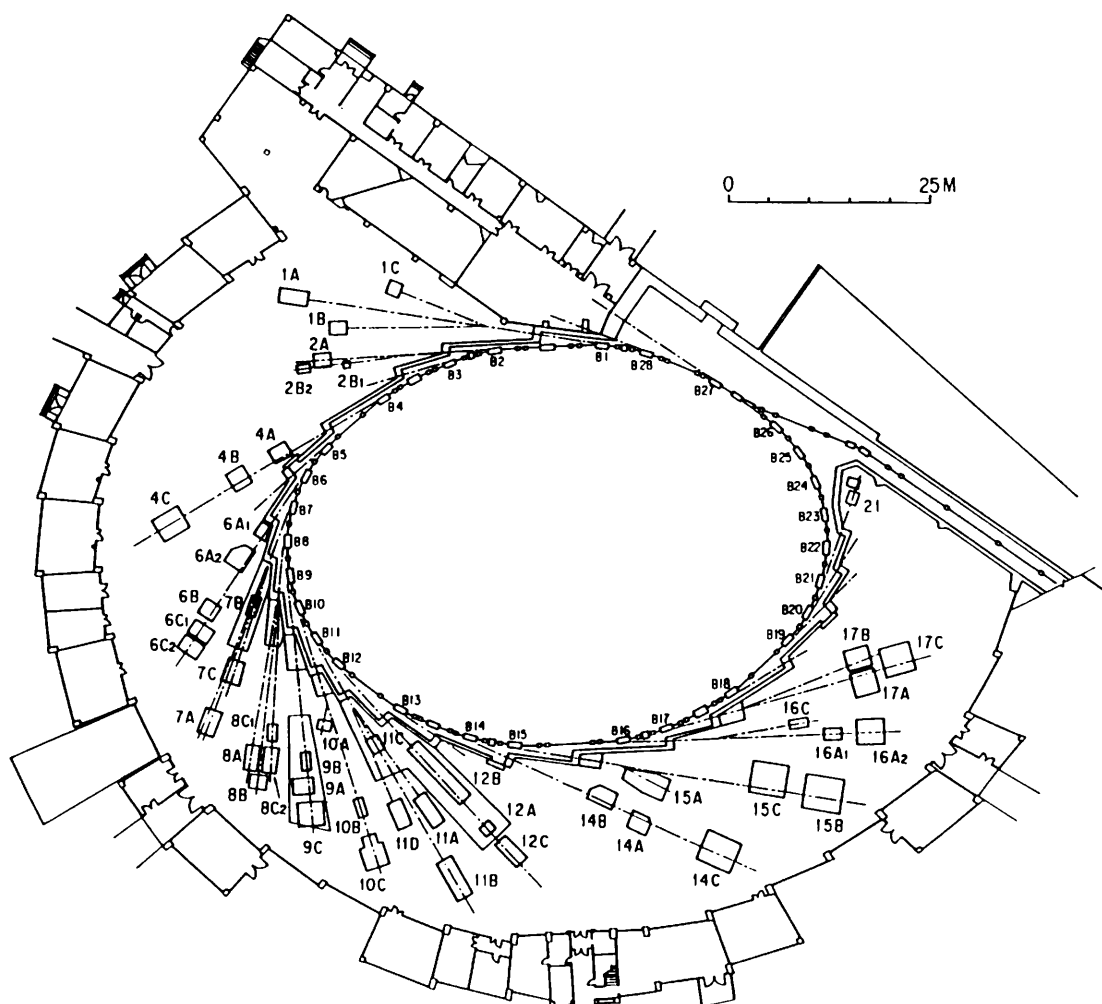


Fig. 1 Plan of the Photon Factory.



- | | |
|--|--|
| 1A : Solid Surface Analysis | 10B : EXAFS |
| 1B : X-ray Lithography | 10C : Small Angle X-ray Scattering (Enzyme) |
| 1C : Photo-Chemical Reaction Experiment | Fluorescent EXAFS |
| 2A : Undulator Experiment | X-ray Diffuse Scattering |
| 2B ₁ : Fresnel Zone Plate Microscope | 11A : Soft X-ray Solid State Spectroscopy |
| 2B ₂ : Soft X-ray Gas Spectroscopy | (2 m Grasshopper) |
| (10 m Grazing Incidence) | 11B : Soft X-ray Double Crystal Monochromator |
| 4A : Dispersive EXAFS | 11C : VUV Solid State Spectroscopy |
| Ultra-Trace Element Analysis | (1 m Seya-Namioka) |
| Radiation Biology Experiment | 11D : Angle-Resolved Photoemission Spectroscopy |
| 4B : X-ray Diffraction by Liquid and Melt | (Constant Deviation) |
| X-ray Camera | 12A : VUV Gas Spectroscopy |
| 4C : X-ray Diffraction under High Pressure | (1 m Seya-Namioka) |
| X-ray Diffraction at Low Temperature | 12B : VUV High Resolution Spectroscopy |
| 6A ₁ : High Resolution Small Angle Scattering | (6VOPE: 6.65 m Vertical Dispersion Off-plane |
| (under Construction) | Eagle Spectrograph/Monochromator) |
| 6A ₂ : Protein Structure Analysis Using Camera Method | 12C : VUV White Line |
| (under Construction) | 14A : Crystal Structure Analysis (Proteins) |
| 6B : EXAFS (under Construction) | EXAFS at High Photon Energy |
| 6C ₁ : Low Temperature X-ray Diffraction | 14B : High-Precision X-ray Optics |
| (under Construction) | Surface, Interface Structure Analysis |
| 6C ₂ : High Precision X-ray Diffraction | 14C : High-Speed X-ray Topography |
| (under construction) | X-ray Radiography |
| 7A : Soft X-ray Photoemission Spectroscopy | X-ray Diffraction by Gas |
| (Plane Grating Monochromator) | Compton Scattering |
| 7B : Surface Photo-Chemical Reaction | Magnetic Scattering |
| (1 m Seya-Namioka Monochromator) | 15A : Small Angle X-ray Scattering (Muscle) |
| 7C : EXAFS and X-ray Diffraction | 15B : X-ray Topography |
| 8A : Soft X-ray Spectroscopy | X-ray Interferometer |
| (Self-Focusing Plane Grating Monochromator) | 15C : High Resolution X-ray Diffraction |
| 8B : EXAFS (Double Crystal) | 16A ₁ : Multipole Wiggler Mode (under Construction) |
| 8C ₁ : X-ray Lithography | 16A ₂ : Multipole Wiggler Mode (under Construction) |
| 8C ₂ : X-ray Tomography and Radiography | 16C : Undulator (under Construction) |
| 9A : X-ray Lithography | 17A : Solid Surface Analysis (under Construction) |
| 9B : Photo-Chemical Vapor Deposition | 17B : Photo-Chemical Vapor Deposition |
| (under Construction) | (under Construction) |
| 9C : EXAFS and X-ray Diffraction | 17C : Lithography (under Construction) |
| 10A : Crystal Structure Analysis (Minerals) | 21 : X-ray Beam Monitor |

Fig. 2 All PF experiments and the arrangement of magnets along the ring

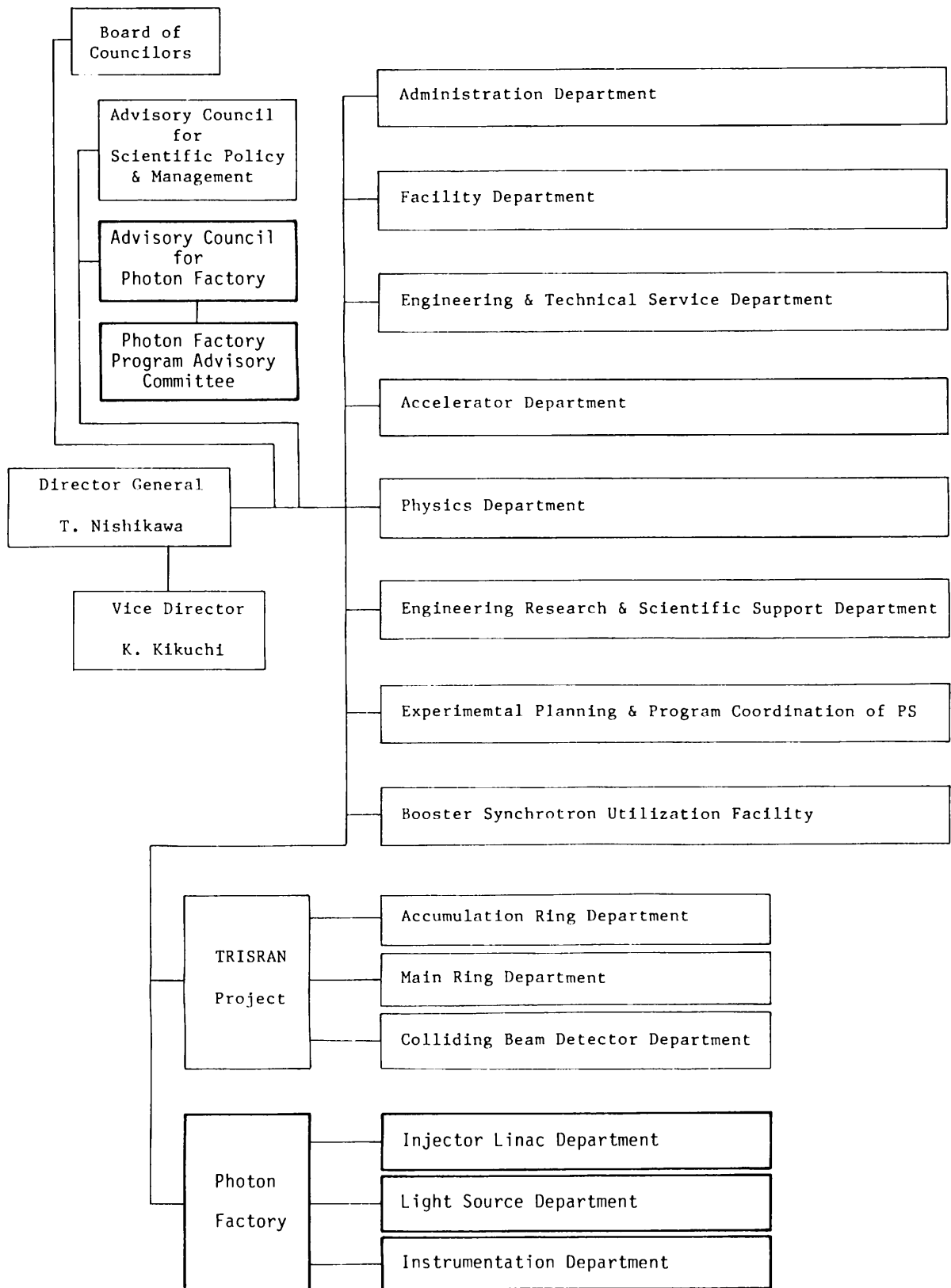


Fig. 3 Organization of KEK

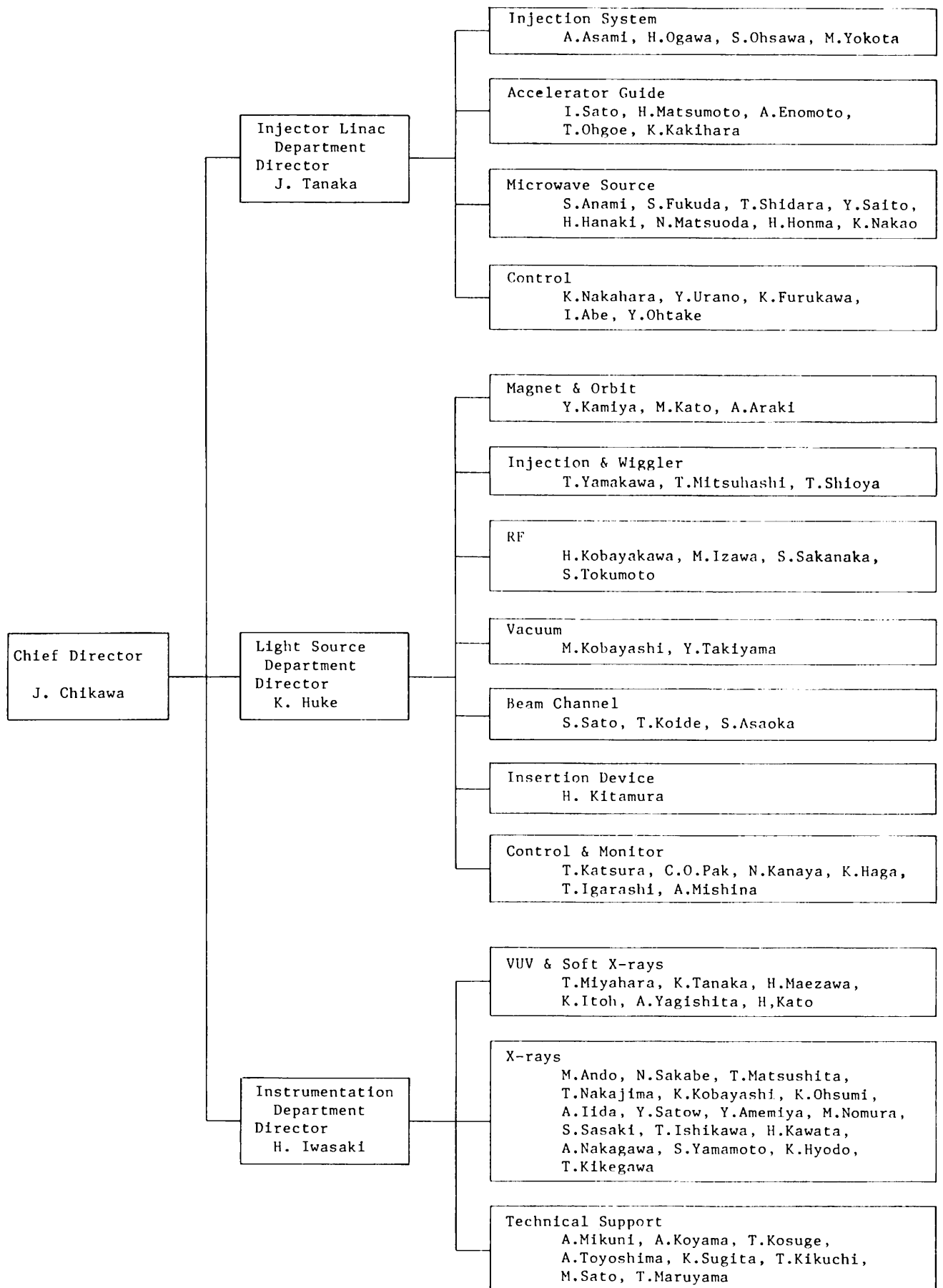


Fig. 4 Organization and Members of Photon Factory

The Advisory Council of the PF was established to discuss scientific programs and management of the PF. This council consists of twenty-one persons of learning and experience; ten members are from outside KEK (Table 3). The term of membership is two years.

The Advisory Council has its own Program Advisory committee (PAC) for examining experi-

mental proposals with respect to their scientific aspects and technical feasibilities. The PAC (Fig.3) includes the directors of the three departments and twelve or less persons of learning and experience from outside KEK (Table 4). The term of the membership is also two years; half of the outside members are changed every year.

Table 2 Annual number of staff & visiting scientists

Position	Division	1978	1979	1980	1981	1982	1983	1984	1985	1986
Chief Director		1	1	1	1	1	1	1	1	1
Professor	Injector Linac	1	2	3	3	3	3	3	3	4
	Light Source	1	4	4	4	4	4	4	3	4
	Instrumentation	0	0	0	1	1	1	1	2	3
Associate Professor	Injector Linac	0	1	1	1	2	2	2	2	1
	Light Source	1	5	4	4	4	3	5	5	3
	Instrumentation	0	0	1	3	4	5	5	8	7
Research Associate	Injector Linac	1	3	4	6	7	8	9	10	11
	Light Source	0	1	4	6	7	7	6	8	9
	Instrumentation	0	0	3	2	7	10	10	10	13
Technical Staff	Injector Linac	0	0	2	4	5	5	6	6	7
	Light Source	3	3	3	4	6	6	6	6	7
	Instrumentation	0	0	0	0	1	2	4	4	8
Visiting Scientist	Injector Linac	2	2	2	2	2	2	2	2	2
	Light Source	2	6	4	4	4	4	4	4	4
	Instrumentation	0	0	6	6	6	6	6	6	6
Total		12	28	42	51	64	69	74	80	90

Table 3 Members of advisory council

* : Chairman
** : Vice-Chairman

Prof. ANDO, Masami	PF Instrumentation Department, KEK.
Prof. ASAMI, Akira	PF Injector Linac Department, KEK.
Prof. HUKE, Kazuo*	Director of PF Light Source Department, KEK.
Prof. IJIMA, Takao	Faculty of Science, Gakushuin University.
Prof. IITAKA, Yoichi	Faculty of Pharmaceutical Sciences, University of Tokyo.
Prof. ISHII, Takehiko	Institute for Solid State Physics, University of Tokyo.
Prof. ITOH, Takashi	College of Arts & Science, University of Tokyo.
Prof. IWASAKI, Hiroshi	Director of PF Instrumentation Department, KEK.
Prof. KOBAYAKAWA, Hisashi	PF Light Source Department, KEK.
Prof. KOMURA, Yukitomo	Faculty of Science, Hiroshima University.
Prof. KURODA, Haruo**	Faculty of Science, University of Tokyo.
Prof. MITSUI, Toshio	Faculty of Engineering Science, Osaka University.
Prof. NAKAHARA, Kazuo	PF Injector Linac Department, KEK.
Prof. SAGAWA, Takashi	Faculty of Science, Tohoku University
Prof. SAKABE, Noriyoshi	PF Instrumentation Department, KEK.
Prof. SATO, Isamu	PF Injector Linac Department, KEK.
Prof. SATO, Shigeru	PF Light Source Department, KEK.
Prof. TANAKA, Jiro	Director of PF Injector Linac Department, KEK.
Prof. TOKONAMI, Masayasu	Faculty of Science, University of Tokyo.
Prof. UNO, Ryosei	College of Humanities & Sciences, Nihon University,
Prof. YAMAKAWA, Tatsuya	PF Light Source Department, KEK.

Table 4 Members of program advisory committee

* : Chairman

Prof. AKISADA, Masayoshi	Institute of Clinical Medicine, University of Tsukuba.
Prof. GOHSHI, Yohichi	Department of Industrial Chemistry, University of Tokyo.
Prof. HARADA, Jimpei	Department of Applied Physics, Nagoya University.
Prof. HUKU, Kazuo	Director of PF Light Source Department, KEK.
Prof. IITAKA, Yoichi	Faculty of Pharmaceutical Sciences, University of Tokyo.
Prof. IKEDA, Shigerou	Faculty of Science, Osaka University.
Prof. IWASAKI, Hiroshi*	Director of PF Instrumentation Department, KEK.
Prof. MARUMO, Fumiyuki	Research Laboratory of Engineering Materials, Tokyo Institute of Technology.
Prof. MINOMURA, Shigeru	Faculty of Science, Hokkaido University.
Prof. MITSUI, Toshio	Faculty of Engineering Science, Osaka University.
Prof. NAMIOKA, Takeshi	Research Institute for Scientific Measurements Tohoku University.
Prof. OHTA, Toshiaki	Faculty of Science, Hiroshima University.
Prof. SUGANO, Satoru	Institute for Solid State Physics, University of Tokyo.
Prof. TANAKA, Jiro	Director of PF Injector Linac Department, KEK.
Prof. YAMADA, Yasusada	Institute for Solid State Physics, University of Tokyo.

Table 5 PF-Budget in each fiscal year

(in million yen)

Items	1978	1979	1980	1981	1982	1983	1984	1985	1986
Salary	10	82	179	269	402	474	484	491	510
Beam Channel Construction & Equipments	534	1,510	2,723	2,874	1,103	0	0	153	131
Site & Buildings	868	2,546	4,561	2,529	0	0	0	0	0
PF Experiments	0	0	0	0	140	153	134	184	190
PF Operation & Maintenance	0	7	60	177	412	477	552	653	820
Computer Rentals	0	0	34	135	136	135	135	135	136
Positron Source Operation & Maintenance	0	0	0	0	0	0	0	41	138
Cooling Systems & Electric Plant Operation	0	0	0	60	120	111	124	180	211
Electricity	0	1	26	52	209	226	257	338	381
PF-Industrial Cooperative Experiments	0	0	0	0	0	94	84	95	185
Miscellaneous	29	55	58	77	115	134	115	127	162
Total	1,441	4,201	7,641	6,173	2,637	1,804	1,885	2,397	2,864

4. BUDGET

The budget of the Photon Factory from its beginning is shown in Table 5. Financial support for the PF is obtained from the government. During FY1986, 33.4 % of the budget will pay for the operation and maintenance of the PF; 20.7 % will pay for electricity.

5. OPERATION TIME AND PROPOSAL

There are three machine operation terms scheduled for 1986 (Table 6). The operation of the first term was 1008 hours and those of second and third term will be 1104 and 1032 hours, respectively. The operation scheduled for each cycle of a term are shown in Table 7. The wiggler is not operated between Saturday morning and Monday morning for users beam time.

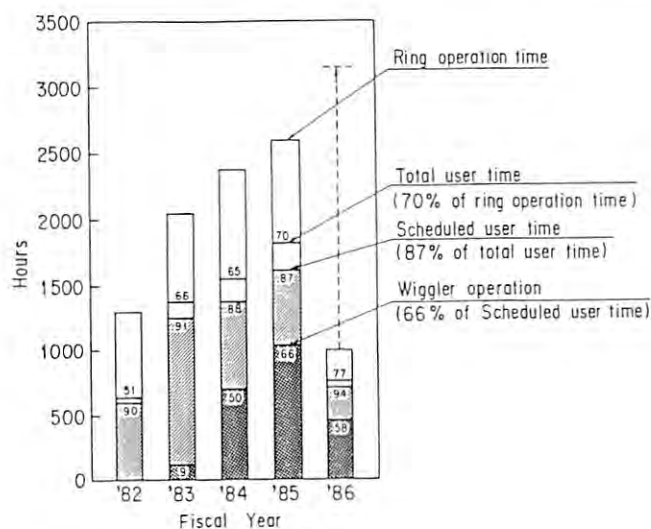


Fig. 5 Ring operation statistics (from the first operation of the PF).

Table 6 Operation schedule in FY 1986

Term	Cycle	Month/Date	Month/Date	Tuning (h)	Machine Study (h)	User Time (h)	Total (h)
1	0	5/7 (Wed)	~ 5/9 (Fri)	48	0	0	48
1	1	5/14 (Wed)	~ 5/24 (Sat)	8	64	168	240
1	2	5/28 (Wed)	~ 6/7 (Sat)	8	64	168	240
1	2.5	6/9 (Mon)	~ 6/14 (Sat)				
1	3	6/18 (Wed)	~ 6/28 (Sat)	8	64	168	240
1	4	7/2 (Wed)	~ 7/12 (Sat)	8	64	168	240
2	0	10/7 (Tues)	~ 9/10 (Thur)	48	0	0	48
2	1H	10/14 (Tues)	~ 10/18 (Sat)	8	24	64	96
2	2	10/22 (Wed)	~ 11/1 (Sat)	8	64	168	240
2	2.5	11/4 (Tues)	~ 1/8 (Sat)				
2	3	11/12 (Wed)	~ 11/22 (Sat)	8	64	168	240
2	4	11/26 (Wed)	~ 12/6 (Sat)	8	64	168	240
2	5	12/10 (Wed)	~ 12/20 (Sat)	8	64	168	240
3	0	1/13 (Tues)	~ 1/16 (Fri)	48	0	0	48
3	1	1/21 (Wed)	~ 1/31 (Sat)	8	64	168	240
3	2	2/2 (Mon)	~ 2/14 (Sat)	0	72	216	288
3	3H	2/16 (Mon)	~ 2/21 (Sat)	8	24	88	120
3	3.5	2/23 (Mon)	~ 2/28 (Sat)				
3	4	3/4 (Wed)	~ 3/14 (Sat)	8	64	168	240
3	5H	3/16 (Mon)	~ 3/20 (Fri)	8	24	64	96
Total				248	784	2112	3144

Injector Linac additionally kept operating both between 1/31 (Sat) and 2/2 (Mon), and between 2/14 (Sat) and 2/16 (Mon) for TRISTAN Main Ring operation.

Table 7 Operation schedule in each cycle

Schedule of 96 hours run

Schedule of 120 hours run

	Sun	Mon	Tues	Wed	Thur	Fri	Sat
A	*	*	*	U	U	U	M
B	*	*	T	U	U	M	*
C	*	*	U	U	U	M	*

	Sun	Mon	Tues	Wed	Thur	Fri	Sat
A	*	*	U	U	U	U	M
B	*	T	U	U	U	M	*
C	*	U	U	U	U	M	*

Schedule of 240 hours run

	Sun	Mon	Tues	Wed	Thur	Fri	Sat	Sun	Mon	Tues	Wed	Thur	Fri	Sat
A	*	*	*	*	M	U	U	U	U	M	U	U	U	M
B	*	*	*	T	U	U	U	U	M	U	U	U	M	*
C	*	*	*	M	U	U	U	U	M	U	U	U	M	*

Schedule of 288 hours run

	Sun	Mon	Tues	Wed	Thur	Fri	Sat	Sun	Mon	Tues	Wed	Thur	Fri	Sat
A	*	*	M	U	U	U	U	U	U	M	M	U	U	U
B	*	M	U	U	U	U	U	U	M	M	U	U	U	*
C	*	M	U	U	U	U	U	U	M	M	U	U	U	*

A : 1:00 a.m. - 9:00 a.m.
 B : 9:00 a.m. - 5:00 p.m.
 C : 5:00 p.m. - 1:00 a.m.

M : Machine study
 U : Users beam time
 T : Tuning

Fig. 5 shows the annual ring operation time of the PF. This figure suggests that the ring operation time has increased remarkably; also, the percentage of user time in the ring operation time has become larger. This means that the efficiency of the ring usage has been improving.

About 25 % of the operation time is used for machine studies. Such studies are effective for the improvement of stability, long life, low emittance configuration, positron operation and so on.

There are three routes for use of the PF beam lines. Scientists from universities and research institutes belonging to the government or a public organization can use the beam lines without charge if their proposals are accepted by PAC. The deadlines for the applications are January 14th and July 14th every year. We call such accepted scientists "general users" and each subject is effective through two years.

The number of proposals submitted by general users from the beginning of the PF is listed in Table 8.

The second type is for scientists of private enterprises; these users are charged. Category A is for cooperative experiments with PF staff; this type must be authorized by the Japanese government if the government supports less than a half of experimental expenses (depending upon the objectives). The deadline for an application is usually January. Category B is for private experiments of the above scientists; proposals can be accepted at any time by the Advisory Council for the PF. The number of the proposals belonging to the above two categories is also listed in Table 9.

Last of all, category C is for cooperative experiments with PF staff; all experimental expenses must be paid by the private enterprise.

Table 8 Number of proposals by general users since the beginning of the PF

Research Field	Period*	1983-I	1983-II	1984-I	1984-II	1985-I	1985-II	1986-I	1986-II	Total
EXAFS		25	17	16	10	22	13	21	19	143
X-Ray (Biology)		10	8	11	7	22	6	18	10	92
X-Ray (Material Sciences)		19	5	8	21	62	13	29	25	182
Soft X-Ray & VUV		13	6	2	10	12	15	7	19	84
Total		67	36	37	48	118	47	75	73	501

* I and II indicate periods when proposals were accepted by the Program Advisory Council (PAC) in March and in September, respectively.

Table 9 Beam time used by industries since the beginning of PF

		1983	1984	1985	1986
General Industries	No. of Industries	11	12	11	7
	No. of Proposals	20	35	21	10
	Beam Time Used (h)	467	905	814	326
	Ratio* (h)	42	75	74	46
Industries Which Have Their Own Beam Lines	No. of Industries	1	1	3	4
	No. of Proposals	1	1	3	4
	Beam Time Used (h)	219	217	424	1211
	Ratio* (h)	291	217	141	302
Total	No. of Industries	12	13	14	11
	No. of Proposals	21	36	24	14
	Beam Time Used (h)	686	1122	1238	1537
	Ratio* (h)	57	86	88	139

Ratio* Beam Time Used / No. of Industries

6. LIST OF PROPOSALS

6.1 Proposals accepted by Program Advisory Committee

<u>Proposal Number</u>	<u>Spokesperson</u>	<u>Title</u>
86-001	M. Ichikawa Research Institute for Catalysis, Hokkaido Univ.	EXAFS Characterization of Bimetal Clusters Entrapped in Inorganic Microcavities
86-002	N. Kamijo Government Industrial Research Institute, Osaka ²	An XANES and EXAFS Study of Gold Catalysts
86-003	T. Imura Faculty of Engineering, Hiroshima Univ.	Study on Metastable Microcrystallite Including Ge, Sn and Te
86-004	T. Onishi Research Laboratory of Resources Utilization, Tokyo Institute of Technology	EXAFS Study on the Structure of Catalysts for Photodecomposition of Water
86-005	H. Terauchi Dept. of Physics, Kwansei-Gakuin Univ.	EXAFS Studies on Premartensitic Phases in A-15 Compounds
86-006	T. Iwamoto Dept. of Pure & Applied Sciences, Univ. of Tokyo	Study on Formation Mechanism and Structure of Metal Complex Host Inclusion Compounds
86-007	A. Yoshiasa Institute of Scientific & Industrial Research, Osaka Univ.	Structure Chemistry of Silver Iodide Polymorphs by EXAFS
86-008	H. Wakita Faculty of Science, Fukuoka Univ.	A Structural Study of Bis (vic-alkanedione dioximato) Nickel(II) in Solid, Molten and Solution
86-009	I. Nakai Dept. of Chemistry, Univ. of Tsukuba	EXAFS Analysis of High Pressure Phases of Arsenic Sulfides
86-010	H. Kuroda Faculty of Science, Univ. of Tokyo	EXAFS Study on Monometallic and Bimetallic Clusters Supported on Molecular-Sieving Carbon
86-011	H. Kuroda Faculty of Science, Univ. of Tokyo	Structure of Ultrafine Iron Oxides on Activated Carbon Fibers
86-012	Y. Iwasawa Faculty of Science, Univ. of Tokyo	EXAFS Studies on the Structure of the Attached ZrO ₂ and ZnO Super Thin-Layer Oxide Catalysts
86-013	Y. Iwasawa Faculty of Science, Univ. of Toyko	EXAFS Studies on the Structural Transition of the V ₂ O ₅ -PO ₄ Catalysts under the Reaction Conditions
86-014	Y. Iwasawa Faculty of Science, Univ. of Tokyo	SEXAFS Studies on the Structure of Ru ₃ (CO) ₁₂ Deposited on the Oxide Single Crystals ³
86-015	M. Sano College of General Education, Nagoya Univ.	XANES Spectra of Various Cobalt Complexes and Their Rules

-
- 1) Ministry of Agriculture, Forestry & Fisheries
 2) Ministry of International Trade & Industry
 3) Science & Technology Agency

86-016	Y. Hiragi Institute for Chemical Research, Kyoto Univ.	EXAFS Studies of Selenocystin and Selenocystein
86-017	M. Niwa Faculty of Engineering, Nagoya Univ.	An EXAFS Study on the Structure of the Germanium Oxide on Zeolites Prepared by CVD Method
86-018	K. Shibata Faculty of Engineering, Univ. of Tokyo	Solid Solution Hardening by Carbon and Nitrogen of Austenitic Steels
86-019	T. Yamane Faculty of Engineering, Nagoya Univ.	Crystal Structure Analyses of Bowman-Birk Type Protease Inhibitor
86-020	T. Masujima Research Institute for Nuclear Medicine & Biology, Hiroshima Univ.	Photoacoustic X-Ray Absorption Spectroscopy (PAXAS)-Detection System and Application to Dosimetry-
86-021	T. Yamane Faculty of Engineering, Nagoya Univ.	Crystal Structure Analyses of Peanut Protease Inhibitors
86-022	Y. Yamane Faculty of Engineering, Nagoya Univ.	Crystal Structure Analysis of st. Frythreus Trypsin
86-023	K. Shinohara Tokyo Metropolitan Institute of Medical Science	Observation of Biological Specimen by X-Ray Microscopy
86-024	K. Fukuyama Faculty of Engineering, Tottori Univ.	X-Ray Diffraction Study on Spherical Viruses
86-025	K. Kajiwara Institute for Chemical Research, Kyoto Univ.	Association Mechanism of β -Casein
86-026	Y. Hiragi Institute for Chemical Research, Kyoto Univ.	Polymerization Process of TMV Protein Studied by Time-Resolved Small-Angle Scattering
86-027	Y. Inoko Faculty of Engineering Science, Osaka Univ.	Small-Angle X-Ray Scattering Study on Higher-Order Structures of Chromatin in Solution
86-028	M. Kataoka Faculty of Science, Tohoku Univ.	X-Ray Solution Scattering Studies on Solubilized Bacteriorhodopsin
86-029	M. Nagura Faculty of Textile Science & Technology, Shinsyu Univ.	Molecular Conformation of Silk Fibroin
86-030	N. Tanaka Institute for Protein Research, Osaka Univ.	Structural Studies on Aldolase in Solution
86-031	T. Tsukihara Faculty of Engineering, Tottori Univ.	Structure Determination of Active Centers of a Ferredoxin from <i>M. Smegmatis</i>
86-032	Y. Matsuura Institute for Protein Research, Osaka Univ.	Utilization of Anomalous Scattering in the Structure Analysis of Cytochromes C from <i>D. Vulgaris</i>
86-033	T. Ito Institute of Physical and Chemical Research ³	Crystal Structure Analysis of ATP Using Small Crystals

86-034	Y. Hata Institute for Protein Research, Osaka Univ.	Structural studies on Serratia Protease in Crystalline State
86-035	T. Mitsui Faculty of Engineering Science, Osaka Univ.	X-Ray Diffraction Studies of the Photointermediates of Triton X-100 Treated Purple Membrane
86-036	T. Mitsui Faculty of Engineering Science, Osaka Univ.	Diffraction Studies of Muscle Contraction by Sinusoidal Length Change
86-037	M. Akiyama Sapporo Medical College	Observation of Phase Transition Process by X-Ray Diffraction Method in Multilamellar Phospholipids
86-038	Y. Tajima Faculty of Science, Tokyo Metropolitan Univ.	X-Ray Structure Analysis of Thin Filaments of a Tonically Contracted Muscle
86-039	M. Ishikawa National Institute of Radiological Sciences ³	Quantitative Determination of Ultra-Trace Elements in Sea Water by SR Excited X-Ray Fluorescence Analysis
86-040	S. Endo Faculty of Engineering Science, Osaka Univ.	X-Ray Diffraction under Ultrahigh Pressure and High Temperature with Sintered Diamond Anvils
86-041	A. Iida Photon Factory, National Laboratory for High Energy Physics	Near Surface Analysis by Total Reflection X-Ray Fluorescence
86-042	N. Yasuoka Basic Research Laboratory, Himeji Institute of Technology	X-Ray Diffraction Studies of Hydrogenase and High-Molecular-Weight Cytochrome in Sulfate Reducing Bacteria
86-043	H. Kawamura National Research Institute for Metals ³	Pressure Induced Phase Transition of Semiconductor under Low Temperature-Pressurizing
86-044	J. Susaki Institute for Solid State Physics, Univ. of Tokyo	Structural Analysis of CaSiO_3 Perovskite under High-Pressure
86-045	H. Iwasaki Photon Factory, National Laboratory for High Energy Physics	Structure Determination by Frequency-Modulated X-Ray Diffraction
86-046	H. Iwasaki Photon Factory, National Laboratory for High Energy Physics	Phase Transition of Amorphous Rare-Earth-Based Alloys under High Pressure and Temperature
86-047	M.H. Manghnani Hawaii Institute of Geophysics, Univ. of Hawaii	Precise Measurements of Equation of State for $(\text{Mg}, \text{Fe})_2\text{SiO}_4$ Spinel and Rocksalt-Type $(\text{Mg}, \text{Fe})\text{O}$
86-048	S. Hashimoto Research Institute for Iron Steel & Other Metals, Tohoku Univ.	Study on the Local Atomic Arrangements in the Disordered Ternary Alloy through a Separating Method for the SRO Partial Intensities
86-049	Y. Kashihara Faculty of Engineering, Nagoya Univ.	Study of Atomic Displacement in Epitaxial Film Interface Region by X-Ray Grazing Angle Diffraction
86-050	Y. Shiozaki Faculty of Science, Hokkaido Univ.	Higher Harmonic Component of Modulation Wave in Incommensurate Thiourea

86-051	J. Harada Dept. of Applied Physics, Nagoya Univ.	X-Ray Diffuse Scattering Study of Structural Fluctuations in Mixed Crystals
86-052	J. Harada Dept. Applied Physics, Nagoya Univ.	X-Ray Characterization of Microstructure of Ion-Planted Si Crystals
86-053	Y. Kitano Faculty of Science, Hiroshima Univ.	Short Range Order in hcp Solid Solutions
86-055	A. Matsumuro Faculty of Engineering, Nagoya Univ.	Measurements of Pressure Dependence of Debye Temperature on Aluminum
86-056	H. Terauchi Dept. of Physics, Kwansei-Gakuin Univ.	Diffuse X-Ray Scattering by Synchrotron Radiation
86-057	M. Sakata Dept. of Applied Physics, Nagoya Univ.	Characterization of GaAs and $(\text{Ga}_m\text{Al}_n)\text{As}$ Super Lattice on Chemical Composition
86-058	K. Gouhara Dept. of Applied Physics, Nagoya Univ.	Photon Counting in X-Ray Diffraction
86-059	T. Murata Dept. of Physics, Kyoto Univ. of Education	FREXAFS Study of Lattice Relaxation of Impurities in Ionic Crystals
86-060	K. Kajiwara Institute for Chemical Research, Kyoto Univ.	Lyotropic Mesophase of Imogolite
86-061	T. Ito Institute of Physical and Chemical Research ³	Study of the Electron Density Distribution in Metal Borides
86-062	F. Marumo Research Laboratory of Engineering Materials, Tokyo Institute of Technology	Study of Thermal Vibration and Electron Distribution in Transition Metal Compounds by Short Wave Length Synchrotron Orbital Radiation
86-063	Y. Waseda Research Institute of Mineral Dressing & Metallurgy Tohoku Univ.	Determination of the Environments Structure Around a Specific Atom in Disordered Materials by the Anomalous X-Ray Scattering
86-064	M. Toriumi Faculty of Science, Univ. of Tokyo	Direct Observation of Deforming Polycrystals at High T
86-065	K. Osamura Dept. of Metallurgy, Kyoto Univ.	Dynamical Structure Change during Initial Stage of Phase Decomposition and during Reversion Process in Al-Zn Alloys
86-066	T. Takahashi Faculty of Engineering, Chiba Institute of Technology	Dynamical Structures during Phase Decomposition of Initial Stage in Al-Cu Alloys
86-067	S. Todo Institute for Solid State Physics, Univ. of Tokyo	X-Ray Study on Low Temperature Phase of Magnetite at 15 K
86-068	T. Suzuki Dept. of Physics, Sophia Univ.	Soft-X-Ray pA Scattering by Light Element Solids

86-069	T. Sagawa Faculty of Science, Tohoku Univ.	XPS Study of Mixing between 4f Orbital and Valence Band in Heavy Rare Earth Elements
86-070	T. Tomiki Faculty of Science, Univ. of Ryukyus.	VUV Spectra of Single Crystals of Al_2O_3 and Y_2O_3
86-071	A. Misu Faculty of Science, Science Univ. of Tokyo	Piezorefectivity Spectra of Alkali Halide and $Gd_{3-x}Bi_xIG$
86-072	M. Kawabe Institute of Materials Science, Univ. of Tsukuba	Photodissociation Process of Semiconductor Etching Gas (HCl , Cl_2 , NF_3)
86-073	T. Hayashi Institute of Applied Physics, Univ. of Tsukuba	Multiple Photoionization Processes in Rydberg States
86-074	K. Tanaka Photon Factory, National Laboratory for High Energy Physics	The Study of Fundamental Processes of Photochemical Vapor Deposition and Photochemical Etching by Using Synchrotron Radiation
86-075	M. Kamachi Faculty of science, Osaka Univ.	EXAFS Study on the Local Structure in Magnetic Materials of Polymers
86-076	H. Hashizume Research Laboratory of Engineering Materials, Tokyo Institute of Technology	Dynamical X-Ray Diffraction Phenomena at Grazing Incidence and Their Applications
86-077	H. Hashizume Research Laboratory of Engineering Materials, Tokyo Institute of Technology	Characterization of Synthetic Multilayers for Synchrotron Radiation Optics by Diffraction Methods
86-078	T. Yokokawa Faculty of Science, Hokkaido Univ.	EXAFS and XANES Studies on the Phase-Separated Glasses Containing Transition Metal Ions
86-079	H. Kuroda Faculty of Science, Univ. of Tokyo	Study on the Electronic Structures of Highly Conductive (Phthalo Cyaninato) Nickel Complexes by Polarized XANES Spectrum
86-080	H. Kuroda Faculty of Science, Univ. of Tokyo	XANES and EXAFS Study in the Ru Clusters on Cu or Au Substrate
86-082	K. Shibata Faculty of Engineering, Univ. of Tokyo	Study on Solid Solution Hardening of Austenitic Steels by EXAFS
86-083	F. Marumo Research Laboratory of Engineering Materials, Tokyo Institute of Technology	Site Preference of Transition Metal Ions in Garnet with Various Occurrences
86-084	H. Morikawa Research Laboratory of Engineering Materials, Tokyo Institute of Technology	A Structural Study of $AgBr-Ag_2O-GeO_2$ Glasses by EXAFS Analysis
86-085	S. Yoshida Faculty of Engineering, Kyoto Univ.	Analysis of Structure of Bimetallic Catalysts Prepared by the Solvated Metal Atom Dispersion Method
86-086	S. Yoshida Faculty of Engineering, Kyoto Univ.	On the Correlation between Catalysis and Local Structures of Composite Iron Oxide Gas Sensors

86-087	Y. Nakamura Faculty of Engineering, Kyoto Univ.	EXAFS Observation of Vapor Quenched Fe-Ag and Fe-Ti Alloys
86-088	Y. Noda Faculty of Engineering Science, Osaka Univ.	EXFAS Studies of Local Ordering in ω -Phase Alloy
86-089	K. Koto Institute of Scientific & Industrial Research, Osaka Univ.	Crystallization of the Stabilized Zirconias
86-090	A. Yoshiasa Institute of Scientific & Industrial Research, Osaka Univ.	EXAFS Study of the $\text{Sr}(\text{Co}_{1-x}\text{Mn}_x)\text{O}_3$ Perovskite Type Solid-Solution
86-091	T. Sakurai College of General Education, Osaka Univ.	The Active Site in Ascorbate Oxidase
86-092	C. Miyake Faculty of Engineering, Osaka Univ.	An EXAFS Study of "the Third Phase" in Nuclear Fuel Reprocessing
86-093	T. Morimoto Faculty of Science, Okayama Univ.	Local Crystal Structure of Exchanged Ions in Zeolite
86-094	M. Kurahashi National Chemical Laboratory for Industry, Agency of Industrial Science & Technology ²	EXAFS and XANES of Metallic Components in Plant Leaves
86-095	M. Nomura Photon Factory, National Laboratory for High Energy Physics	Structure of Active Sites on Supported Bimetal Cluster Catalysts
86-096	O. Shimomura National Institute for Research in Inorganic Materials ³	XANES Study of Pressure Induced Semiconductor-Metal Transition
86-097	C.D. Garner Manchester Univ.	EXAFS and XANES Studies on Nitrogenase
86-098	K. Hieda Faculty of Science, Rikkyo Univ.	Radiobiological Effects of Phosphate K-Shell Ionization on DNA Molecules
86-099	K. Hieda Faculty of Science, Rikkyo Univ.	Radiobiological Effects of Monochromatic X-Rays on Bromouracil Substituted DNA
86-100	K. Takakura International Christian Univ.	NMR Study of Molecular Damage in Nucleic Acid Induced by SR-Soft X-Ray Irradiation
86-101	H. Maezawa Dept. of Radiology, Tokai Univ.	Killing and Mutation of Bacterial Cells and Bacteriophages by Innershell Ionization of Phosphorus after Monochromatic Soft X-Rays Irradiation.
86-102	K. Kobayashi Photon Factory, National Laboratory for High Energy Physics	Induction of Genetic Changes in Yeast Cells Irradiated with Monochromatic Soft (1 keV - 5 keV) X-Rays
86-103	Y. Hiragi Institute for Chemical Research, Kyoto Univ.	Change of the Quarternary Structure on Tryptophanase

86-104	M. Kimura Niigata College of Pharmacy	Biological Activities of Myelin Proteins
86-105	Y. Muroga Faculty of Engineering, Nagoya Univ.	Kinetics of the Helix-Coil Transition in Solutions of Polyglutamic Acid
86-106	S. Tokutomi National Institute for Basic Biology	X-Ray Solution Scattering Studies on Phytochrome Phototransformation
86-107	H. Inoue National Institute of Agrobiological Resources ¹	Association-Dissociation Process of Cucumber Green Mottle Mosaic Virus Coat Protein Determined by Time-Resolved X-Ray Solution Scattering
86-109	H. Ihara Electrotechnical Laboratory ²	X-Ray Diffraction on the High-Pressure Synthesis of Bi-MoN
86-110	T. Nasu Faculty of Education, Yamagata Univ.	X-Ray Diffraction Analysis on Local Structure Changes of Amorphous Alloys
86-111	N. Mori Institute for Solid State Physics, Univ. of Toyko	High Pressure X-Ray Studies on the Magnetic- Nonmagnetic Transition of Iron Alloys
86-112	K. Tsuji Faculty of Science & Technology, Keio Univ.	Low Temperature and High Pressure X-Ray Study on the Pressure-Induces Phase Transition of Amorphous Semiconductors
86-113	E. Kita Institute of Physics, Univ. of Tsukuba	Structural Analysis of Iron-Rare-Earth Multi-Layered Films
86-114	I. Shirovani Muroran Institute of Technology	Structure and Phase Transition of Black Phosphorus and Black Phosphorus Arsenic Alloy at Very Low Temperatures and High Pressures
86-115	A. Yamamoto National Institute for Research in Inorganic Materials ³	Determination of the Symmetry and Crystal Structure of Al-Mn Quasicrystals by Means of S.R. X-Rays
86-116	Y. Yoshioka Musashi Institute of Technology	X-Ray Stress Measurement by Use of Synchrotron Radiation Source
86-117	K. Ishida Faculty of Science & Technology, Science, Univ. of Tokyo	X-Ray Diffraction Study on X-Ray Magnetic Scattering by Hexagonal Ferrite
86-118	Y. Fujii Faculty of Engineering Science, Osaka Univ.	Test of Optical Elements for X-Ray Inelastic Scattering Project
86-119	T. Yagi Institute for Solid State Physics, Univ. of Toyko	Precise Determination of the Equations of State of Mantle Minerals
86-120	T. Yagi Institute for Solid State Physics, Univ. of Tokyo	Pressure Measurements Based on a Gold Pressure Scale in Mega-bar Region
86-121	O. Shimomura National Institute of Research in Inorganic Materials ³	Generation of Ultrahigh Pressure by Double Stage Multi-Anvil High Pressure System
86-122	N. Hamaya Faculty of Engineering Science, Osaka Univ.	Search for the Devil's Staircase of Modulated Structures in Rare Earth Elements under High Pressure

86-123	T. Kikegawa Photon Factory, National Laboratory for High Energy Physics	Measurements of Temperature Factor of High Pressure Phases of Elements
86-124	F. Ito Research Institute for Iron Steel & Other Metals, Tohoku Univ.	Precise Determination of Fermi Surface in Metals and Alloys by Means of High Resolution Compton Scattering
86-125	S. Konaka Faculty of Science, Hokkaido Univ.	Electron Distribution in the Water Molecule as Studied by Angle-Dispersive X-Ray Diffraction
86-126	F. Sato Science & Technical Research Laboratories, Japan Broadcasting Corporation	In-Situ X-Ray Study of Dislocation Dynamics in Compound Semiconductors at High Temperatures
86-127	S. Nanao Institute of Industrial Science, Univ. of Tokyo	Structural Study of Al-Ru-Mn Icosahedral Alloy by Anomalous X-Ray Scattering
86-128	H. Kawata Photon Factory, National Laboratory for High Energy Physics	X-Ray Magnetic Scattering Topography
86-129	O. Nittono Faculty of Engineering, Toyko Institute of Technology	Synchrotron Topographic Study of MBE Film/InP Wafers Subject to Various Heat-Treatments
86-130	S. Nanao Institute of Industrial Science, Univ. of Tokyo	Structural Study of GaAs/AlAs Superlattices
86-131	H. Suzuki Research Institute for Iron Steel & Metals, Tohoku Univ.	Direct Observation of Lattice Defects in Solid Helium by X-Ray Topography
86-132	M. Hidaka Faculty of Science, Kyushu Univ.	Correlation between Long-Range and Short-Range Order of Structural Phase Transition
86-133	S. Nakai Faculty of Engineering, Utsunomiya Univ.	Measurement of the Angular Distribution in Al and Si K-XPS Plasmon Satellites
86-134	H. Tawara Institute of Plasma Physics, Nagoya Univ.	Innershell Photoionization Processes in X-Ray Energy Range
86-135	J. Murakami Research Institute for Scientific Measurement, Tohoku Univ.	Auger-Electron and Fragment-Ion Spectroscopy of N ₂ , O ₂ and N ₂ O
86-136	T. Sasaki Faculty of Engineering Science, Osaka Univ.	Photoionization Processes of Phosphates from K-Shell of Phosphor
86-137	T. Sakaki Faculty of Engineering Science, Osaka Univ.	Photodissociative Processes of Monosilane (SiH ₄) Associated with SiK Hole States
86-138	A. Iida Photon Factory, National Laboratory for High Energy Physics	Trace Element Determination Using Undulator Radiation
86-139	T. Ohta Faculty of Science Hiroshima Univ	Study on Surface Structure of High M.P. Metal Silicides with the Soft X-Ray Standing Wave Method

86-140	T. Ohta Faculty of Science, Hiroshima Univ.	Surface EXAFS-XANES Studies of Cu Single Crystal-K Adsorption Systems
86-141	A. Nishijima National Chemical Laboratory for Industry, Agency of Industrial Science & Technology ²	Study on the Local Structure Around Sulfur and Catalytic Activity of Iron Sulfide Catalyst
86-142	I. Toyoshima Research Institute for Catalysis, Hokkaido Univ.	Structure of Adsorbed S on Fe, Co Single Crystal Surfaces by SEXAFS
86-143	I. Ikemoto Faculty of Science, Tokyo Metropolitan Univ.	Sulfur K Absorption Spectra of Organic Conductors (TTF Salts, Ni(mnt) ₂ Salts)
86-144	T. Koide Photon Factory, National Laboratory for High Energy Physics	Optical Reflection Study of the Electronic States of Transition Metal Carbide
86-145	H. Kato Photon Factory, National Laboratory for High Energy Physics	Angle Resolved Photoelectron Spectroscopy of NO on W Surfaces
86-146	A. Fujimori National Institute for Research in Inorganic Materials ³	Resonant Photoemission Study of Rare-Earth Halides
86-147	T. Miyahara Photon Factory, National Laboratory for High Energy Physics	Photoemission Study on the Electronic States of Cu-Ni, Ag-Pd and Other Alloys
86-148	T. Hanyu Faculty of Science, Tokyo Metropolitan Univ.	Resonant Photoemission Spectra of Ce-Alloys
86-149	H. Fukutani Institute of Physics, Univ. of Tsukuba	Photoelectron Spectroscopy of Neutron-Irradiated Graphites
86-150	Y. Sakisaka Faculty of Science, Kyoto Univ.	Angle-Resolved Photoemission Spectroscopy of H- and Xe- covered Cr(110) and Fe(110) Surfaces
86-151	E. Miyazaki Faculty of Science, Tokyo Institute of Technology	Interactions of Gas Molecules with NbC Single Crystal Surfaces
86-152	Y. Sugita Faculty of Science, Toyama Univ.	Section Topography with Higher Order Reflection and Its Application

6.2 Proposals accepted for charged Beam time assignment

<u>Proposal Number</u>	<u>Spokesperson</u>	<u>Title</u>
86-Y001	D. Shinoda Fundamental Research Laboratories, NEC Corporation	X-Ray Optics, X-Ray Lithography Experiments
86-Y002	T. Kitayama Atsugi Electrical Communication Laboratory, NTT	X-Ray Lithography
86-Y003	K. Yoshida Research Center Mitsubishi Chemical Industries Ltd.	The EXAFS Study of Catalysts
86-Y004	K. Kohra Photon Factory Kondankai	Training Course
86-Y005	M. Ogirima Central Research Laboratory, Hitachi Ltd.	Synchrotron Radiation Test for Focusing Mirror System, Double Crystal Monochromator, Exposure System and CT System.
86-Y006	H. Sato NTT Electrical Communications Laboratories	Solid Surface Characterization
86-Y007	H. Sato NTT Electrical Communications Laboratories	Evaluation of Semiconductor Crystals by X-Ray Topography
86-Y008	H. Sato NTT Electrical Communications Laboratories	EXAFS Studies of Superconducting Materials
86-Y009	K. Sasaki Nippon Steel Corporation	AES and XPS Using SOR
86-Y010	N. Yamamoto Central Research Laboratory, Idemitsu Kosan Co., Ltd.	EXAFS Study of Nickel Alloy Catalysts
86-Y011	K. Sasaki Nippon Steel Corporation	Characterization of Amorphous Alloy Products
86-Y012	S. Hoshino Crystallographic Society of Japan	A Short Course in Materials Structure Analysis and Characterization by S.R.
86-Y013	D. Shinoda Fundamental Research Laboratories NEC, Corporation	X-Ray Optics and X-Ray Lithography Experiments
86-Y014	M. Ogirima Central Research Laboratory, Hitachi Ltd.	Synchrotron Radiation Test for Grating and Crystal Monochromator, Exposure System and CT System
86-Y015	T. Miyashita Ibaragi Electrical Communication Laboratory, NTT	In-Situ Observation of Dislocation Motion by White Beam Topography
86-Y016	Y. Yoshida Research Center, Mitsubishi Chemical Industries Ltd.	The EXAFS Study Of Catalysts

PF SEMINARS, MEETINGS AND PUBLICATIONS

PF Seminars

GUDAT, W.S. (Kolm Univ.) March 4, 1985
Bulk and Surface Electronic Properties of Ferromagnets at Finite Temperatures:
Spin Polarized Photoemission Studies

BARBEE, T. W., Jr. (Stanford Univ.) March 22, 1985
Layered Synthetic Microstructures: Reflecting Media for X-ray Optics and Dif-
fracting Structure for the Study of Condensed Matter

VACHETTE, P. (LURE) March 25, 1985
Recent Development at LURE-DCI:SAXS, Dispersive EXAFS, Protein Crystallography

IIDA, A. (Univ. of Tokyo) April 22, 1985
Trace Element Analysis by Synchrotron Radiation

KITAMURA, H. (PF) April 24, 1985
Study on the Technical Feasibility of Multi-pole Wiggler

SAKISAKA, Y. (Kyoto Univ.) April 25, 1985
Angle-resolved Photoelectron Spectroscopy on Clean and Adsorbed Surfaces of
Transition Metals Using Synchrotron Radiation

FUJIMORI, A. (NIRIM) May 20, 1985
Photoemission Spectroscopy on Interfaces between Semiconductors and Rare Earth
Metals

KOTANI, A. (Osaka Univ.) May 21, 1985
Many Body Effects in X-ray Absorption Spectroscopy

KOBAYASHI, K. (Univ. of Tsukuba) July 16, 1985
Radiation Biology Using Synchrotron Radiation

OHSUMI, K. (Univ. of Tokyo) July 17, 1985
Accurate Determination of Crystal Structure by Making Use of Synchrotron
Radiation

KOTANI, A. (Osaka Univ.) July 24, 1985
Spin Polarization of Auger Electrons in Transition Metals

HODGKIN, D. (Univ. of York) October 16, 1985
Actual Crystal Structure of 2Zn Insulin

YOSHINO, K. (Harvard-Smithsonian center for Astrophysics) November 12, 1985
Aeronomy and High Resolution Spectroscopy

MACDOWELL, A. (Daresbury) November 26, 1985
0.1-10 keV Beamline for Surface EXAFS at Daresbury - Design, Performance and
Problems -

HEUBERGER, A. (Fraunhofer-Institute) December 18, 1985
High Resolution Lithography Using Synchrotron Radiation

SHAM, T.K. (BNL & Chinese Univ. of Hong Kong) December 21, 1985
Some Recent Application of X-ray Absorption Spectroscopies with Synchrotron
Radiation

NAKAHARA, K. & URANO, T. (PF) January 8, 1986
Reports on the 2nd International Accelerator Control System Workshop at Los
Alamos and on the SLC Control System

OHSAWA, T. (PF) January 14, 1986
Present Situation of Wake Field Acceleration in DESY and Injector Linacs in
CERN and ORSAY etc.

LABLANQUIE, P. (LURE) Present Status of ACO and Super-ACO	January 16, 1986
PETROFF, J.F. (Univ. Paris VI) (Ga _{1-x} Al _x As) _n /.../GaAs(001) Superlattices: Growth Imperfections Characterized by Synchrotron Radiation Diffraction Techniques	February 3, 1986
HODSON, K.O. (Stanford Univ. & SSRL) X-ray Absorption Edge Studies in the 2-3KeV Energy Range: Experimental and Applications to Molybdenum and Sulfur	March 25, 1986
KURIYAMA, M. (NBS) Description of NBS Materials Science Beam Line at NSLS	April 24, 1986
KAINDL, G. (Frier U. Berlin) M-edge X-ray Absorption Spectroscopy in Rare-earth Materials	June 6, 1986
POUGET, J.P. (Univ. Paris-Sud) X-ray Synchrotron Radiation Study of the Anion Ordering Phase Transition in the Organic Superconductor (TMTSF) ₂ ClO ₄	July 17, 1986
BETZ, H. (Fraunhofer-Institute) X-ray Lithography and the Compact Synchrotron, COSY	August 25, 1986
KNOTEK, M.L. (NSLS) Management and Science of National Synchrotron Light Source	September 16, 1986

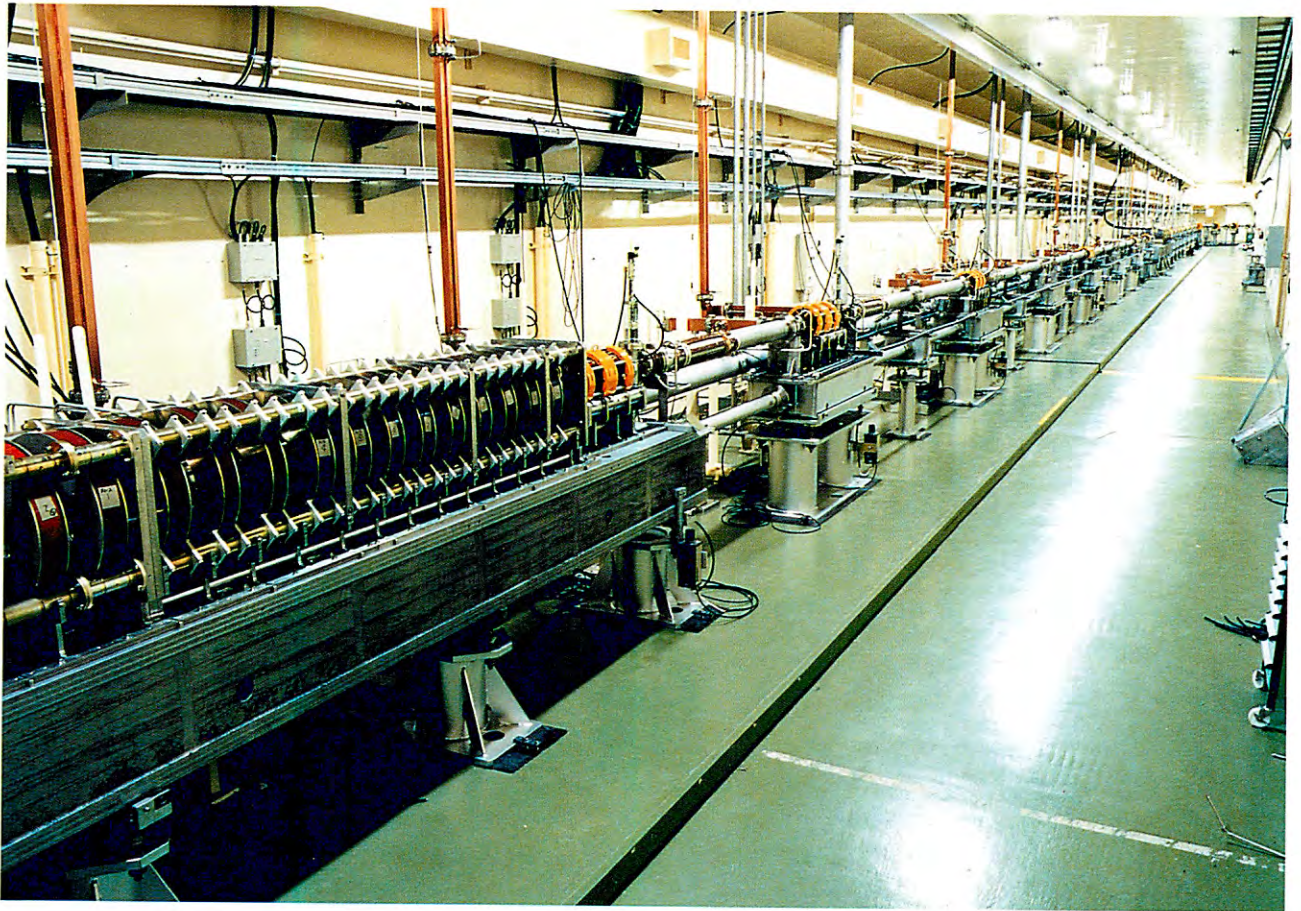
Meetings

Future progress of new research fields which will be possible by using a light source with high intensity and high brightness in VUV and soft X-ray regions	October 20-21, 1986
Workshop on a plan of super-synchrotron radiation source for the next generation	November 4-5, 1986
4th Photon Factory symposium	November 6-7, 1986

Publications

PF news	ISSN 0288-691X	Vol.4, No.1-5
---------	----------------	---------------

Injector Linac Department



View of the positron generator

From the left, the high-current 200 - MeV electron linac, the positron production target and the 250 - MeV positron linac.

1. INTRODUCTION

This volume is the fourth activity report of the Photon Factory. It now seems timely to review the linac itself and its operational performance.

The linac is a full energy injector for the PF 2.5-GeV storage ring as well as an e^-/e^+ injector for the e^-/e^+ collider TRISTAN accumulation ring.

Construction of the 2.5-GeV electron linac started in April 1978 as a four-year program; just after its completion in 1982, construction of the positron generator was started as a three-year program.

Since the linac serves an injector for the rings, high beam stabilities are most desirable.

In order to obtain stable linac beams, a high level of stabilization for the acceleration rf field and the beam focusing magnetic field is required.

Also, a high current level for the beam breakup threshold is necessary, since even at a lower current than that of the threshold, a flicker of profile or position of the beam is often observed as a germ of the breakup in such a long linac. Consequently, the general design philosophy for the linac was from the beginning based on obtaining stable and reliable operation. Then, the structure was simplified in order to reduce costs and to facilitate construction, operation and maintenance. The principal parameters of the electron and positron linacs are listed in table 1.1.

The linac comprises a 35-MeV injection system, a 400-m long main accelerator, a beam-switching system, a central control system and a 250-MeV positron generator which comprises a 200-MeV high-current electron linac, an electron-positron converter system and a 250-MeV positron linac. The 250-MeV positron beam is injected at the 250-MeV point of the main accelerator.

The 2.5-GeV electron beam has been provided for the PF ring since June 1982 and for the TRISTAN-AR since October 1983, respectively. The positron generator has been in commissioning since October 1985. Operation times for each fiscal year are given in Fig. 1.1.

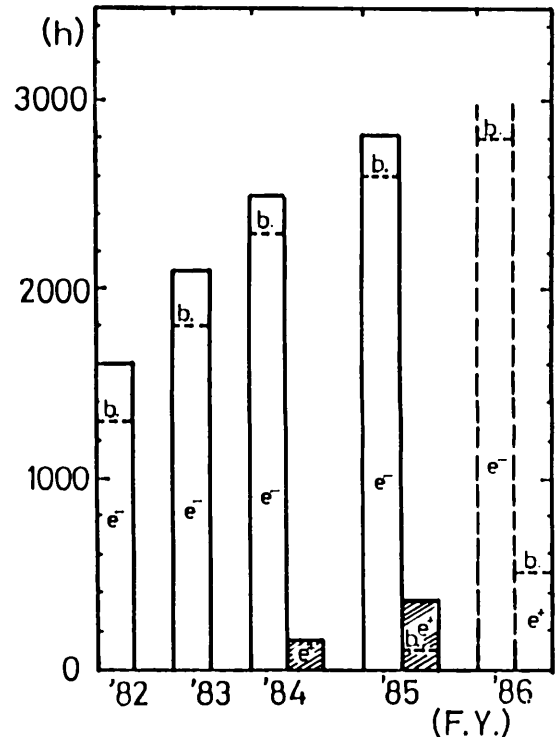


Fig. 1.1 Yearly operation time of the linac from FY 1982 to FY 1986. The dashed lines (indicated by b.) are operation times based on the budget.

Table 1.1 Principal parameters of the 2.5 GeV linac and the positron generator.

Parameters	2.5 GeV electron linac		Positron generator			
	Design	Achieved	200 MeV e^- linac		250 MeV e^+ linac	
			Design	Achieved	Design	Achieved
Energy (GeV)	2.5 (50mA)	2.54 (55mA)	0.200	0.200	0.250	0.250
Beam current (1.5 μ s)(mA)	50 (2.5GeV)	max 400 (1.8GeV)	10,000	7,000	>10	27
Beam pulse width: short	2ns	1.5ns	1.0ns	1.5ns	1.0ns	1.5ns
long	2.0 μ s	2.5 μ s	10ns	10ns	10ns	10ns
Repetition rate (pps)	max 50	1 - 20	50	20	50	20
Accelerator guides	Quasi-constant-gradient traveling wave types; $2\pi/3$ mode; 5types ^{a)}					
Operation frequency	2856 MHz					
Length of guides (m)	2		1.5, 2, 4		2, 4	
Total number of guides	160+2 (Injector)		1, 1, 5		4, 4	
Peak rf power/kly. (MW)	30	30	30	30	30	30
Number of klystrons	40+1 (Injector)		3		3	
Type of gun	Oxide cathode; Triode.					
Gun voltage (kV)	-100	-100	-150	-160		

a) 5 different size types of disk bore diameter

Most of the design performance values of the 2.5-GeV electron linac were satisfied during the initial operation. The linac had been designed to be able to accelerate beam currents of 50 mA to energies of 2.5 and 3.0 GeV with a total rf power of 840 and 1,200 MW, respectively.

During routine operation, the energy is fixed at 2.5 GeV and the injected electron beam currents for the PF ring and the AR are 30 - 50 mA (0.2 - 0.8 μ s, 1 pps) and 100 - 150 mA (1.5 ns, 10 pps), respectively.

Consequently, a total rf power of 840 MW is sufficient for ordinary operation. The energies of the injected beams for both rings are finely corrected by adjustments of the rf phase at the end acceleration unit. Since the beam breakup threshold current is sufficiently high (for example 300 mA for a 2.5- μ s beam pulse width), no indication of an instability has been observed during ordinary operation.

The energy spread at 2.5 GeV is less than 0.5 % for beams longer than 1 μ s; however, it spreads to 0.8 % for a 0.5- μ s beam since the width of the beam pulse corresponds to the filling time of the accelerator guides. On the contrary, it decreases to 0.1 % for short pulse beams (such as 1.5 ns).

The normalized emittance is less than 10 μ m \cdot mrad (2×10^{-3} μ m \cdot mrad at 2.5 GeV). The beam diameter is less than 5 mm and more than 90 % of the beam current passes through a 4-mm diameter hole.

The full energy injection to the PF ring shows an excellent advantage. Injection and stacking of the electron beam in the PF ring are very easy. Under ordinary operation the beam stacking rate is 2 - 3 mA/pulse. During the degassing process of the ring vacuum chamber exposed to the atmosphere for long time, a continuous injection of the full energy beams makes quick degassing of the chamber possible.

During routine electron beam injection to the PF ring, a long pulse beam (30 - 50 mA, 0.2 - 0.8 μ s and 1 pps) is provided for multi-bunch mode operation. In the AR, on the contrary, a short pulse beam (100 - 150 mA, 1.5 ns and 1 - 10 pps) synchronized with the beam revolution frequency is required because of the single-bunch mode operation.

In the PF ring, stored beams filling all of the rf buckets (312) cause an instability due to the ion-trapping effect. To reduce this instability, a partial-fill mode operation (filled up 2/3 buckets of all) is effective. For such an operation, synchronized injection is also required. During positron injection into the AR, the beam pulse width is the same as that for electrons; however the beam repetition rate is increased to 20 pps.

These operational modes are quite different from each other from a linac point of view. The switchover between them must be made as promptly, easily and reliably as possible.

To meet the requirement, special electron gun systems and a double synchronized trigger control system have been developed, since the frequencies of the linac (2856 MHz), the PF ring (500 MHz) and the AR (508.6 MHz) are independent of each other.

The first positron beam of 2.3 mA was accelerated to 250 MeV with a primary electron beam of 200 MeV, 1.6 A (10 ns) in July 1985. By the end of March 1986, the positron beam current was increased up to 10 mA (4 ns) at 250 MeV and 4.5 mA at 2.5 GeV.

In July 1986, a 250-MeV, 27-mA (1.5-ns) beam was obtained with a primary electron beam of 200 MeV, 7.9 A. It was mainly due to an increase in the gun voltage up to 160 kV and the use of a 119-MHz subharmonic buncher.

In November 1986, more than a 10-mA (1.5 ns) beam was obtained at 2.5 GeV. The beam stacking rate in the AR was 6 - 7 mA/min at a repetition rate of 20 pps.

The fault rate of the high-power klystrons was reduced to about 1 fault/41 kly.h. The window puncture was also improved. These troubles were cured by improvements in the klystron-fabrication process, TiN film coating on the ceramic window and by sufficient conditioning of the klystrons during their initial operation. The cause of such troubles was basically due to impurity gases (H_2 , O_2 , ...) contained in such materials as OFC, stainless steel and alumina ceramics, constituting the klystrons or high-power rf system.

A study of the high-power rf windows has advanced remarkably. High-purity, fine-grain and void-less ceramic windows coated with TiN thin film (\sim 50 A thick) have shown a high durability for multipactor electron bombardment. However, in such high-purity and fine-grain ceramics, metalizing is rather difficult. Consequently, the studies and tests regarding the metalizing process have been repeated in FY 1985.

Although breakage of the PFN capacitors of the klystron modulators had not been experienced until recently, a few capacitors were damaged during FY 1985.

One of the main reasons for the trouble was due to an inadequate adjustment of the PFNs. During the summer shutdown in 1986, the PFNs were readjusted to slow the risetime of the pulse and to reduce the rf phase modulation in the acceleration rf wave pulses. The readjustment was not only effective in improving the acceleration rf wave but also in reducing the peak value of the current flowing through each capacitor in the PFNs.

Another serious problem involved faults in the sub-booster klystron power supplies. Since any trouble in the sub-booster stops 8 high-power klystrons, the improvement also made a contribution to the reduction of the fault rate of the high-power klystrons.

In the positron generator, the design value for the positron current (> 10 mA, < 2 ns at 2.5 GeV) was already satisfied; however, the current at 2.5 GeV can be expected to be increased by at least 50 % with the improvements in the primary electron beam focussing, the electron-to-positron converter, the initial positron focussing and the 250-MeV beam-transport system.

2. OPERATION OF THE POSITRON BEAM

2.1 Outline of operation

After the first positron beam was accelerated to an energy of 250 MeV in July 1985, improvements of the positron generator have been continued in order to obtain more current and more stable operation. The chronological progress is as follows.

- (1985)
- 10/08 Installation of the 119-MHz subharmonic buncher (SHB).
 - 10/25 First acceleration of positrons up to 2.5 GeV.
 - 10/30 First injection of positrons into the TRISTAN accumulation ring (AR).
 - 12/20 First injection of positrons into the PF storage ring.
- (1986)
- (Jan. -March) Operation of the SHB system, and development of the 4-ns grid pulser for the gun.
 - 3/20 Colliding of positrons and electrons in the AR.
 - (May -June) Adjustment of 2-ns positron beams with the 4-ns grid pulser and the SHB system.
 - 6/26 First injection of 2-ns positron and electron beam into the AR (a single bunch beam in the AR).
 - (July -Aug.) Test for rising the gun high voltage from 115 to 160 kV.

The operation time from October 1985 to July 1986 was about 800 hours. Adjustment of the positron generator itself was made independently of the 2.5-GeV linac operation; however, positron acceleration by the 2.5-GeV linac was performed using machine-study time, which has been assigned to the linac department by 3 shifts (1 shift = 8 hours) per 30 shifts in every two-week operation period. Injection to the PF and AR has been performed using the respective machine-study times.

2.2 The positron generator

Increasing of the positron intensity

Figure 2.1(a) shows an increase of the positron intensity at the end of the positron generator (250 MeV) during the course of the past year. In July 1985, the positron intensity was only 2.3 mA; however, by July 1986, it had been increased by about 10 times. This was due to increases of the primary electron beam current (Fig. 2.1(c),(d)) as well as gradual improvements in the electron-to-positron conversion rate (Fig. 2.1(b)).

The large increase of the primary beam was obtained by improvements and adjustments of the injection system (the gun, the SHB, and the transport system) of the positron generator (described in the section of 4.2 injection system).

The conversion rate was increased by the following improvements: (1) adjustment of the

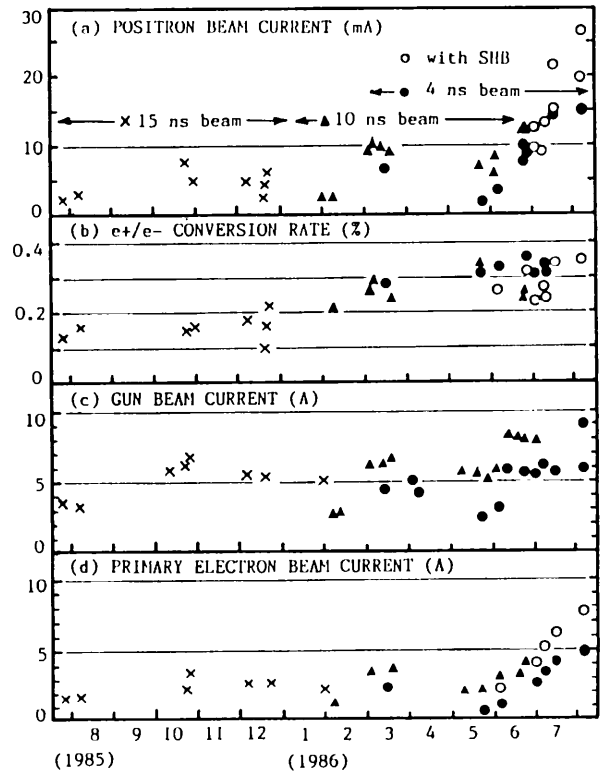


Fig. 2.1 Improvement of the performance in the positron generator during July 1985 - August 1986. (a) Increase of the positron intensity at the end of the positron generator (250 MeV). (b) Electron-to-positron conversion rate at the end of the positron generator. (c) Gun peak current. (d) The primary electron beam current bombarding the positron production target.

primary beam size on the positron production target, (2) addition of one more quadrupole doublet about 3.4-m upstream of the target, (3) improvement of the primary beam by increasing the gun voltage, and (4) adjustment of the positron focussing system. The positron yield is proportional to the primary electron beam power, captured positron momentum width and square of the (one-plane) acceptance; according to this formula, the specific yield of the positron generation in the KEK is within a reasonable range as compared with other machines in the world.

Improvement of the pulse width

Though the single bunch beam in the AR is less than 2 ns in width, at first a rather wide (15 ns) beam was used for adjustments, since it was easier to observe such a wide beam at that time. However, as improvements of the gun and adjustments of the SHB system progressed, more intensive and shorter positron beams could be accelerated.

Transport of the high current primary electron beam

In order to obtain more positrons, it is obviously necessary to increase the power of the primary electrons bombarding a positron production target; however, it becomes more difficult to transport the primary beam without loss as the intensity increases.

Figure 2.2 shows the ratio of the peak current at the target to the current at the gun: without the SHB system the ratio is around 0.6 owing to the capture efficiency of the 2856-MHz bunching system. Also, with the SHB the ratio increases to roughly 1.2 at maximum, since the SHB compresses the pulse width of the gun beam from 4 to 2 ns and increases the peak current twice at the entrance of the 2856-MHz bunching system. In the figure, it appears that the ratio decreases as the gun emission intensity increases to about 10 A. The reason for such a tendency is considered to be that the emittance is increased as the current increases, though a quantitative analysis has not been performed.

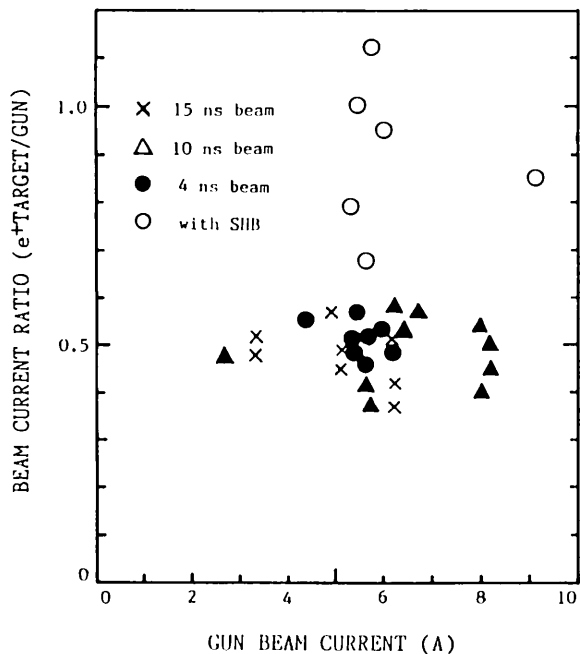


Fig. 2.2 The ratio of the peak current on the positron production target to the peak current at the gun.

The primary-beam transport system was designed with an emittance ($0.015 \pi \cdot \text{MeV}/c \cdot \text{cm}$) three times as large as the PF 2.5-GeV linac design value and the maximum beam radius of 0.7 cm; therefore, it is now necessary to improve the transport system so as to make the adjustment much easier.

Importance of the primary beam quality

It is important not only to increase the beam intensity but also to make the beam size

small; in the KEK positron generator, the design value of the primary electron beam radius on the target is 1.2 mm. Therefore, a large part of the positron conversion adjustment is to tune the transport system of the primary electron beam and the beam radius on the target. A large emittance and a long bunch length probably make the beam size large.

Figure 2.3 shows the conversion rate vs. the primary beam current. This figure clearly shows that though the primary electron beam current is increased by using the SHB system, the positron yield does not always increase to the expected value, owing to decreases in the conversion rate. Before July 1986, this situation had not been improved, even though it took much time to adjust the primary beam. In July 1986, after the high voltage of the gun was increased from 115 to 160 kV, the situation changed drastically; this improvement increased not only the primary electron beam current but also the conversion rate (especially when the SHB system was used).

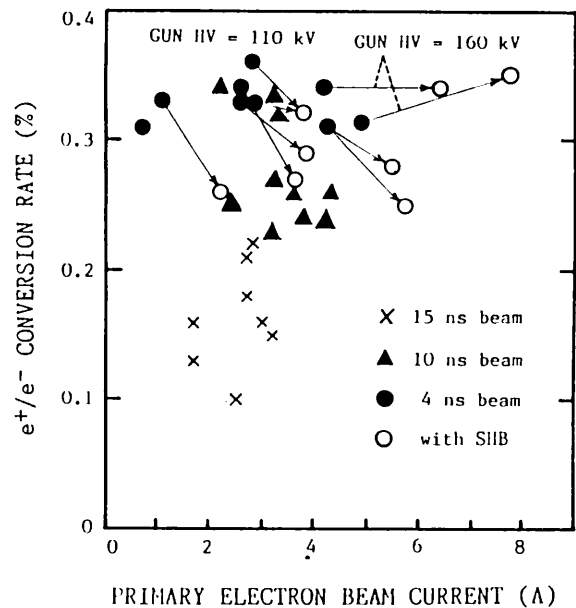


Fig. 2.3 The electron-to-positron conversion rate vs. the primary electron beam current on the positron production target.

Phasing

At first, the rf phasing of the positron generator was accomplished by observing the beam loading at the time of a long pulse electron beam ($1 \mu\text{s}$). Later, phasing became possible at a short pulse (4 ns) electron beam of several amperes; the automatic phasing system has been used since March 1985. For positron acceleration, the rf phase was first shifted by 180 degrees, and then adjusted a little further while observing the accelerated positron current. All rf phases of the positron generator were adjusted for those of the 2.5-GeV linac by changing the positron generator subbooster rf

phase, so as to increase the beam intensity in the 2.5-GeV linac.

2.3 Positron acceleration in the PF 2.5-GeV linac

Transmission of the positron beams

Figure 2.4 shows an example of the transmitted current along the positron generator and the PF 2.5-GeV linac. A positron beam of 250 MeV from the positron generator is transported to the 250-MeV point of the 2.5-GeV linac and accelerated up to 2.5 GeV; during the acceleration about one half of the current is spilled between the positron generator and the 500-MeV point. However, transmission from the 500-MeV point to the end of the linac is almost 100%.

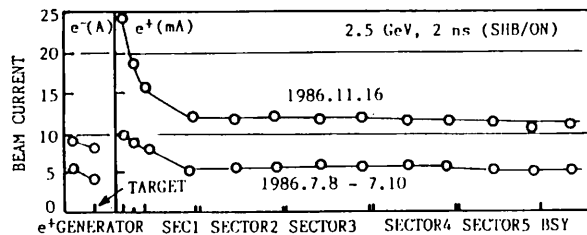


Fig. 2.4 An example of the transmitted current along the entire length of the positron generator and the PF 2.5-GeV linac.

Adjustment of the beam transport

When the first positron beam was accelerated up to 2.5 GeV, it took 10 shifts (80 hours) to adjust the beam transport downstream from the positron generator: the 30-degree bending transport line between the generator and the 2.5-GeV linac, and the 2.5-GeV linac transport. The reason to spend such a long time was as follows: (1) Adjustment of positron beam was very critical owing to the large emittance; (2) it is difficult to observe the positron beam profile owing to its weak luminosity; (3) small beam ducts in diameter and the misalignment made it difficult to transport positrons in the 30-degree bending system, and (4) the beam monitors of the 2.5-GeV linac were insufficient; only five screen monitors were installed at the end of each sector in every 80 m, and signals from the wall current monitors were possible to observe only at the subcontrol stations.

In April 1986, the beam-transport system was improved locally; then, the beam-monitor system in the PF 2.5-GeV linac was reinforced. Five more screens were installed at the middle point of each sector, 20D low-loss semiflexible coaxial cables were installed along the linac and signals from the wall current monitors could be observed at the main console station.

Owing to the improvement and the establish-

ment of the 2.5-GeV linac transport parameters, the adjustment had been concentrated to the rf phasing and the beam transporting between the two linacs (the positron generator and the PF 2.5 GeV linac); consequently, the time required for an adjustment has been greatly shortened.

2.4 Injection to the AR

Injection into the AR has progressed in due order: (1) 15-ns positron injection (October 1985), (2) alternate injection of 10-ns positron and 2-ns electron beams (March 1986), and (3) alternate injection of 2-ns positron and electron beams.

Intensity of the positron beam

In October 1985 and March 1986, injected positron currents were about 1.3 and 3 mA, respectively, at the end of the linac. However, these intensities were not sufficient for the AR operators to smoothly adjust the AR injection line (about 350-m downstream from the linac), since the AR injection line could only be adjusted using the screen monitors. By June 1986, the positron intensity was increased to about 5 mA; on the other hand, the charge quantity per pulse decreased, since the pulse width was shortened from 10 to 2 ns in order to accumulate a single bunch beam in the AR. Therefore, it was still difficult to adjust such beams. To solve this problem, a grid pulse switchover system of the gun was developed and an accurate injection became possible; that is, adjustment of the beam transport was made at first with 10-ns sighting beams and then a 2-ns beam was injected.

Energy spread adjustment of the positron beam

Also, in June 1986, an effort to decrease the beam loss between the linac and the AR was made in co-operation with the AR department. Up to that time, the energy and the energy spread of the linac beam had been adjusted only by screen monitors installed along the AR injection line. These could also be observed in the linac main control station. However, they did not have a sufficient sensitivity for observing the dispersion of the positron beam of several milliamperes. It turned out that large numbers of positrons were spilled in the AR injection line (for example, about 15 pC/pulse decreased to 2 pC/pulse). The beam loss was considered to be due to a much larger momentum spread of the linac beam than the momentum acceptable by the AR injection line (full width 0.5 % acceptable).

In order to improve this situation, first, one of the beam pipes installed at the widest momentum dispersion region was replaced by one with a larger diameter. Second, downstream from that region a current monitor was added and the image of signals on an oscilloscope was sent from the AR control station to the linac. Up to the present, this monitor has made diagnoses of the linac beam much easier, and transmission has been improved to at the maximum about 70 %.

At the same time, in June 1986 the relation between the number of bunches in the AR and the linac beam pulse width was studied together with the beam stacking rate in the AR (Table 2.1).

Table 2.1 The number of bunches and the beam stacking rate in the TRISTAN accumulation ring (AR) for various pulse width of the linac positron beam (at 4 to 5 mA peak), studied in June 1986.

beam width	number of bunches	beam stacking rate
10 ns	4	2 mA/min
4 ns	2	
2 ns	1	1.2 mA/min

2.5 Beam switchover

Since January 1986, it was necessary to switchover the following beams: (1) positron beam to the AR (10 or 2 ns, 10 pps), (2) electron beam to the AR (2 ns, 10 pps), (3) electron beam to the PF ring (0.8 μ s, 1 pps), and (4) electron beam to the beam dump for the high-energy physics experiment (500 MeV and 2.5 GeV, < 1 μ s, temporarily from January to July).

For these different kinds of beams, the following parameters had to be changed from one beam to another: (1) beam transport parameters, (2) gun triggers, (3) pulse repetition rates, (4) pulse width (short or long pulse), (5) rf phase and timing.

When the positron beam was switched off and the beams from the PF 2.5-GeV linac gun were switched on, the 250-MeV bending magnet of the beam line of the 2.5-GeV linac was degaussed in the following manner: The exciting field of the magnet was changed so that the polarity and the digital-to-analog converter (DAC) values of the power supply were set at 4096, -1024, 256, -64, 16, -4, and 0 (in that order). In the injection of March 1986, this manner was performed manually in the positron subcontrol station; however, since the next injection in May 1986, this has been automatically performed using a single board computer installed in the local control device of the magnet power supply communicating with a personal computer in the main control station. In manual changing, it required much effort by two operators; however, in automatic changing it requires only a little effort by one operator. It took about 3 minutes for automatic degaussing. The reproducibility of the beam states was confirmed by switching several times for each beam.

2.6 Further improvement of the positron beam

The positron intensity had been rapidly increased in July 1986; it was expected that more than 10 mA of positrons would be accelerated to the end of the linac during October. Further-

more, since the repetition rate of the positron beam is to be increased from 10 to 20 pps, the injection rate to the AR will be greatly improved within the next period of scheduled operation.

In the near future, a more intense positron beam will be required in order to store it in the PF ring. Therefore, further improvements are needed to increase the positron intensity and to realize more reliable and easier operation.

As for the beam-transport system, it is necessary to increase the positron conversion ratio by improving the positron focussing field distribution just downstream from the target; the field-free space between the pulsed field (12 kG) and the following DC field (2 kG) is to be filled up, and the field distribution shape is to be changed to more suitable one. The other is to decrease the beam loss downstream from the positron generator; the 30-degree bending transport line and the 250-MeV region of the 2.5-GeV linac are to be improved and reinforced.

3 ELECTRON LINAC

3.1 Operational status of microwave source

In the period between August 1985 and July 1986, the microwave system had been stably operated with a total operating time of about 3,300 hours. Various improvements were made in the sub-booster amplifiers and the high-power klystron modulators. Vacuum tubes (Eimac 4PR60C) used in the sub-booster modulators as final-stage switching devices were replaced with 4PR1000A's to prevent high-voltage faults which sometimes occurred. The modulators for high-power klystrons had operated stably except for a few problems. The major troubles were failures in the trigger pulsers (TRIG-II) for driving the main thyratrons and capacitor breakdowns in the pulse forming networks (PFN). Some of the TRIG-II thyratrons were replaced with SCR's which were expected to have longer life. Until recently, no breakdown of the PFN capacitors had been experienced, but several capacitors were broken during this operational period. They were broken due to arcing on one of the capacitor elements. The best way to solve this problem seems to be to use new capacitors having a higher working voltage. Some capacitors which have a capability for a higher voltage operation are being fabricated. It is also expected that this kind of problem can be reduced by some modification of the PFN circuit. Inductors were added on the main-thyratron anode to suppress the high-frequency component of the current. Furthermore, the respective time constants for the first five sections in the PFN were chosen so as to be longer in order to protect capacitors from rapidly changing high currents. These modifications were finished in the summer of 1986. Microwave phase modulations on the

pulse flat top were also improved drastically by these modifications since the slow rise time of the pulse waveform decreased the undesirable phase modulation due to the sharp reflected waves from the couplers of the accelerator guides.

Twenty-three microwave ceramic windows of the waveguide system were replaced by new TiN coated windows. These were fairly durable under multipactor electron bombardment; their initial-conditioning time after installing became fairly short. A study of the rf window has advanced.

Fourteen high-power klystron assemblies were replaced during this period. The details are as follows: Three of them were replaced because of problems with high-power pulse-transformer assemblies (a capacitive divider for monitoring high-voltage pulses, a filament transformer and water leakage). One of them was replaced owing to contamination on the surface of the ceramic window. The others were klystron failures (10). The cause of all these problems was internal arcing.

Table 3.1 shows the operational performance of tubes during the past five years (up to July 1986). Eighty-five tubes have been used since 1982. Thirty-nine tubes failed during these periods and their MTBF (Mean Time Before Failure) was 13,700 h. The mean age of living tubes was 4,400 h.

Table 3.2 shows a more detailed analysis of the operational status corresponding to the

respective tube production years. This table also shows that the main causes of tube failures were internal arcing and window puncturing. Also, there is a tendency for the MTBF to gradually increase year by year owing to improvement efforts.

An important factor concerning linac operation is the klystron fault rate, since the faults lead to interruptions of beam injection into the PF ring or the TRISTAN accumulation ring. Table 3.2 also shows the fault rate corresponding to each production year. Table 3.3 shows the fault rates and the applied voltages from October 1982 to July 1986. It also indicates a tendency that the fault rate has decreased year by year.

Efforts to improve the tubes have continued by the manufacturer and KEK. One of the major improvements in tube production from August 1985 to July 1986 was the introduction of a double-vacuum furnace. These tubes have been installed in the klystron gallery and operated. Until 1985, since tubes had been produced using the baking furnace filled with the forming gas (92% nitrogen + 8% hydrogen), the hydrogen was not

Table 3.1 Cumulative usage hours during the past 5 years.

Period	Total Tubes	Failed Tubes		Living Tubes		MTBF
		No.	Mean Age (h)	No.	Mean Age (h)	
1982/4 - 1983/3	53	11	1,300	42	2,900	13,500
1983/4 - 1984/3	63	20	2,300	43	4,200	11,200
1984/4 - 1985/3	70	25	3,100	45	5,800	13,600
1985/4 - 1986/3	77	32	4,000	45	7,500	14,400
1986/4 - 1986/7	85	39	4,400	46	7,400	13,100

Table 3.3 Operational Status (fault rate and voltage)

Year	Period Month	Fault rate (per day per 41 tubes)	Averaged applied
			voltage (kV)
1982	10 - 12	3.5	236
	1 - 3	4.4	238
1983	5 - 7	4.6	239
	10 - 12	3.3	241
	1 - 3	2.6	243
1984	5 - 7	2.4	242
	10 - 12	2.6	241
	1 - 3	2.1	239
1985	5 - 7	1.5	241
	10 - 12	1.6	238
	1 - 3	1.6	237
1986	5 - 7	1.9	240

Table 3.2 Status corresponding to the year of production. "Standby" tubes are those waiting for retesting. "Unused" tubes are those which have not been used in the klystron gallery at all.

Year	Total No.	Living Tube				Fault rate per day	Voltage (kV)	Failed Tubes			Mean Age(h)		MTBF	
		No. of Working Tubes		No. of Non-working Tubes				No. of Total Tubes	Cause			Failed Tubes		Living Tubes
		PF	Positron	Standby	Unused				Arcing	Window	Others			
1979	4	0	0	0	0		4	2	1	1	3902	0	3902	
1980	20	6	0	1	0	0.9	238	13	7	5	1	4033	11442	10193
1981	20	8	0	2	0	0.7	240	10	6	2	2	4663	12409	17072
1982	9	3	0	1	0	0.7	238	5	4	1	0	4181	8690	11133
1983	13	8	2	0	0	1.7	238	3	3	0	0	6019	7858	29593
1984	13	3	4	0	2	1.0	241	4	4	0	0	4048	4314	7284
1985	12	11	0	0	1	0.8	240	0	0	0	0	0	1548	0
1986	4	2	0	0	2			0	0	0	0	0	0	0

completely evacuated before pinching off the tube. Using the new vacuum furnace, the final pressure in the tube before pinch-off was considerably decreased. It was also observed that outgassing at first heater operation was kept at a very low rate. Since the major causes of arcing possibly come from internal residual gases, it is expected that these tubes will run more stably.

The development of an impregnated cathode has also continued. This cathode can regain its original emission level by a proper reactivation after exposure to air. Most of the excess barium and contaminations in an impregnated cathode evaporate during the first few hours. Therefore, it is possible to operate it in a separate envelop in order to get rid of the excess materials before installing it in a final tube. This enables us to keep the inside of the tube clean. However, its working temperature is higher ($\sim 1000^\circ\text{C}$) than that of an oxide cathode; there are various problems concerning thermal shielding of the assembly and processing of the materials. The impregnated cathode, itself, had already been fabricated and the housing of the test diode for this cathode was also completed. Its study is in progress. Whole assemblies will be completed and tested in the near future.

3.2 Phase control

In order to maximize the accelerated beam energy and to minimize the energy spread, centers of accelerated electron beam bunches must be on the crests of the rf accelerating wave. Generally, this requirement is satisfied by adjusting the phase of the accelerating wave; this operation is called "phasing".

AT the KEK 2.5-GeV linac a beam-induction method has been adopted for phasing. This technique utilizes phase comparisons between a beam-induced wave and an acceleration rf wave passed through an accelerator guide. The beam-induced wave can be observed by changing the pulse timing for the klystron to the standby mode which is delayed $84 \mu\text{s}$ from the acceleration mode. The phase correlation between these two waves can be measured by comparing the respective waves with the reference cw signal. All phase shifters for the klystrons are adjusted according to the principle that the phase difference between both waves should be 180° . The biggest advantage of the beam-induction method is its high sensitivity; thus, this method is most suitable for fine tuning and is adopted at long linacs.

The phasing system was already reported in the activity report 1983/84; however, this system has been improved in order to automatically execute phasing during 1985. In addition, the improvement and re-tuning of the PFN's (see another section) reduced phase modulation on flat-top of the klystron output waves; this made possible an easy adjustment of the phase.

Phasing System

An outline of the rf system and the phase-control system is given in Fig.3.1. The 41 klystrons are divided into 5 sectors, each of which has a sub-booster and a sub-control station.

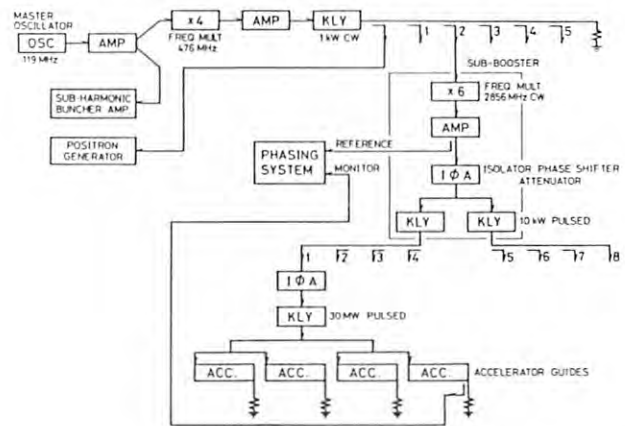


Fig. 3.1 Outline of the rf system and the phasing system.

Eight rf signals picked up at output ports of the accelerator guides in one sector are sent to a coaxial switch box located in the sub-control station; two of them are selected for monitoring or phasing. A reference signal (CW) from the s-band amplifier installed in a sub-booster and the selected rf signal from the switch box are fed to a phasing unit (Fig. 3.2). The s-band amplifiers and the multipliers are well-tuned in order to maintain good phase stability. In the phasing unit, the phase difference between two input signals is mixed and converted to a pulse voltage signal by a phase detector. This phase-difference signal is amplified and held by a sample and hold circuit which is triggered by a pulse synchronized with a trigger pulse of the klystron modulator. All functions of this unit are controlled by a phasing unit controller which has a

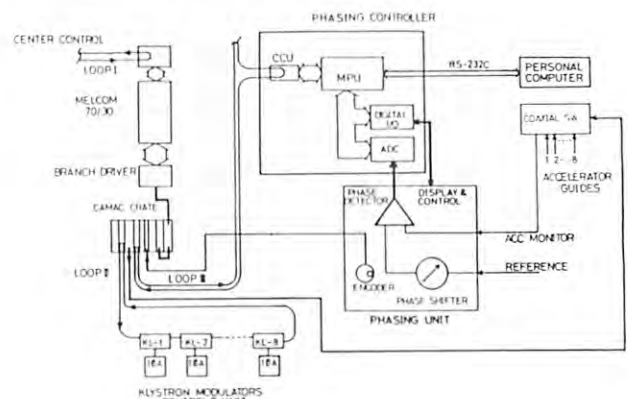


Fig. 3.2 Block diagrams of the phasing unit, the phasing controller and the communication system.

microprocessor, a communication controller, a digital I/O circuit and an A/D converter for the phase signal. A small personal computer also communicates with the phasing unit controller through an RS-232C serial line. The program for auto-phasing is automatically loaded into the computer during resetting of the system; the procedure can be easily executed in response to a request from an operator in the main control room.

Phase Detector

The phase detector, which is the key of this system, was required to have an accurate null output at a 90° phase difference. In order to satisfy this requirement a precise phase detector was recently developed.

This detector consists of a precise 3-dB microwave power divider and a well-matched pair of diodes. The power divider is a micro-strip line hybrid circuit and has a completely symmetric structure. The input signal is divided into two signals that have exactly equal amplitudes and a phase difference of 90°.

When two signals with amplitudes of E_s and E_r are fed, respectively, to the two input ports, the differential output V of the diodes can be expressed as

$$V \propto (E_s^2 + E_r^2 + 2E_s E_r \cos\phi)^{n/2} - (E_s^2 + E_r^2 - 2E_s E_r \cos\phi)^{n/2}$$

where ϕ is the phase difference between E_s and E_r , and the diodes are assumed to have the same response of $v \propto E^n$. At $\phi = 90^\circ$, this formula gives a V of zero and a sensitivity $|\partial V/\partial \phi|$ that is maximum. Figure 3.3 shows a typical example of a detector phase error at $\phi = 90^\circ$. Measured errors exist within $\pm 0.5^\circ$ over the range of input power from 30 μ W to 30 mW at a reference power of 10 mW.

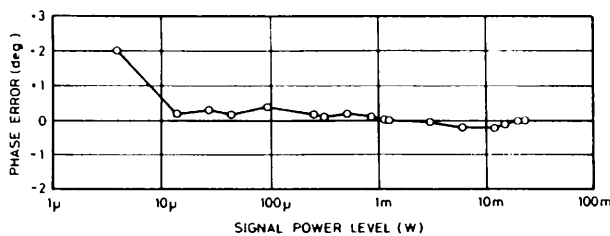


Fig. 3.3 Phase errors of a detector at $\phi=90^\circ$ plotted as a function of signal power levels at the reference of 10 mW.

Auto-phasing

A phase difference of 180° between a beam-induced wave and an acceleration wave is realized by the following two-step procedure. First, the phase of the reference signal is adjusted to be 90° away from one of a beam-induced wave at the standby mode. Second, the phase difference between an acceleration wave and the reference signal is also tuned to be 90°.

In order to develop an auto-phasing program which executes the above procedure, response characteristics of the system should be well considered. For example, the phase shifters to be adjusted are controlled according to a command from the phasing controller; however, the response delay caused by the communication of the system prevents a real time control of the phase shifters. This limitation of the phasing system obliged us to develop a program using the iteration method described below.

In Fig. 3.4, the output signal V of the phase detector is illustrated as a function of the phase difference ϕ between two input signals.

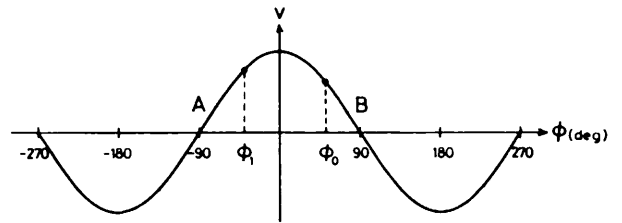


Fig. 3.4 Illustration of the output signal V of the phase detector vs. the phase difference ϕ .

First, phasing of the reference signal is executed at the standby mode. We suppose that the phase difference between the beam-induced and reference waves should be adjusted at the point A, $\phi = -90^\circ$ (or B, $\phi = 90^\circ$) and the initial phase difference ϕ_0 exists in a region $(-270^\circ, 90^\circ)$. The A/D converter takes the reference phase signal V and the value is checked as to whether to be positive or negative.

If $V > 0$, the phase shifter should be rotated as ϕ decreases by 90° .

If $V < 0$, ϕ should increase by 90° .

This operation causes a new ϕ_1 to exist in a region $(-180^\circ, 0^\circ)$. Taking V again, the phase shifter is operated according to the measured V as follows:

If $V > 0$, ϕ decreases by 45° .

If $V < 0$, ϕ increases ϕ by 45° .

Then, a new ϕ_2 will be found in a region $(-135^\circ, 45^\circ)$. After operating l times the new ϕ_l should be $-90^\circ \pm (180^\circ/2^l)$.

Next, the klystron wave should be phased at another point B, $\phi = 90^\circ$ (or A, $\phi = 90^\circ$) in the acceleration mode according to the same procedure mentioned above; but, IFA has to be adjusted as ϕ increases if $V > 0$ (inversely for the phasing of the reference signal).

The output signal from the phase detector contains noise which is caused by firing of the modulator thyratrons, random noise and dc offset as well as the pure phase signal. Therefore, the system needs reductions of these components which disturb accurate phasing. In our case we achieved sampling of the signal in the standby mode without the beam and subtracted this value from the measured phase signal in order to obtain a real phase.

At first, this auto-phasing program was expected to be revised sometimes; thus, a program written in BASIC language was installed in the small personal computer connected to the phasing controller.

The output waveforms from the phase detector are shown in Fig. 3.5. Figure 3.5 (a) is the phase signal of the beam-induced wave before reference phasing; the lower waveform in Fig. 3.5 (b) represents the phase signal after klystron phasing. Beam loading on the acceleration rf wave is also presented in Fig. 3.5 (b) in order to indicate the timing correlation between the beam and the phase of the klystron wave.

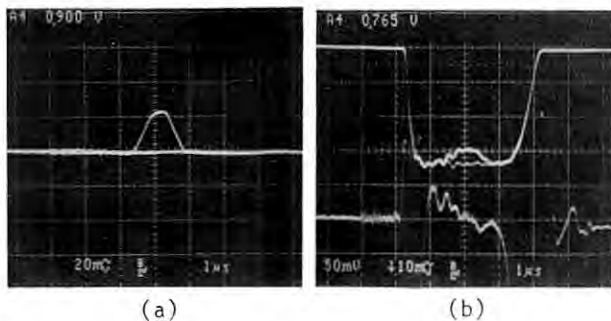


Fig. 3.5 Waveforms of the output signal v from the phase detector (amplified by 10). (a) Phase difference between the beam-induced and reference waves (at the standby mode) before reference phasing. (b) Upper: The waveform of the acceleration rf wave with the beam-loading. Lower: The phase difference ($4^\circ/\text{div}$) between the klystron wave and the reference (at the acceleration mode) after klystron phasing.

Results of autophasing for 41 klystrons are described as following:

1. Easy phasing is achieved.
2. The adjusting time was reduced to about one half of that for the manual procedure and was 10 minutes per 8 klystrons.
3. The phasing error can be evaluated within about $\pm 3^\circ$.

The advantage of this phasing system is the simple construction and the simple procedure due to microcomputer control.

The long adjusting time is mainly caused by the mechanical drive of the klystron phase shifter and the reference one. At present a new auto-phasing program is under development in order to reduce the adjusting time by one quarter.

Another disadvantage of the beam induction method is a decrease in the beam energy in the acceleration unit during the standby mode. Consequently, this method cannot be executed during injections into the AR or PF ring. For phase shifting of the klystron output wave, a new method should be developed, which is able to

be applied during injection, even if it does not have so good phasing accuracy. The phase of a beam-induced wave can be expected to be stable during a few weeks operation of the linac, as long as the injection system of the linac is locked. Therefore, the phase correlation between the reference and beam-induced waves needs not to be examined again after the initial fine phasing of both waves at the start of operation; the phase correlation between the acceleration rf wave and the reference wave represents a phase shift of the klystron wave. This means that the phase drift of the klystron output wave can be determined without disturbing the beam energy at any time during operation if the corresponding initial phase of the reference wave is memorized; that phasing without the disadvantage may also be possible. These functions are now about to be combined with the new program.

3.3 Developments

Processing of signals from short-pulse beam monitors

A beam-current signal-processing system for short-pulse beams is now under development. This system will utilize the wall-current monitors already installed and will enable a simultaneous monitoring of the short-pulse beam current along the accelerator.

The short-pulse beam which is injected into the TRISTAN is monitored by wall current monitors and a fast oscilloscope (Tektronix 7104); each signal is selected by changing coaxial switches one by one. In order to make manipulation easier, simultaneous monitoring of short-pulse beams along the accelerator is necessary.

A new signal-processing system for short-pulse beam observations is now under development. Since a beam pulse width of 1.5 ns is too narrow for obtaining the pulse height by a simple and low-cost electronic circuit, a charge-sensitive analog-to-digital converter (ADC) for high-energy physics experiments was adopted to obtain an integrated beam current.

A module of this kind (LeCroy 2249) has been tested; it has been confirmed that the digitization linearity and the long-term stability are less than one percent. It can easily communicate with a computer through a CAMAC interface.

Each ADC is installed in each sub-control room and connected to a minicomputer. An input signal from a wall-current monitor is divided by a power splitter with a high isolation of 30 dB so as not to disturb signals to a waveform monitor oscilloscope. For monitoring the weak positron beam an amplifier with a 20-dB gain is inserted between the power splitter and the ADC. In order to provide a precise integration time gate, a generator for the gate signal synchronized with the beam timing was designed, with which the gate signal is selected either from two timings by a computer. The computer also can correct the beam current data for offsets of the circuit and noise effects. Then, these

corrected data are transferred to the main-control processor through a bit-serial communication network and displayed on the operator's console. A block diagram of this system is shown in Fig. 3.6.

One purpose of this system is the reduction of noise from klystron modulators, especially for observing weak positron beams. It is necessary to estimate the background with klystron outputs and without beams. Each component of the above system has been tested, but the total system has not yet been completed.

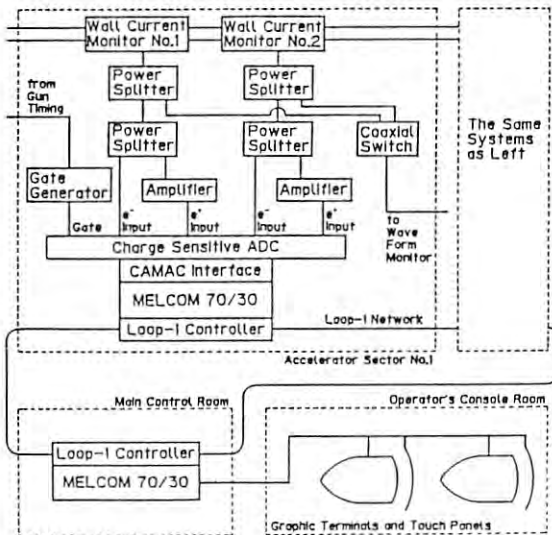


Fig. 3.6 Block diagram of the signal-processing system for short pulse beam observation.

Rf windows

(1) Introduction

Development work regarding alumina ceramic rf windows, which are used in s-band high-power klystrons and waveguide system of the linac, has been attempted in recent years. From the results of observations and experiments carried out in 1985, the following has been concluded concerning window-breakdown phenomena (Photon Factory Activity Report 1984/85):

- 1) Windows failed mostly as a result of punctures; such failures are initially generated on the alumina ceramic surfaces as holes by localized surface melting. These then grow to a puncture.
- 2) Optical emission from windows during rf operation has been found to be a luminescence of the alumina surface due to multipactor electron bombardment.
- 3) A TiN thin film having a low secondary electron emission (SEE) coefficient suppresses the multipactor electron bombardment when a film is coated on the alumina window surface.

These results indicate various directive methods for window improvements. During 1986, the following two terms have been newly adopted.

- 1) An alumina ceramic with lower porosity and less grain-boundary matrices (such as SiO_2 , CaO and MgO) has been used as a high-power rf window disk. Ceramic bulk singularities, such as voids and grain-boundary matrices, are considered to be dielectrically weak, especially when heated. Therefore, they seem to be starting points of puncture generation and routes of puncture propagation.
- 2) A TiN film of about 50-Å thickness has been coated on alumina ceramic disks.

Recently, window puncturing could be reduced; therefore, these two treatments are most likely to be effective for the prevention of detrimental damage to window disks.

For further advanced developments of the rf window, it is important to investigate the initial stage of surface melting and puncture generation; it is also necessary to determine how multipactor electron bombardment on the alumina surface is related to this stage. This report also describes a higher-power examination of windows using a resonant ring system and a measurement of the SEE coefficient of alumina window disks using a modified electron microscope.

- (2) Observations of the rf window installed in the waveguide system

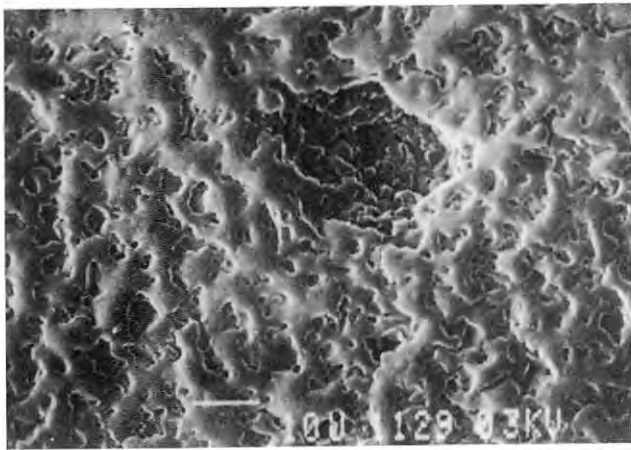
One of the luminescence patterns on the rf window is shown in Fig. 3.7; it was caused by the multipactor during rf operation with a power of 20 MW and a pulse repetition rate of 10 pps. A very bright spot of the luminescence can be seen. Multipactor electron bombardment on this surface area should be stronger than at other regions. Removed from the waveguide system after about 500-h operation, the ceramic disk shows a shiny area on the surface (Fig. 3.8). The location corresponds to that of the bright luminescence spot observed during rf operation. Figure 3.9(a) is a photograph of this area observed by a scanning electron microscope (SEM); it shows that the surface of the alumina



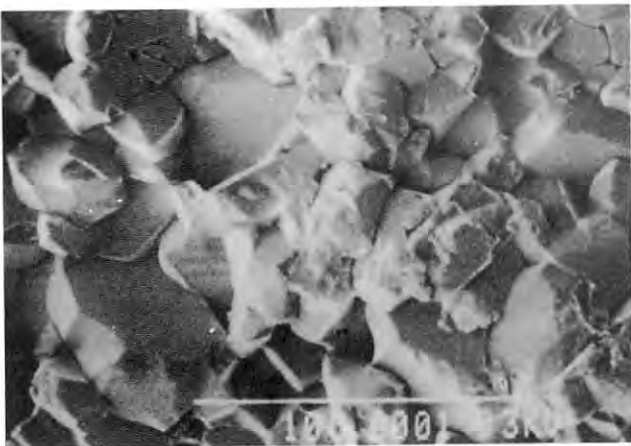
Fig. 3.7 Luminescence pattern from the alumina rf window disk during rf operation with a power of 20 MW. The rectangular waveguide cross-section dimension is 72.1mm×34mm.



Fig. 3.8 Surface of the alumina disk (92mm in diameter) after rf operation. A shiny stain can be seen with a location corresponding to the bright luminescence spot in Fig. 3.7.



(a)



(b)

Fig. 3.9 Microscopic photograph of a alumina surface observed by SEM. A 10- μ m bar is scaled.

- (a) Shiny surface area. The alumina surface is melted and a hole can be seen.
- (b) Unmelted alumina surface.

ceramic was melted. On the other surface area melted grains were not observed (Fig. 3.9(b)). In fig. 3.9(a), it can be seen that there is a small hole (diameter of about several tens of μ m) that does not penetrate to the inside (which would grow to a puncture if rf operation was longer). From these observations, it can be verified that the multipactor electron bombardment, when it is so strong as to cause the intensive luminescence, heats up the alumina surface, causes melting and induces a hole.

(3) Observations of the rf window installed in the resonant ring

More detailed information concerning the initial stage of surface melting has been obtained by window examinations using a higher power of the resonant ring system (Photon Factory Activity Report 1984/85). A schematic diagram of the resonant ring is shown in Fig. 3.10. The pumping system consists of a turbo-molecular pump (magnetic-bearing type), a sputter-ion pump and a titanium sublimation pump. The ultimate pressure after a bake-out reaches 10^{-10} Torr. The pressure is kept lower than 10^{-8} Torr, even during rf operation. The highest power ever obtained by this ring without windows was 300 MW with an input power of 18 MW. When the ring power reached near 300 MW, arcing breakdown took place on the plunger surface of the phase shifter.

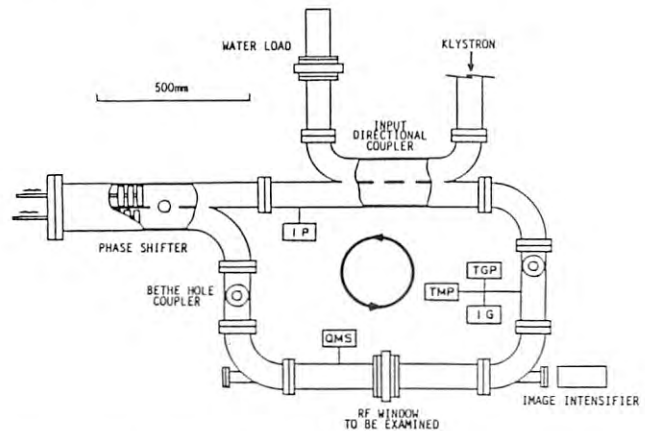


Fig. 3.10 Schematic drawing of the resonant ring. The built-up rf power moves in the counterclockwise direction.

The luminescence pattern on a window disk observed by a channel plate image intensifier is shown in Fig. 3.11 for a ring power of 200 MW. Several star-like spots can be observed as well as another areal luminescence pattern; the latter can also be seen with naked eyes; the former cannot. These bright spots appeared when the ring power was above 100 MW; occasionally, some of them disappeared and then again appeared. It should be considered that such localized bright spots represent luminescence caused by the spatially selective multipactor according to ceramic surface conditions. These



Fig. 3.11 Luminescence pattern on a window disk observed by an image intensifier (examined in the resonant ring with an rf power of 200 MW).

conditions should be spatially or locationally varied by contaminations, charge accumulation, temperature distribution and geometrical or ingredient singularities. These cause secondary electron emission and induce multipactor locally.

After operation for about 4 h with a power of 200 MW, one of the bright spots suddenly grew with a drastic increase in intensity. The image intensifier was saturated owing to the high brightness of the spot. It became so bright that it could be seen by naked eyes (Fig. 3.12). Once the luminescence intensity grew to the highest level, it never decreased. After removing the window disk from the resonant ring system, it showed a stain where this bright spot occurred during rf operation. This area on the surface was melted and a hole of about 100 μm in diameter was found (Fig. 3.13). Therefore, from the resonant ring experiment, it is again confirmed that the multipactor electron bombardment with such a bright spot causes surface melting and puncture generation.

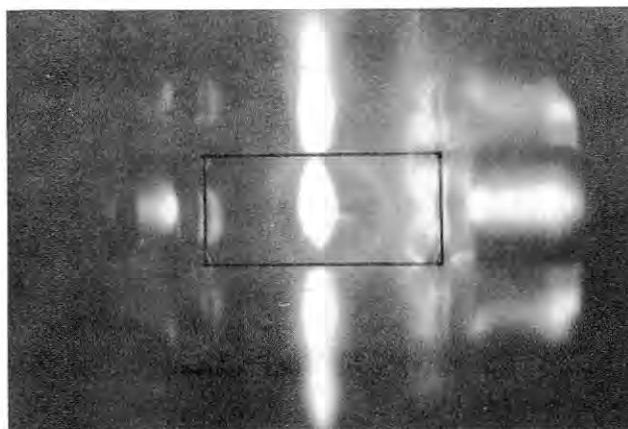


Fig. 3.12 Luminescence pattern after a drastic growth in the bright spot shown in Fig. 3.11.

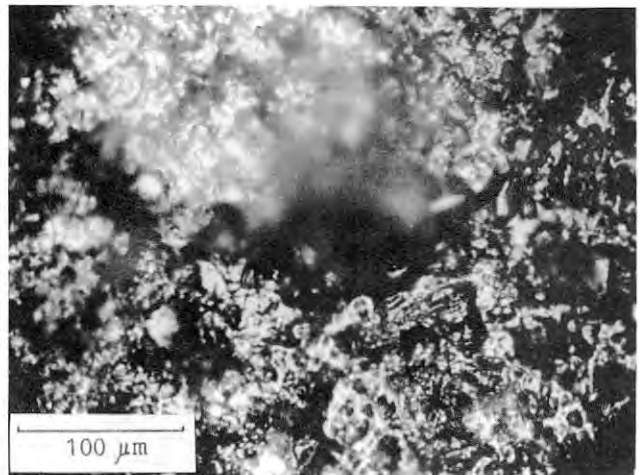


Fig. 3.13 Microscopic photograph of the alumina disk surface where the bright luminescence spot was observed during rf operation in Fig. 3.12. The surface is melted and a hole ($\sim 100 \mu\text{m}$ in diameter) can be seen.

The drastic growth of the local multipactor leading to the surface melting can probably also be explained by a spatially non-uniform surface condition. This is likely to be triggered by a localized phenomena: outgassing from the alumina surface or inside of alumina bulk, micro-discharge due to charge accumulation and degeneration of alumina caused by electron bombardment. Once the alumina surface is locally heated by the multipactor, $\tan \delta$ and electrical conductivity increase. These result in an increase of dissipated power. Thus, the alumina surface is heated more and more by itself. This "runaway" phenomena is drastic because of the lower value of thermal conductivity and contributes to surface melting and puncture generation.

Therefore, it should be concluded that a well-controlled surface condition is most important for the alumina window disks as well as less bulk singularities.

(4) Measurements of cathodoluminescence and secondary electron emission

For avoiding rf window breaks, it is necessary to suppress the multipactor as described above. A TiN thin-film coating on the disk is one of the useful methods. The SEE coefficient on which the multipactor occurrence strongly depends was measured on both coated and uncoated (bare) alumina disks. Also, cathodoluminescence (CL) spectra were observed in order to investigate the basic aspect of the alumina ceramic surface melted by multipactor heating.

The experimental apparatus using a scanning electron microscope is shown in Fig. 3.14. The primary-beam energy of the SEM can be continuously varied up to 30 keV. For CL experiments, an incident beam current measured by using a Faraday cup was kept constant at 12 nA and the photon emission intensity was recorded over a

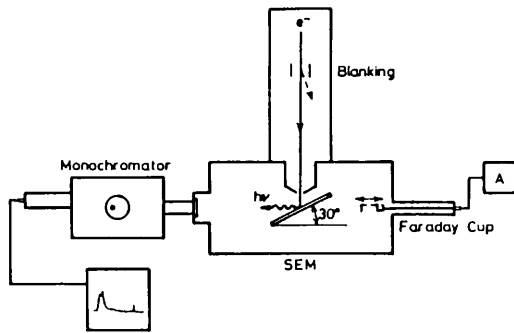


Fig. 3.14 Experimental apparatus for CL and SEE measurements.

wavelength range from 200 to 800 nm. For SEE experiments, a pulse modulated beam (100 pA current and 1 ms) obtained by a fast blanking unit was used in order to avoid surface charging effects. The total secondary electron emission coefficient σ can be determined as

$$\sigma = I_s/I_p,$$

where I_p is the primary current (100 pA) and I_s is the secondary electron current (including elastically scattered primary-electron current) captured by the Faraday cup.

Figure 3.15 shows the results of CL measurements for alumina ceramics: (a) bare, and (b) melted. The spectrum for the melted alumina has a characteristic structure at 410 nm. As the primary electron energy increases, the intensity of the 320-nm peak increases. This intensity increase is caused by a bulk volume effect; incident electrons enter deeply into the material. The intensity of the 410-nm peak most likely unchanged. This 410-nm peak can be considered as being due to a composition change and/or defect generation caused by melting only at the surface layer.

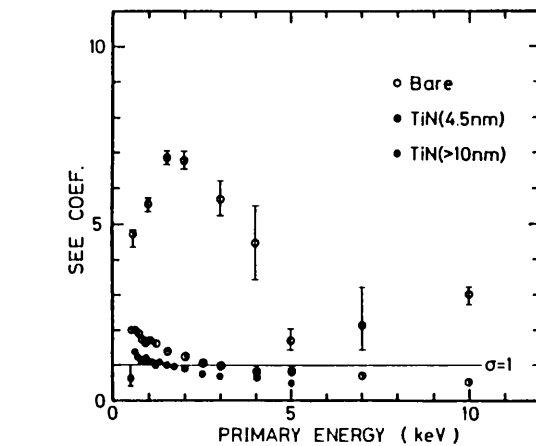
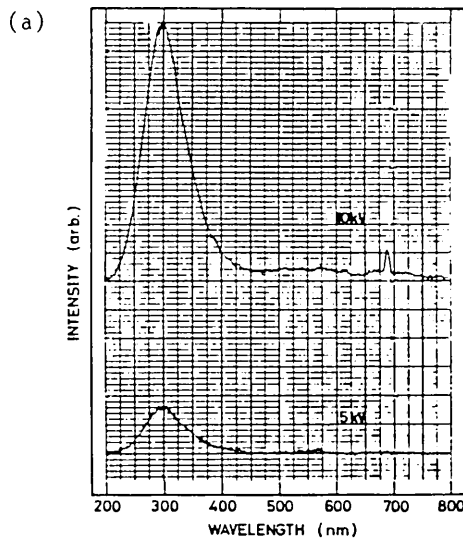


Fig. 3.16 Secondary electron emission coefficients of alumina ceramic disks.

Figure 3.16 shows σ values measured by SEM for bare and TiN coated alumina ceramic window disks. The primary energies were varied up to 10 keV. At the rf power level during practical rf operation, the kinetic energy of multipactoring electrons has been estimated to be less than a few keV. In Fig. 3.16, σ is fairly larger than unity for a bare alumina ceramic. On the contrary, it is near or less than unity for a TiN-coated type ceramic. Therefore, it is confirmed that TiN films sufficiently suppress SEE in the electron energy range where multipactor occurs.

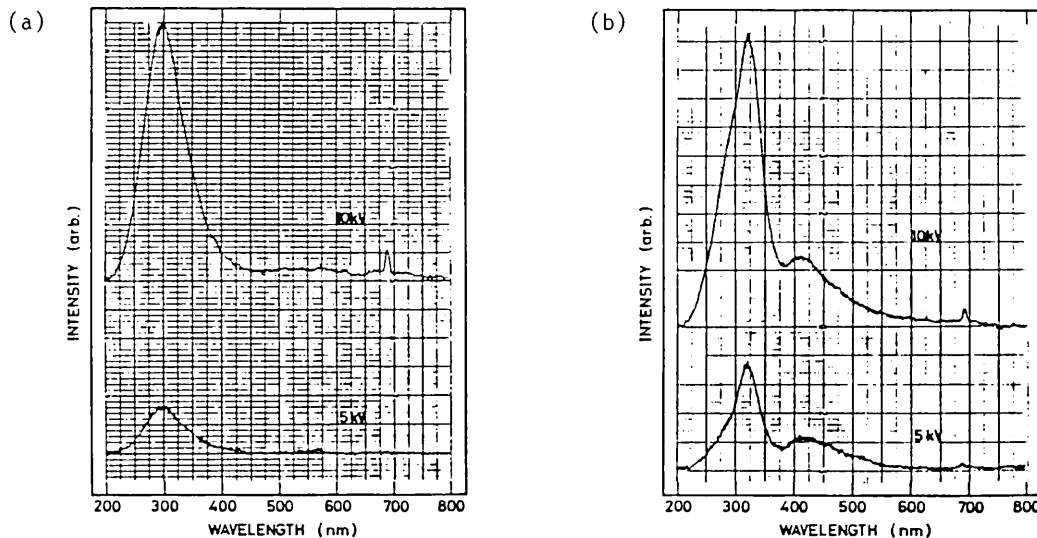


Fig. 3.15 Cathode luminescence spectra of alumina ceramic disks with primary electron energies of 5 and 10 kV: (a) bare, (b) melted.

4. POSITRON GENERATOR

4.1 Progress of the beam acceleration

During the initial stage of beam testing, accelerated positron beam intensity was so low that it was difficult to observe the beam with profile monitors; therefore, rather long pulse beams were used for the test. Meanwhile, the accelerated beam current has steadily increased owing to various improvements, such as those in the gun and focussing system.

In December 1985, a pulse peak current of 5 A was obtained from the gun with a pulse width of 15 ns (10 ns at FWHM). This beam was accelerated up to an energy of about 200 MeV and bombarded the positron production target, where the peak current of the beam was 2 A. In due course, it became possible to reduce the width of the beam due to the progress of the gun grid pulser. In June 1986, an emission current of 8 A was obtained with a width of 10 ns; an accelerated current of 4 A was obtained at the target. Waveforms of the accelerated beam observed at that time are shown in Figs. 4.1(a) and (b).

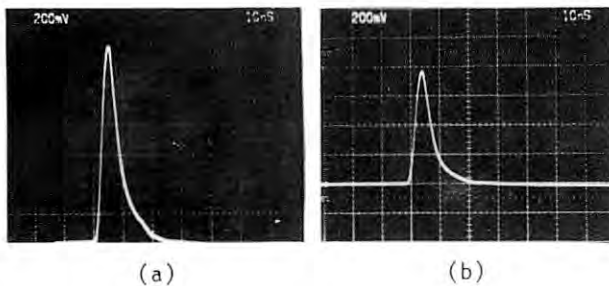


Fig. 4.1 Electron beam current signals.
 (a): Beam injected from the gun at a peak current of 5.6 A.
 (b): Accelerated beam just before the positron production target at a peak current of 3.2 A.

However, it was still difficult to reduce the pulse width further to 4-ns, particularly because the positron beam with a 4 ns width was so weak that it was impossible to tune the AR beam transport system. Therefore, the following procedure has been carried out in order to accelerate the 4-ns beam. First, tuning of the whole accelerator, including the AR, was made with a 10-ns beam; then, the grid pulser was replaced with a 4-ns one. After a little fine tuning the 4-ns positron beam was accelerated and injected into the AR.

It was scheduled in June to perform an $e^+(4\text{ ns}) - e^-(2\text{ ns})$ collision experiment in the AR. The positron and the electron beams should be alternatively injected many times for this experiment. This means that the above-mentioned procedure was no longer applicable since tuning for the 4-ns positron beam should be performed within a very short time. To overcome this difficulty, both 4- and 10-ns pulsers were installed into the electron gun; also, a switching circuit was connected to them in order to

remotely switch over from one pulser to the other immediately. Figure 4.2 shows the beams thus produced; with this apparatus the collision experiment was successfully performed in the AR. Figure 4.2 also shows the difficulty in reducing the pulse width without a serious sacrifice of pulse amplitude.

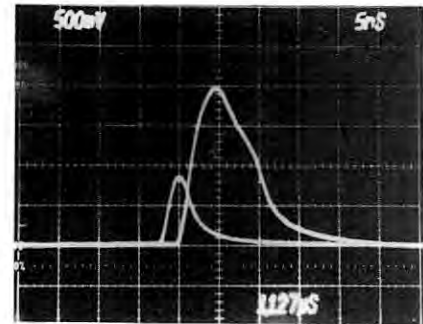


Fig. 4.2 Beam current waveforms injected from the gun with pulse widths of 4 ns (small one) and 10 ns (large one).

In June, a positron beam shorter than 2 ns was requested in order to obtain a single bunch beam in the AR. To produce a positron beam shorter than 2 ns, the SHB was operated; this compressed the beam pulse-width from 4 ns to shorter than 2 ns. Figure 4.3(a) shows the waveforms of the beam, where the lower one with a longer width is a case of the SHB-off and the upper one with a shorter width is an SHB-on case. The positron beams measured at the end of the positron generator are shown in Fig. 4.3(b). With this method single-bunched beams were successfully accumulated in the AR.

To advance accelerator characteristics further, some improvements were made. One was to raise the high voltage of the electron gun

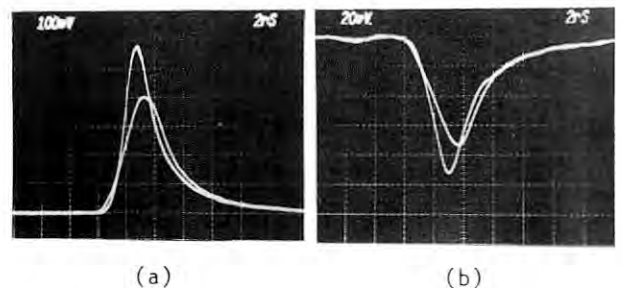


Fig. 4.3 Accelerated electron and positron beams with and without the SHB.
 (a): Electron beams just before the target. Higher one: with the SHB, peak current 2.4 A. Lower one: without the SHB.
 (b): Positron beams at the end of the positron generator. Higher one: with the SHB, peak current 6.8 mA. Lower one: without the SHB.

from 110 to 150 kV; another was the development of a new grid pulser to produce a higher voltage pulse. Using these devices a beam acceleration test was carried out in July after the scheduled operation period. The results of the test are summarized in Fig. 4.4. The new grid pulser made it possible to draw out a considerably higher current from the gun, whereas the rise of the gun voltage suppressed the beam space charge effect and enabled the higher current acceleration. As a result, the positron beam current reached more than 20 mA at the end of the positron generator.

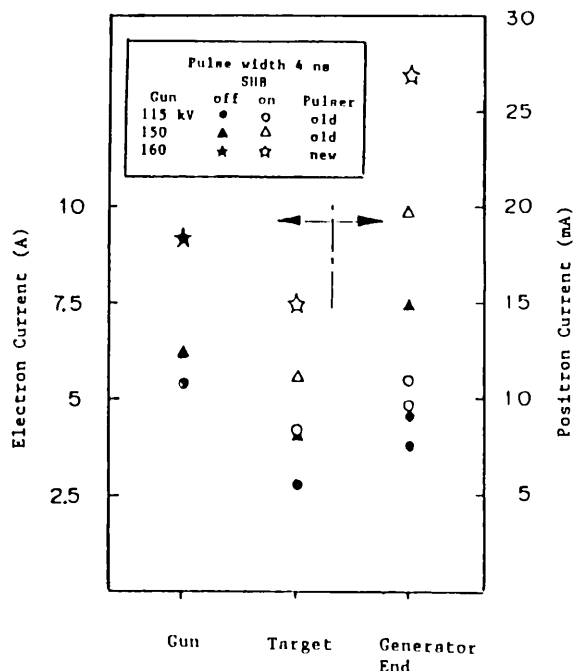


Fig. 4.4 Accelerated electron and positron beam currents along the positron generator, when the gun voltage was varied; the grid pulser was changed by a new or old type.

4.2 Injection system

Advances in the injection system

Since the conversion efficiency of an electron to a positron to be accelerated is very low (an order of 1/1000), it is very important to increase the electron beam current for a given beam energy. For this purpose two major improvements were made in the injection system. One of them was concerned with the electron gun system; the other was the installation of a subharmonic buncher (SHB) system.

As for the gun, improvements were made on its vacuum system, electrode structure and grid pulser. In addition, it was possible to operate the gun at higher voltages and to switch over immediately from one grid pulser to another. In the nanosecond region it becomes more difficult to obtain a shorter pulse without a decrease in the beam current. The SHB was introduced in

order to overcome this difficulty; it works in such a way that it reduces the pulse width by compressing the beam in its acceleration axis and increasing the peak current.

Improvements in the electron gun

Several improvements have been made in the gun system: a vacuum system, cathode-anode structures, a grid pulser, and operation conditions. As a result, the emission current was considerably increased. The current amounts to about 10 A with a pulse width of 4 ns and a cathode-anode voltage of 160 kV.

(1) Electron gun assembly

A thermionic gridded gun is installed in the gun assembly composed of a focus electrode, an anode, a ceramic insulator and a grid pulser (Fig. 4.5). The electrode structure was determined by an analysis of electron beam trajectories based on the computer code of W. B. Herrmannsfeldt.

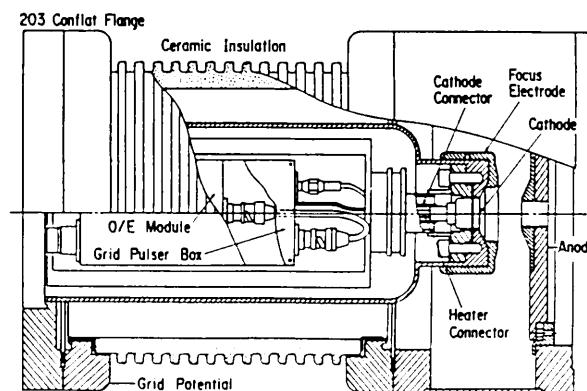


Fig. 4.5 Cutaway view of the electron gun assembly.

(2) Vacuum system and its operation

The characteristics of an oxide-coated cathode are strongly affected by residual gases in the environmental vacuum. The cathode should be kept in an ultra-high vacuum when the accelerator is operating. However, the vacuum of the accelerator guides following the gun system is appreciably worse than that required for the gun. It is, therefore, important for the gun to maintain a high vacuum by differential pumping between the gun and the accelerator guide. For this purpose two ion pumps of 10 l/s each have been added at the end of the gun (Fig. 4.6). It is especially important to keep a good vacuum during and after the conversion process; thus, much attention has been paid to vacuum operation. Prior to conversion, all vacuum elements (such as the ion gauge outgassing during the initial stage of operation) are switched on.

During the conversion, all pumps (including ion pumps) are operated. The vacuum pressure is lower than 10^{-9} Torr even when the beam is on.

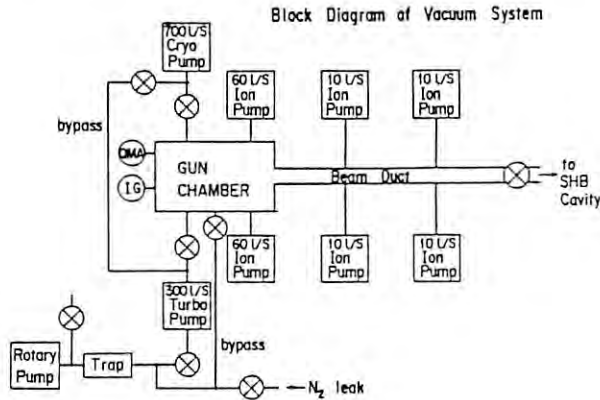


Fig. 4.6 Block diagram of the vacuum system. QMA: Quadrupole Mass Analyzer, IG: Ion Gauge.

(3) Cathode-anode structure

Since the electric field gradient on the cathode surface had been too low, the cathode-anode distance was reduced from 34.5 mm to 24.0 ± 0.5 mm in order to obtain a high perveance. The anode aperture was enlarged and anode nose was added in order to improve beam trajectories. Figure 4.7 shows an example of calculated beam trajectories that predicts a higher perveance of $0.26 \mu\text{A}/\text{V}^{3/2}$.

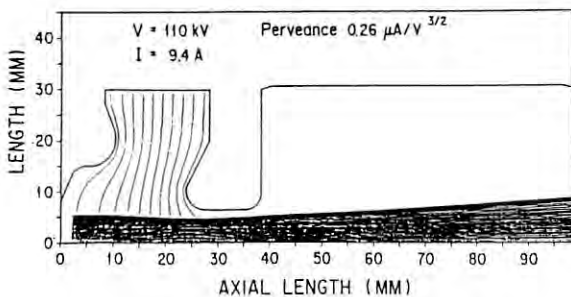


Fig. 4.7 Beam Trajectories from the gun cathode to the entrance of the first magnetic lens.

(4) Grid pulser

The grid pulser utilizing the avalanche effect of transistors has been improved mainly regarding the following two points.

One is the impedance matching between the pulser and the grid-cathode assembly as a load. Owing to the improvements in the gun system (mentioned above), the emission current could be increased; however, with this current increase the impedance of the assembly decreased. It was found that the emission current from the cathode

increased as the impedance of the grid pulser decreased (Fig. 4.8). This would be due to the improvement of the impedance matching between the two. The optimum impedance of the grid pulser can be determined for the emission current.

The other one is the use of new transistors that have a large slew rate. Figure 4.9 shows a circuit diagram of the pulser in which the output impedance is adjusted by the number of coaxial cables connected in parallel.

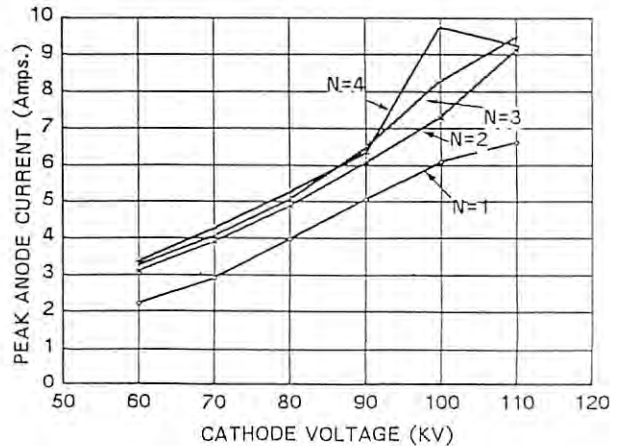


Fig. 4.8 Dependence of the peak anode current on the high voltage applied to the cathode and the grid pulser output impedance. N shows the number of parallel coaxial cables for the PFN.

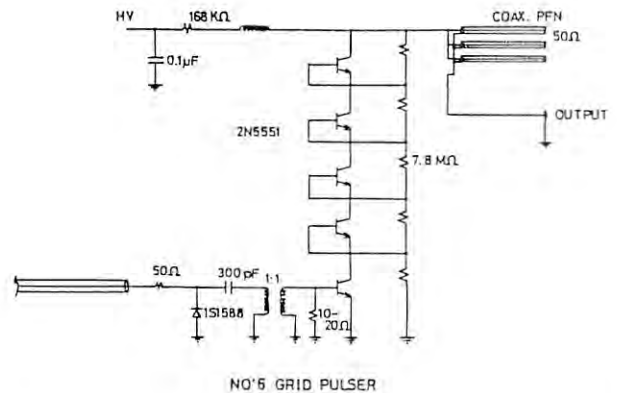


Fig. 4.9 Simplified circuit diagram of the short pulse grid pulser.

(5) Operation conditions of the gun system

Improvements for the operation of the gun system were made regarding three points: operational stability, a rise in the applied voltage between the cathode and the anode, and the introduction of a pulse-width selection system.

Operational stability: The operational stability has been considerably improved by selecting a grid-cathode assembly having a good performance

in the heater voltage vs. emission current characteristics (Fig. 4.10) and a nominal rating voltage (6.3 V) of the cathode in the space-charge limited region.

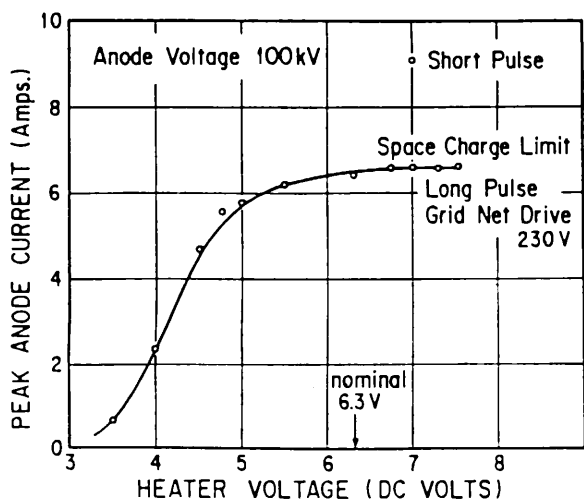


Fig. 4.10 Emission characteristics of the oxide-cathode gun as a function of the heater voltage.

Operational voltage up of the gun from 110 to 160 kV: A gun voltage of 160 kV was applied to the present gun with the aid of an SF₆-gas-filled capsule enclosing the ceramic insulator. As a result, the emission current increased and the beam characteristics were improved. A new ceramic insulator for higher voltages is now being prepared.

Introduction of a pulse-width selection system: A pulse-width selection system has been introduced to facilitate adjustments of the positron beam transportation which is very difficult for the short and low-intensity positron beam. In this system, a beam with a relatively long pulse-width (10 ns) is used for more easily sighting the position and profile of the positron beam; then, the pulse width is changed to a shorter-pulse beam (2 ns). These two pulses can be easily selected from the main/subcontrol room; the system works well. Figure 4.11 shows a block diagram of the selection system which comprises a control signal transmission line with optical isolation, two coaxial switches, a switch driver and two grid pulsers.

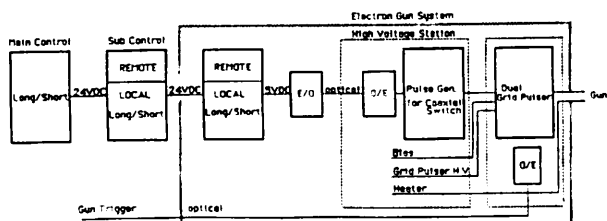


Fig. 4.11 Block diagram of the pulse selection system.

(6) Emission characteristics

Typical emission characteristics are shown in Figs. 4.10 and 4.12. From the short pulse (15 ns) data in Fig. 4.12, the perveance was found to be $0.26 \mu\text{A}/\text{V}^{3/2}$; this is in good agreement with the value predicted above. The impedance of the grid-cathode assembly is inferred to be about 17Ω at a cathode-anode voltage of -110 kV and about 12Ω at -160 kV . The highest emission current of 10 A with a pulse width of 4 ns has so far been obtained at a cathode-anode voltage of -160 kV .

The lifetime of the oxide-coated cathode emitting a high current is now under examination.

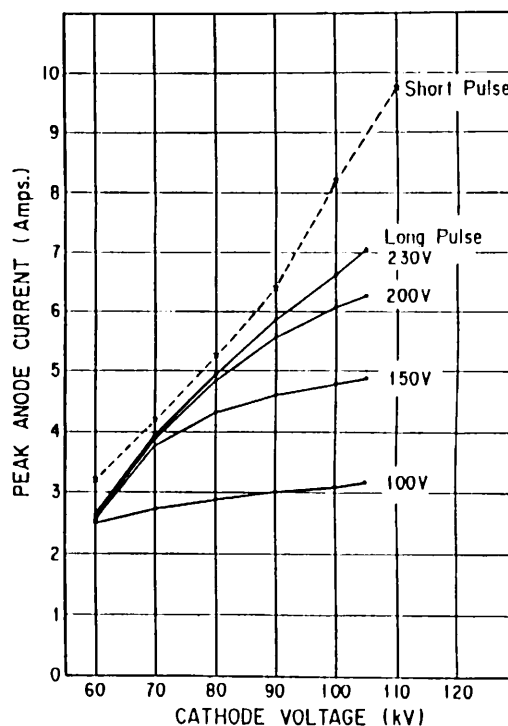


Fig. 4.12 Emission characteristics of the oxide cathode gun as a function of the cathode voltage. Voltages given in the graph show the grid drive voltage for a long pulse. The drive voltage for a short pulse is about 250 V. The heater voltage during these tests was 7.0 V.

Subharmonic buncher (SHB)

There are two major difficulties in positron beam acceleration. One is in obtaining a sufficient positron-beam intensity so as to be accumulated in the AR within a reasonably short time. The other is in making a pulsed beam shorter than 2ns (the period of the rf in the AR (508.6MHz)) in order to accumulate the beam in a single bucket.

Since positrons are secondary particles generated by bombarding a target with electrons, it is difficult to obtain an intense positron beam; the conversion efficiency from electrons to positrons is as small as about 0.3%. The primary electron beam intensity required is more than 10 A at an energy of 200 MeV. Although it is possible to extract a 2-ns beam directly from the electron gun, the obtainable current is only of the order of 10^{-1} A; on the other hand it becomes feasible for a 4-ns beam. Because of the characteristics of a grid pulser for the gun, a beam current from the gun increases as the pulse width is increased in a range of several nanoseconds. Therefore, a method of longitudinal compression for a longer pulse beam

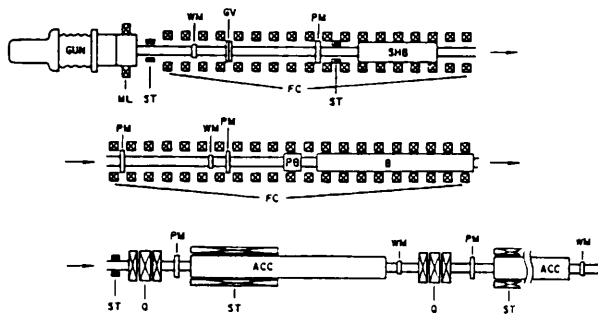


Fig. 4.13 Layout of the injector of the positron generator.
ML: Magnetic lens. WM: wall-current monitor. GV: Gate valve. PM: profile monitor. ST: Steering coil. FC: Focussing coil. SHB: Subharmonic buncher. PB: Prebuncher. B: Buncher.

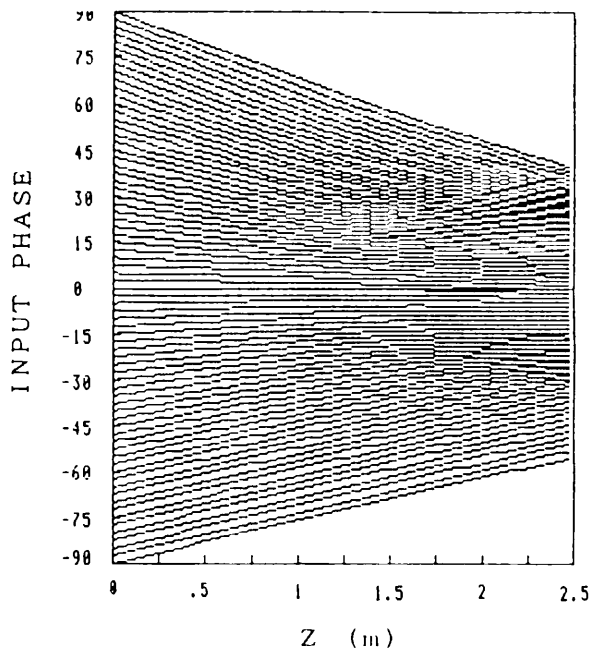


Fig. 4.14 Beam trajectories modulated by the SHB.

from the gun (the use of a subharmonic buncher) is more advantageous for obtaining a higher current. The SHB system is operated at a frequency of 119 MHz; this is the 24-th subharmonic frequency at 2856 MHz (the acceleration frequency of the positron generator and the PF 2.5-GeV linac). The layout of the injector is shown in Fig. 4.13.

The SHB compresses the width of a beam passing through the acceleration gap and the drift space from 4-ns to less than 2-ns (Fig 4.14). Calculations were made using a one-dimensional disk model which took into account space-charge forces. For simplifying calculations, a beam entering into the SHB was assumed to have a current pulse with a triangular waveform and a peak current of 10 A. The beam density changes in the drift space following the SHB (Fig. 4.15); after passing through the prebuncher it is separated into several bunches (Fig. 4.16). It is expected from the result that the peak current is increased by a factor

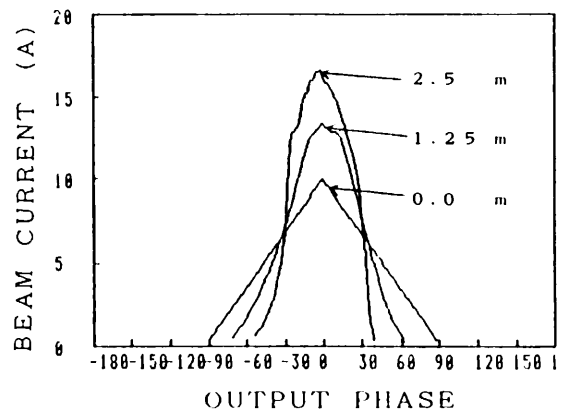


Fig. 4.15 Calculated bunched beam profiles for various drift space lengths following the SHB.

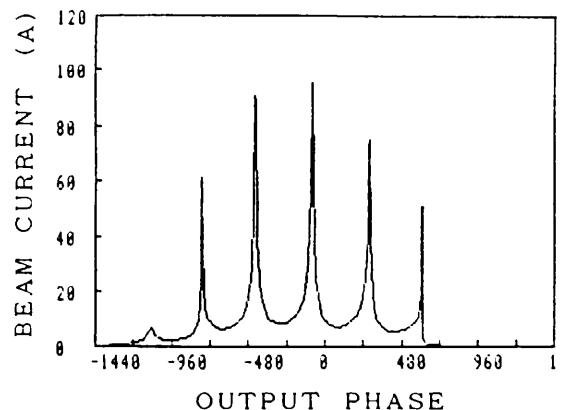


Fig. 4.16 An example of the calculated beam current structure within a pulse after passing through the prebuncher and its associated drift space.

of two owing to the compression. The number of bunches in the beam pulse (bunching in 2856 MHz) is less than six (Fig. 4.16). This indicates that the accelerated beam width is shorter than 2-ns (as desired).

The current variations of compressed beams were measured versus the rf power fed to the SHB cavity (Fig. 4.17). The peak current was increased up to a factor of about two with increasing SHB rf power.

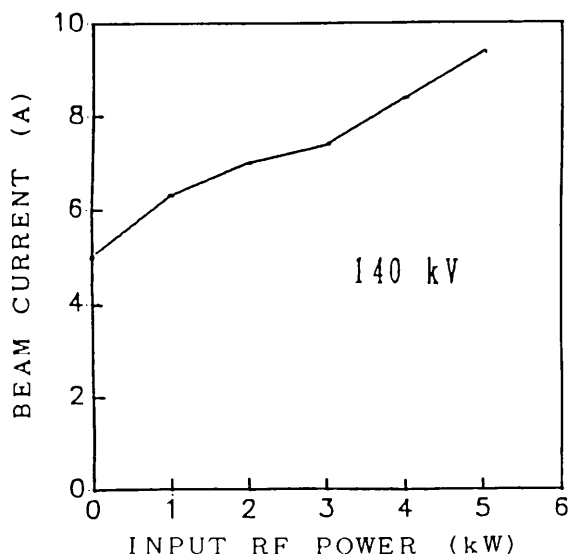


Fig. 4.17 Peak current variation of the beam compressed by the SHB versus the rf power fed to the SHB.

4.3 Control system

Double synchronized trigger generator

A new trigger synchronizer of the positron generator was developed for double synchronization with two independent radio-frequencies using a time-to-analog converter (TAC) and an analog-to-digital converter (ADC). All the triggers required for the positron acceleration and the AR positron injection should be synchronized with two different radio-frequencies: 0.8 MHz of the AR revolution frequency and 119 MHz of the subharmonic buncher (SHB) frequency of the linac. Synchronization with the AR revolution frequency is essential for single-bucket accumulation during a multiple injection. The SHB compresses the pulse width of a 4-5 ns long electron beam in order to obtain an intense beam shorter than 2ns (the period of the AR accelerating rf (508.6 MHz)). In the old system the triggers were only synchronized with the AR revolution frequency since the SHB had not been installed.

The new synchronizer provides four synchronized triggers at different timings: a beam trigger for a gun grid pulser, a monitor trigger 2.5 μ s earlier than the first, a klystron and kicker magnet trigger 100 μ s earlier and a septum magnet trigger 850 μ s earlier. The master trigger is synchronized with the output signal of a doubly-synchronized timing generator and outputted as the septum magnet trigger. The other three triggers are generated after delaying the septum magnet trigger by using the 0.8 MHz frequency as a clock (Fig. 4.18).

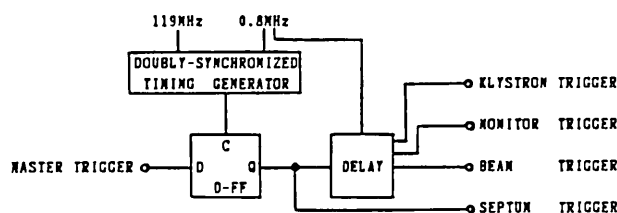


Fig. 4.18 New trigger synchronizer block diagram.

The doubly-synchronized timing generator is composed of a TAC, an ADC, digital comparators and a D-type flip-flop. A block diagram is shown in Fig. 4.19. Frequencies of 0.8 MHz and 119 MHz are divided by 8 and 2, respectively. Intervals between the rising edges of the two divided rf's are converted to digital values through a TAC and an ADC. Digital comparators select some interval values which pass through a preset window. Output signals from the comparators are synchronized with the subharmonic of 0.8 MHz; consequently, the doubly-synchronized timing signals are generated.

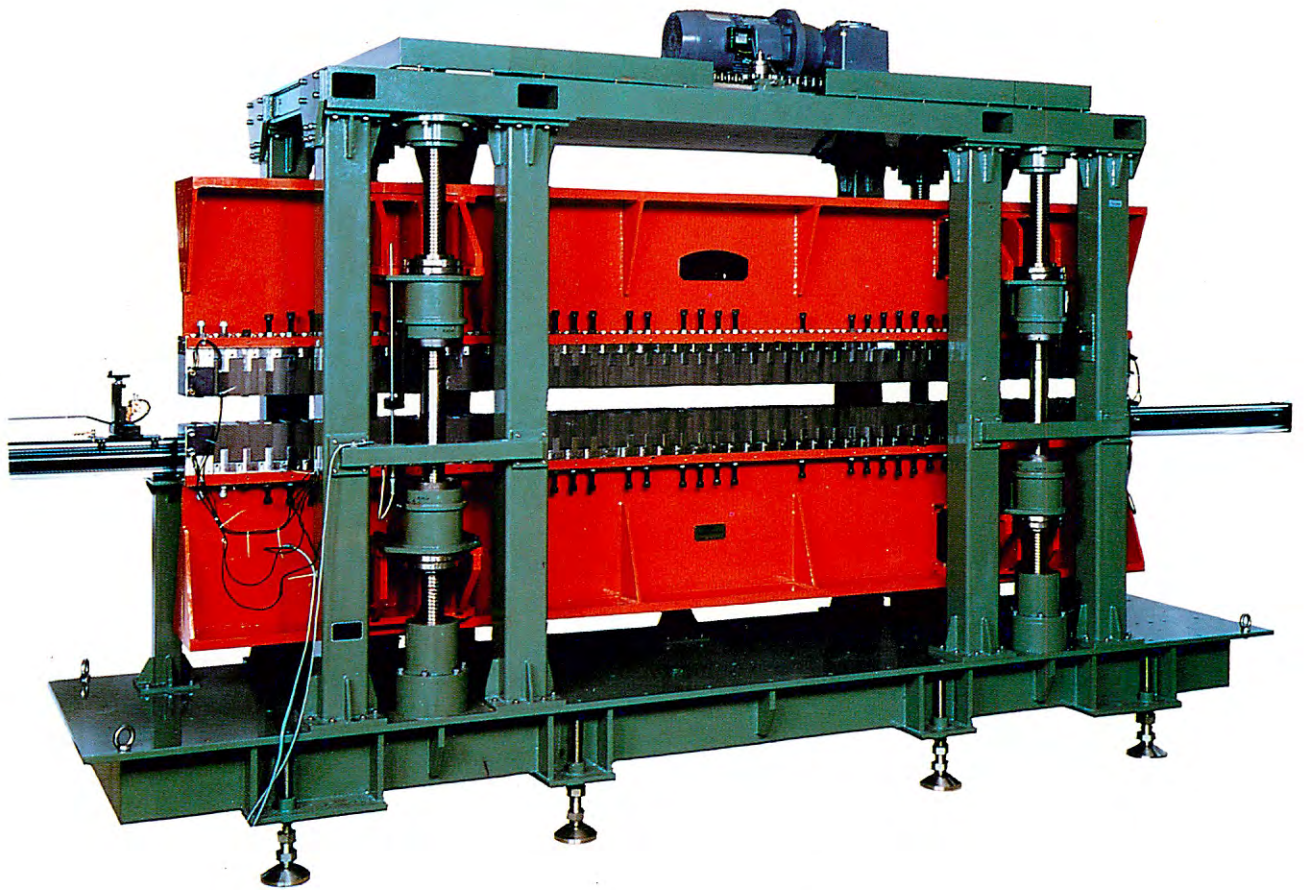
Careful consideration is needed in order to select the frequencies of the two rf's since the frequency combination changes the interval of the doubly-synchronized timing signals. If the frequency ratio between the two divided rf's is close to some integer, the interval becomes too long for operating the positron generator at a repetition frequency of 50 Hz.

During normal operation for AR injection the jitter between the electron beam signal and 0.8 MHz or 119 MHz was observed to be less than 300 ps, and is sufficiently small for single bucket accumulation during multiple injection using the SHB.



Fig. 4.19 Block diagram of the doubly-synchronized timing generator.

Light Source Department



B16 Multi—pole Wiggler (see p.78)

1. INTRODUCTION

The Light Source Department is equipped with a 2.5-GeV electron storage ring fully dedicated to research work with synchrotron radiation (SR). The storage ring was commissioned in March, 1982; and since then it has been well operated for over four years.

The storage ring (principal parameters listed in Table 1.1) has been and is growing in every sense. As can be seen in the figures given in p.15, the operational budget has been increasing; beam time has, thus, also been increasing. The number of beam channels is also growing with the cooperation of private companies and other institutes. There have been many improvements regarding the storage ring characteristics, prompted by machine studies.

As for beam instabilities, tune surveys of betatron oscillations have been performed over a wide area of the tune diagram. Two horizontal coupled bunch instabilities caused by higher-order mode resonances, 830 and 1070 MHz, could be completely cured by regulating the cooling-water temperature of each of four cavities and by exciting octupole magnets. A head-tail instability was cured by exciting septupole magnets. A two-beam instability caused by ion trapping was also cured by octupole magnets and by partial filling operation in which two-thirds of the RF buckets were filled and one-third were left empty. The ion trapping was directly observed using the bremsstrahlung generated by stored electrons hitting residual gases or trapped ions. Detail are described in Section 2.3. The longitudinal coupled bunch instability caused by a higher-order mode resonance, 758 MHz, has been partially cured by applying phase modulation to the RF power. However, under high stored current operation, the beam size grew slightly so that the beam lifetime decreased when the vertical wiggler was operated. In the end of the spring run, a "758" damper was inserted into one of the four cavities. As described in Section 2.3, the threshold current of the "758" instability was increased and the beam lifetime during wiggler operation became just the same as that without the wiggler. As a byproduct of this experiment, a new technique for venting the cavity was estab-

lished. The vacuum pressure decreased to the 10^{-9} torr range twelve hours after venting the cavity; twenty hours after that the beam lifetime reached 15 hours at a stored current of 200 mA.

A stable closed orbit is one of the most important properties for an electron storage ring dedicated to SR usage. There were many causes for the closed distortion reported in previous Activity Reports. In February, 1986, vibration of the SR axis between 0.7 and 100 Hz was measured under cooperation between the PF and SSRL of Stanford University. They found that the maximum amplitude was about 10 μm with frequency components of about 14.5 Hz. Also, the vertical vibrations of the ring tunnel floor were measured. It was found that the cause of the SR axis variation came from the vibrations of seven air-conditioners, a refrigerator and the evacuation system of the wiggler. Then, the signal of the SR axis vibration was fed back to the steering magnets. The final result shows that the vibration amplitude was suppressed to 0.02 μm . These experiments will be very useful when designing a new ring with small emittances. Details are described in Section 2.5.

Beam lifetime is closely related to the vacuum pressure of the storage ring. Before the second run of FY 1985, the initial stored current was limited to 150 mA because there was no cooling system for the vacuum chambers of the straight sections. During a summer shutdown in FY 1985, about 80 water-cooled absorbers were inserted at the upstream end of the straight sections. As a result, the initial stored current was gradually increased: the maximum achieved values were 360 mA without the wiggler and 250 mA with it, respectively (see Section 2.4.). These values are limited by RF power. Progress concerning the average stored current and the average injection interval during user time is illustrated in Fig. 1. Now the average stored current is 170 mA with an average injection interval of 12 hours. During the autumn run in FY 1985, it was shown that the vacuum pressures in the old chambers were better by fifty times than that in the newly fabricated chambers after 0.1 A-hours cleaning operation, even though the old chambers had been exposed to air for over one hundred days. This means that the old

Table 1.1. Principal parameters of the storage ring

Energy	2.5 GeV. Achieved; 1.6 GeV \sim 3.0 GeV. Above 2.5 GeV, accelerating storage.
Storage current	300 mA without wiggler. 200 mA with wiggler. Max. achieved 360 mA.
Bending magnet	Total 28. Radius of curvature 8.66 m.
Other magnets	Quadrupole 58. Sextupole 22. Octupole. Skew. Vertical steering.
Emittance	Horizontal 4.0×10^{-7} m \cdot rad.
Critical wavelength	Bending magnet 0.3 nm. Wiggler 0.06 nm.
RF frequency	500.105 MHz. Harmonic number 312.
RF acceleration system	2-klystrons (each 160 KW), 4 single cell cavities.
Radiation loss	400 keV/turn without wiggler. 450 keV/turn with wiggler.
Injection	2.5 GeV Linac. Rate 1 Hz. Time needed, a few minutes.
Vacuum pressure	5×10^{-11} torr without beam. 1×10^{-9} at the current of 300 mA.
Beam lifetime	15 hours at 300 mA, 25 hrs. at 150 mA.
SR channel	Total 16. Three under construction. One for beam diagnostics.
Insertion device	Superconducting vertical wiggler 5 T. Undulator, 60 periods, $K = 1.7$. Multipole wiggler, 26 periods, 1.52 T with 18.0 mm gap.

chambers remembered their histories; that is, the gas desorption from a storage ring vacuum wall resulted not only from the wall surface, but also from the inside of the wall. This suggested that newly fabricated vacuum-system parts must be treated with argon discharge cleaning and electron bombardment before being installed into the ring.

As will be described in Section 2.2, at the end of 1985, positrons were accumulated in the storage ring; the maximum current was 5.5 mA, accumulated in one hour with a 1-Hz injection rate. Now, the injector linac produces more intense positron beams; thus, the Light Source Department intends to change the electron storage into positron storage during FY 87, fabricating 50-Hz pulsers for two septum magnets and four kicker magnets. This will help eliminate ion trapping and/or particle trapping which causes a rapid deterioration of the beam lifetime (reported in previous Activity Reports).

The next steps that the Light Source Department is intending are: (1) *Low emittance*. During the next summer shutdown, four quadrupole magnets will be installed into the ring, four new power supplies of quadrupole magnets will be manufactured and the four old power supplies will be enforced. Then the horizontal emittance of the ring will be reduced to one-third of the present value. (2) *Multipole wiggler* (see Section 4.1). Magnetic field measurements are being undertaken for a multipole wiggler which is made of "NEOMAX", a new material for a permanent magnet. The number of poles will be 53, the field strength 1.52 T and a magnetic gap of 18.0 mm (to be installed during this autumn run). (3) *Feedback system for the closed orbit distortion*. This system (already mentioned) will be installed in each SR channels. Priority will be given to the SR channel where a precision experiment is in progress.

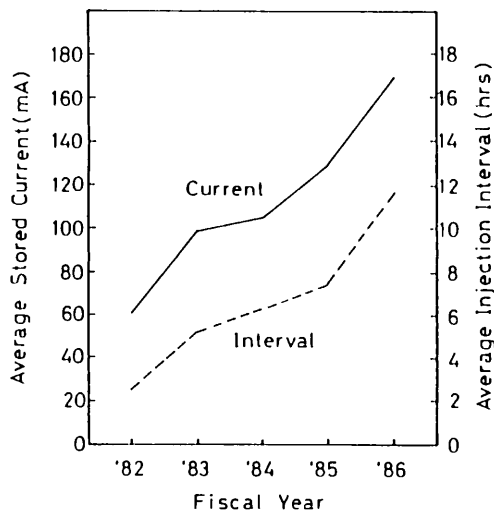


Fig. 1.1. Progresses concerning the year average of stored current and the injection interval during user time.

2. STORAGE RING

2.1 OPERATION

During FY 1985, the Storage Ring was operated for 2611 hours. The beam time was limited by the operational budget, especially by the electric-power budget. In FY 1986, it is expected that the beam time will be 2800 hours. Normally, the Storage Ring is operated from Wednesday morning through Saturday morning of the following week. Details of the beam time schedule are shown in Table 2.1.

Table 2.1 Beam time schedule

	Sun.	Mon.	Tues.	Wed.	Thur.	Fri.	Sat.
A	*	*	*	*	M1	U1	U1
1st week B	*	*	*	T	U1	U1	U2
C	*	*	*	M1	U1	U1	U2
2nd week A	U2	U2	M2	U1	U1	U1	M3
B	U2	M2	U1	U1	U1	M3	*
C	U2	M2	U1	U1	U1	M3	*

A: 1:00 a.m. - 9:00 a.m.

B: 9:00 a.m. - 5:00 p.m.

C: 5:00 p.m. - 1:00 a.m.

T: Tunings of machines, Linac, PF Storage Ring and Accumulation Ring.

U1: Users' beam time with superconducting wiggler.

U2: Without wiggler

M: Machine study

During 240 hours of continuous operation, 70 % of the beam time (168 hours) is allocated to users' experiments. However, for 48 hours of the users' beam time, the superconducting vertical wiggler is not operated since there is no supply of liquid helium from the Cryogenic Engineering Division of KEK. As for the machine study time, the Accumulation Ring of TRISTAN has a priority during M1; however the PF Storage Ring can use this beam time for studies if the PF Ring does not require many beam injections. During beam time M2, the PF Ring has priority use; the Linac has priority during M3. Usually, before M3 begins the PF Ring stores 300-mA electron beams and supplies SR to users. Even though there is no chance to reinject the beam, the PF Ring stores about 100 mA of the beam at the end of M3. We call this the user's bonus time.

The beam accumulation procedure into the Storage Ring is very smooth and quick because of the full energy injection from the Linac. Under the operation without the wiggler, it takes less than ten minutes from beam-channel closing to the channel opening, during which injection and safety confirmations are performed. On the contrary, during wiggler operation, it takes thirty minutes to open the beam channels again, because the wiggler is a superconducting vertical type having a narrow gap in the horizontal direction. In this case, the following procedures are required for reinjection: sweeping out the beam using a beam scraper, reducing the coil current to zero, moving up the wiggler to set the beam

position at the injection position where the horizontal aperture is wide enough for injection, cleaning out the vertical SR scraper to keep the wide aperture in the vertical direction for injection, storing beams into the storage ring, and exciting the wiggler. The percentage of time needed for injection in the total users time ranged between 5 % and 8 %.

The biggest machine failure was a vacuum leakage through a port of one of the four RF cavities (November 19, 1985). The cause was that a finger-shaped RF contactor (which was used for a blank flange of the cavity) was melted by the strong RF field. This problem was the same as that which occurred on November 20, 1984; 60 hours of user time was lost. These two experiences suggested that a new type RF contactor must be developed. Including this problem, the percentage of machine-failure time was 5.9 % over the last year.

2.2 STORAGE OF POSITRON BEAM

The 2.5-GeV positron beam was injected into the Photon Factory storage ring and stored on December 20, 1985. A maximum current of 5.5 mA and a beam lifetime of 120 hours was obtained. The positron beam was injected by passing it through the same orbit as the electron beam by changing the polarity of the magnet system, including the beam transport, two septum magnets, four kicker magnets and the ring magnet system. The current feed-throughs of the kicker magnets were exchanged for new ones in order to protect them against a high voltage of 40 kV. The insulation of the septum magnet to the earth was also reinforced. The positron beam of 2 mA in height, 10 nsec in width (FWHM) was injected into the Ring at a repetition rate of two Hz; the accumulation rate was 0.1 mA per minute. The yield of the bremsstrahlung generated in the bending magnet was reduced to about half compared with the case of electron accumulation. This suggested that there was no ion trapping which had been observed in the case of electron accumulation. This fact is very convenient for such insertion devices as the wiggler and the undulator which are located in the long straight sections¹⁾. The undulator radiation from the long straight section with a positron

beam was also measured. In order to improve the injection rate, the power supplies for the kicker and the septum magnet will be exchanged and a repetition rate of up to 50 Hz will be obtained.

reference

- 1) H. Maezawa, KEK Report 85-15 Feb. 1986 A/M.

2.3 BEAM STUDIES

2.3.1 Damping Coupler and Longitudinal Coupled-Bunch Instability

The longitudinal coupled-bunch instability, caused by the TM011-like mode, was suppressed by installing a higher-order mode-damping coupler in cavity #2 (the most detrimental to the present machine operation).

Two transverse instabilities, due to the TM111- and TM110-like modes, lead to a beam loss and should be avoided. These can be avoided by shifting the resonant frequencies and choosing a proper value of the betatron tune. A frequency shift is accomplished by controlling the cavity temperature using the temperature regulation system of the cooling water. However, when the cavity temperature changes, the frequency of the TM011-like mode also shifts. Unfortunately, the optimum temperature set for the longitudinal instability leads to the transverse instability. Therefore, the temperature setting of the cooling water must be chosen so as to avoid transverse instabilities and to achieve as high a threshold current of the longitudinal instability as possible. As a result, the maximum threshold current of the longitudinal instability is limited to value of 60 ~ 70 mA at the present operating point. Although this is not high, the PF ring is best operated at a high stored current of 300 mA since the longitudinal instability does not lead to an immediate beam loss, but only to a slight horizontal-blowup of the beam. However, when the superconducting vertical wiggler is in operation, the beam lifetime becomes short at a high stored current because of the narrow horizontal aperture in the wiggler. Therefore, we

Table 2.3.1 Measured resonant frequencies and loaded Q values.

These values were measured in air at room temperature by setting the tuning plunger at 2 cm inside the cavity wall. f_0 is measured without the damper. In this case, the side opening of the cavity is closed by a blank flange with a copper block which has the same structure and dimensions as that used in the upper opening. f_d is measured with the arrangement shown in Fig. 2.3.1. TM110 H(V) means the split mode of the TM110-like mode which deflects the beam horizontally (vertically).

Mode	resonant frequency (MHz)			loaded Q-value	
	f_0	f_d	$f_0 - f_d$	on damper	with damper
TM010	499.7299	499.6005	0.1294	12200	12130
TM011	758.267	756.482	1.785	7360	800
TM110 H	833.2709	832.5636	0.6773	42300	39700
TM110 V	825.177	832.192	-0.015	2800	2760
TM111 H	1070.812	1069.500	1.312	34400	800
TM111 V	1073.080	1072.892	0.188	8130	8130

decided to suppress the longitudinal instability by installing a damping coupler in cavity #2 (the most detrimental).

Before the construction of the damping coupler, characteristics of the cavity were measured using a model coupler in order to determine its effects on the fundamental and the higher order modes. Table 2.3.1 shows the resonant frequencies and the loaded Q-values of a cavity with damping coupler dimensions determined by tests with a model coupler.

The rod antenna couples strongly with the higher-order cavity modes if they have a high E-field parallel to the antenna at its position. As can be seen in Fig. 2.3.1, the cavity has two openings for damping couplers. When a damping coupler is installed in the side opening of the cavity, TM₀₁₁-like and TM₁₁₁-like modes were damped since they had such an E-field. Therefore a damping coupler was installed in the side opening of cavity #2 for the present study.

Data were taken at cavity dissipation powers of 22.3 and 29 kW/cavity with the same temperature (20°C) of the cooling water for all four cavities. The values of the cavity dissipation power correspond to the operating condition without and with the superconducting vertical wiggler, respectively.

Figure 2.3.2 shows the dependence of the threshold currents of the longitudinal instability on the RF accelerating frequency at a cavity power of 22.3 kW/cavity with the temperatures all at 20°C. Figure 2.3.3 also shows the threshold currents for optimum water temperatures.

A comparison of the thresholds in these figures (measured with and without the damping coupler) shows an obvious damping effect.

2.3.2 Extracted Power from the Damping Coupler

Power output for the single bunch operation

The RF fields induced by the beam in the

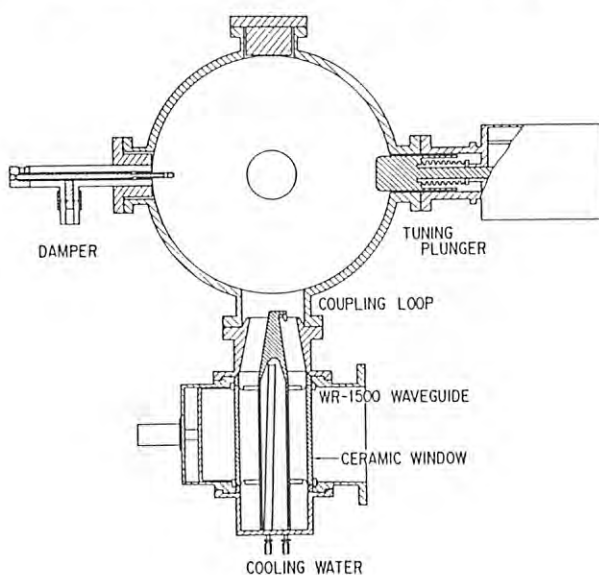


Fig. 2.3.1 Schematic view of a cavity with a damping coupler installed in the side opening. The circle in the center of the cavity is the beam duct hole.

cavity can be observed with the damping coupler. Figure 2.3.4 is a frequency spectrum for single-bunch operation at a beam current of 10.6 mA. It indicates that the extracted power contained mainly a frequency component of 756 MHz. The results of the low-power experiment carried out prior to this beam test showed that by installing a damping coupler the loaded Q-value of the TM₀₁₁-like mode was 700, damped by a factor of 11. The resonant frequency was 756 MHz (shifted

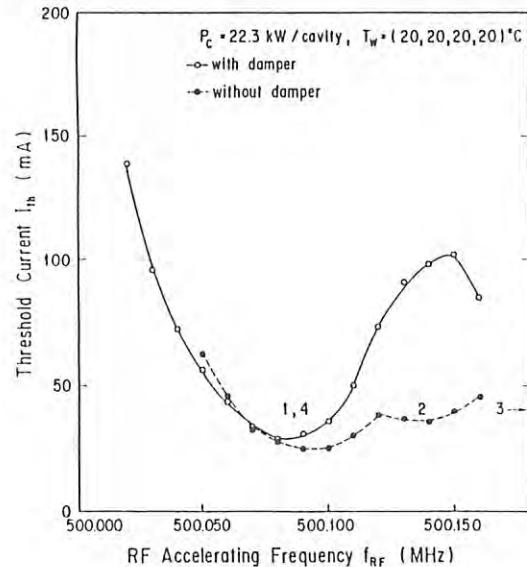


Fig. 2.3.2 Dependences of the threshold currents of the longitudinal coupled-bunch instability on the RF accelerating frequency (measured at a cavity dissipation power of 22.3 kW/cavity and the temperatures of 20, 20, 20 and 20)°C. The damping coupler was installed only in cavity #2 (the worst for the present operation).

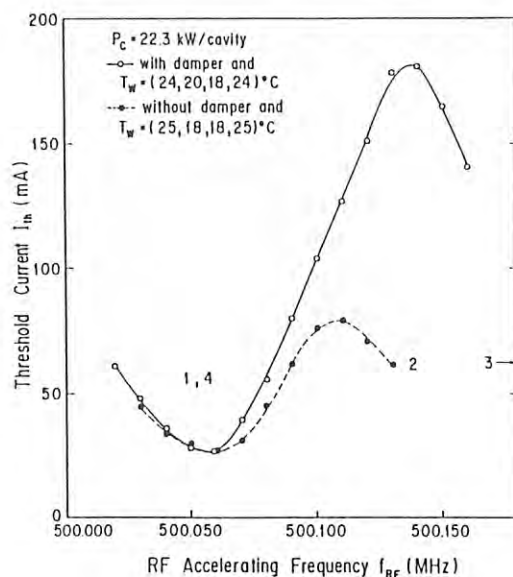


Fig. 2.3.3 The thresholds of the longitudinal coupled-bunch instability, measured at the cavity power of 22.3 kW/cavity for the best temperature sets.

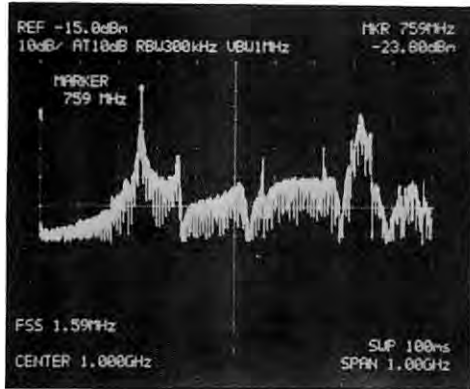


Fig. 2.3.4 Frequency spectrum of the beam through the damping coupler. The stored current was 10.6 mA for single-bunch operation. The cavity power was 22.3 kW/cavity and the temperatures of the cooling water were 20, 20, 20 and 20 °C. The center frequency is 1.0 GHz and the scan width is 0.1 GHz/division. The accelerating frequency was 500.106 MHz.

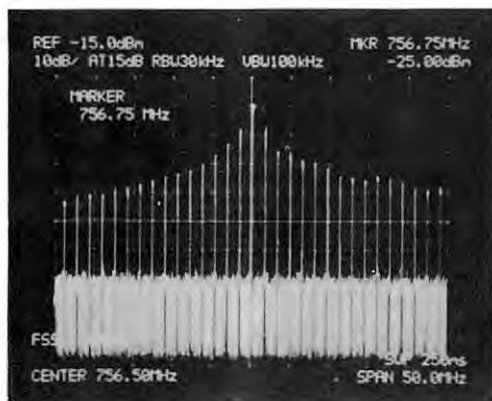


Fig. 2.3.5 Frequency spectrum of the beam signal through the damping coupler for the single bunch operation at 10.6 mA. $P_c = 22.3$ kW/cavity frequency is 756.75 MHz and scan width is 5 MHz/division.

lower by 1MHz from that of the cavity without the damping coupler). The frequency spectrum around 756 MHz is shown in Fig. 2.3.5; the peaks are harmonics of the revolution frequency. The center frequency of this display is about 756 MHz. Such spectral peaks increased in height with the stored current.

On the other hand, since the power level of the accelerating mode ($f_{RF} = 500.106$ MHz) in the cavity was controlled so as to remain constant at any stored current, the spectral peak height of the accelerating mode did not change with the beam current.

The total extracted power was measured with an RF power meter (HP 436A) through a pick-up port at a dummy load. Figure 2.3.6 shows the

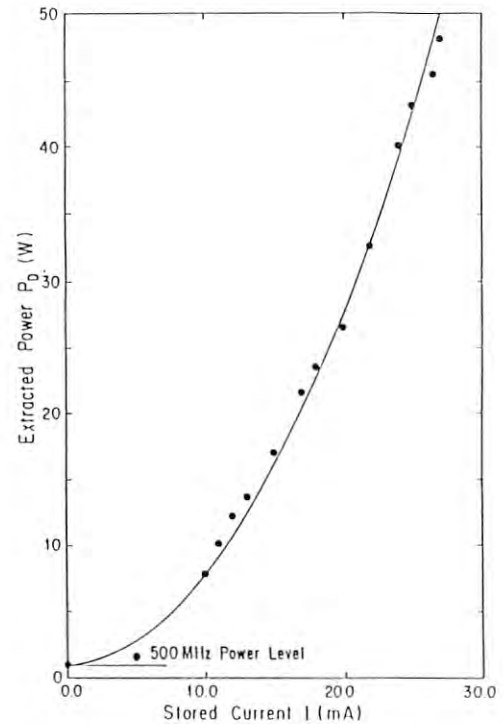


Fig. 2.3.6 The current dependence of RF power extracted from the damping coupler for single-bunch operation. The damping coupler was attached to cavity #2 down stream of the south cavities. The largest component was 756 MHz at the higher current. The power level of the fundamental mode was about 1 W at any current. $P_c = 22.3$ kW/cavity and $T_w = (20, 20, 20, 20)$ °C. $f_{RF} = 500.106$ MHz.

dependence of the extracted power on the beam current; for a correction we used measured coupling coefficients of the pick-up (i.e., -30 dB at 500MHz and -27 dB at 756 MHz, including cable losses). Effects from the other frequency components for the correction factors were ignored since they gave small contributions in this case.

These results (Fig. 2.3.6) agree fairly well (within 10 %) with the values expected from low-power measurements.

Power output for the multi-bunch operation (partial filling)

A typical spectrum from the damping coupler is shown in Fig. 2.3.7; here, one can see the peaks due to the longitudinal coupled-bunch instability between the peaks of the harmonics of the accelerating frequency. The stored current was 98.5 mA in the partial filling mode and the temperatures of the cavity cooling water were 20, 20, 20 and 20 °C. This beam current was above the threshold of the longitudinal instability and the highest peak in Fig. 2.3.7 is the one due to the longitudinal oscillation induced by the cavities without a damping coupler.

The power output from the damping coupler is shown in Fig. 2.3.8 as a function of the stored current, measured with the same method described

above. At high currents, the main component of the extracted power was 756 MHz; it was induced by the instability. Below the threshold the power of the accelerating mode and its harmonics were extracted. The former was constant with the stored current.

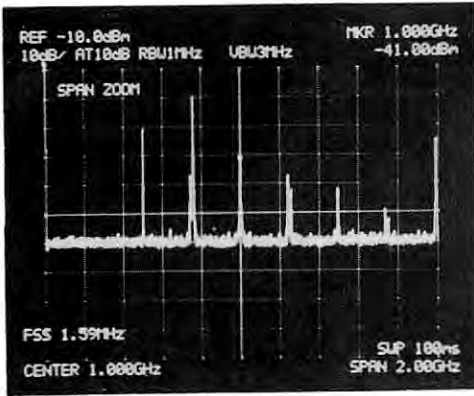


Fig. 2.3.7 Frequency spectrum of the beam signal through the damping coupler for multi-bunch operation. The cavity power was 22.3 kW/cavity and the temperatures of the water were 20, 20, 20 and 20 °C. The stored current was 98.5 mA, (above the threshold of the longitudinal coupled-bunch instability). The center frequency is 1.0 GHz and the scan width is 0.2 GHz/division. Accelerating frequency was 500.106 MHz.

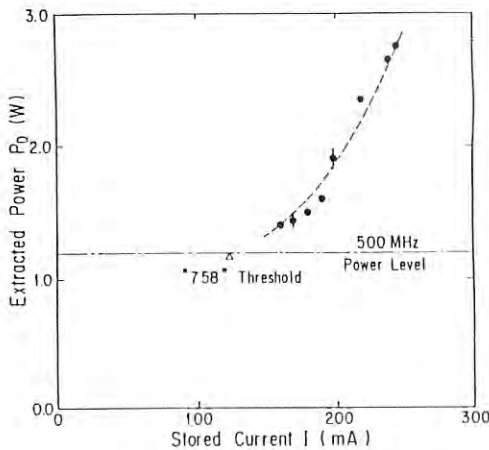


Fig. 2.3.8 The current dependence of RF power extracted from the damping coupler at cavity #2. The storage ring was operated in the partial filling. $P_c = 29.0$ kW/cavity and $T_w = (20, 20, 20, 20)^\circ\text{C}$. Below the threshold of the instability, the largest component was the fundamental mode with $f_{RF} = 500.106$ MHz. Above the threshold, 758-MHz components gradually increased with the current.

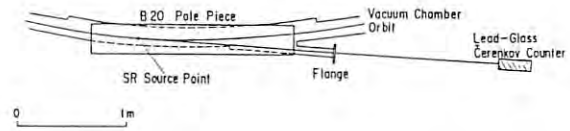


Fig. 2.3.9 Schematic drawing of the experimental system set at the bending magnet B20. Bremsstrahlung was detected by a lead glass gamma detector placed at 3,530 mm apart from the source point.

2.3.3 Ion-Trapping Studies with Bremsstrahlung

Ion-trapping often has detrimental effects on the stored beam in the electron storage ring. Studies of this phenomenon are progressing at the Photon Factory by detecting bremsstrahlung from electron-ion collisions. The experimental arrangement is shown in Fig. 2.3.9. The source point of bremsstrahlung was in the vacuum duct of bending magnet B20. High-energy bremsstrahlung hit a lead glass gamma detector ($100 \times 100 \times 300$ mm³) with a veto-counter in its front. The threshold level of the gamma detection was set at approximately 1.9 GeV.

Study of two-beam instability with bremsstrahlung

In the PF storage ring the most serious problem due to ion-trapping is vertical-beam blowup; this can be explained by an oscillation between the electron beam and trapped ions that occurs almost periodically. It was observed in the signal of the photo-diode array as a regular pulsation (see Activity Reports 1982/83 and 1983/84).

In the present experiment, bremsstrahlung was counted by a multi-channel analyser in the multi-channel scaler mode, with a trigger started by the timing of the vertical beam blowup. The trigger pulse was generated from the photo-diode signal (Fig. 2.3.10).

Figure 2.3.11 shows the bremsstrahlung yields thus obtained. The time variation of the yields was governed by two different time

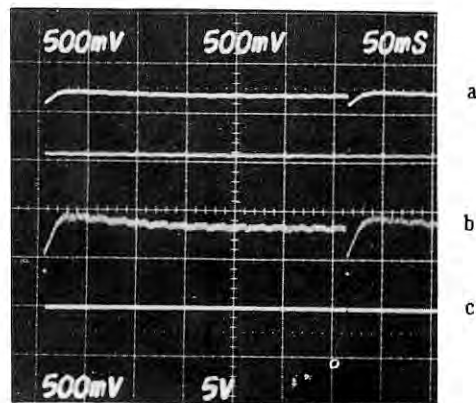


Fig. 2.3.10 Trigger pulse generated from the dip (timing of the blowup). a: Vertical profile monitor, b: Peak signal vertical profile monitor, c: Trigger pulse.

constants (Fig. 2.3.11): (a) Rapid decrease in the count rate at the beam-blowup timing and increase with a time constant of about 10 msec, which is approximately the radiation damping time. (b) Slow rise in 200 msec, until the start of the next blowup, which is interpreted as an accumulation process of ions.

Correlation between beam filling pattern and bremsstrahlung yield

A difference in the bremsstrahlung yields was found between partial and uniform bunch filling. Usually, the storage ring is operated in the partial mode, since it is experimentally known that the partial mode can greatly suppress the ion-trapping effects (see Activity Report 1982/83). Theoretically, it was pointed out that due to the existence of unstable regions of ion motion and the effect of multiple ionization, the number of trapped ions is small in the partial filling beam.

By comparing bremsstrahlung event rates of both modes under the same current and pressure conditions, it was found that the rates for the uniform filling were always higher than that for partial filling.

Bremsstrahlung yields measured with two different fillings are shown in Fig. 2.3.12 as a function of the stored current. Vacuum pressures measured near the source point during the present experiment were approximately the same for both fillings; thus, the difference in the bremsstrahlung yield with different bunch fillings, (Fig. 2.3.12) is a clear indication of trapping more ions during uniform filling.

A sudden decrease in the yield appeared during uniform filling at about 60 mA. The decrease was caused by vertical-beam pulsation (observed by a beam profile monitor). Because of the large mass difference, electrons move faster than ions when the beam is oscillating; the overlapping of the electron beam and the trapped-ion cloud becomes small. As a result, the bremsstrahlung yield decreased during beam pulsation.

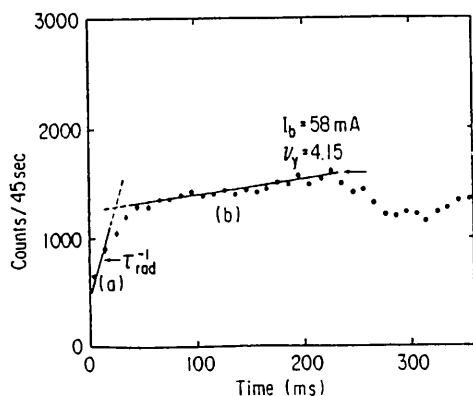


Fig. 2.3.11 Time variation of the bremsstrahlung yields. The starting time was synchronized to the periodical beam blowup caused by the oscillation of the electron beam and the trapped ions. Slow rise (b) is interpreted as an accumulation process of ions.

2.4 IMPROVEMENTS OF THE VACUUM SYSTEM AND THEIR RESULTS

2.4.1 Summary

During the summer shutdown in 1985 the vacuum system of the electron storage ring was modified for improvements. The main purposes of the improvements were the following three. The first was the protection of the stainless steel duct-components against heating as a result of a high flux of photons. The second was the replacement of the B-duct with a standard light exit port to a new B-duct with a 0-degree-type light port to extract light from an insertion device. The third was modifications of the ducts in short straight sections in order to fit new octupole and skewed quadrupole magnets. The improvements took three months. During this period all the ducts were removed from the magnets and left in the atmosphere. After the improvements each duct was baked for two days so that the pressure reached to the values of the final ones during the last run. The first beam was injected on October 31. No problem occurred during the first injection and during the following storage of beams. On beam, the pressure rose owing to photodesorption of molecules adsorbed on the ducts surfaces in the atmosphere. The pressure rises were small and about one thirtieth of those when the new surfaces of the old ducts were irradiated by photons. The small pressure rises demonstrate that the irradiation effect of photons does not influence the surface but dose affect the surface layer of the vacuum ducts. The maximum stored current reached 360 mA (limited by the klystron power). The improvements resulted in success.

During summer of 1986, the vacuum system of the new quadrupole magnet was installed for low emittance operation.

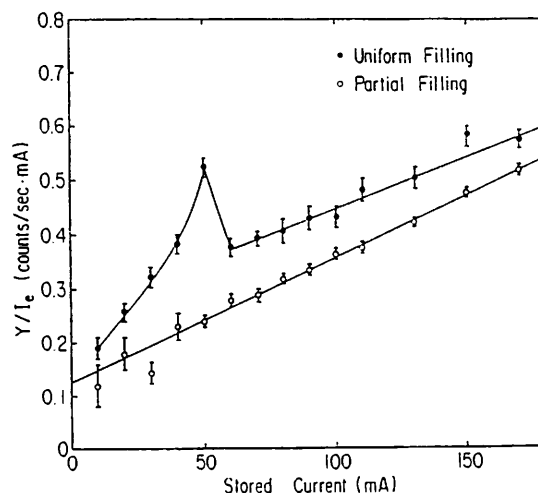


Fig. 2.3.12 Bremsstrahlung yields measured with uniform and partial fillings. Count rates divided by the currents are plotted. The yields for the uniform filling were higher than those for the partial filling at any stored current.

2.4.2 Design of absorbers

While designing the absorbers for synchrotron radiation, it was theoretically analyzed whether a newly installed absorber could affect the pressure distributions along the vacuum ducts or not. Because the pressures along the vacuum ducts depend on the irradiation intensity of photons, photons generate photoelectrons that can release many molecules from the duct surfaces by electron stimulated desorption. When the photon absorber was installed in the ducts, the irradiation distribution changed according to the shadow length of the absorber. On the surface of the absorber, the intensity is about two orders of magnitude higher than that on the duct surface at the absorber position. Theoretical calculations show that the change of the pressure is even less when the absorber is placed in the duct although the irradiation distribution changes; the total number of photons incident on the duct in the absorber section is kept the same value when the absorbers are installed. Figure 2.4.1 shows a typical example of the distributions of local pressures in the normal cell section. Figure 2.4.2 shows a cross-sectional view of the absorbers for the Q duct.

2.4.3 Pressure variation

The pressures of the electron storage ring depend on the outgassing rate by photons and the effective pumping speed of the system. The outgassing rate is a function of both the irradiation intensity and the desorption coefficient (called η (molecules/photon)). As the coefficient depends on the history of irradiation, the pressure variation is usually represented as pressure normalized by stored current (Pa/amp) against accumulated current (amp·h). The pressures of the PF ring have been measured by 50 ionization gauges and recorded by a micro-

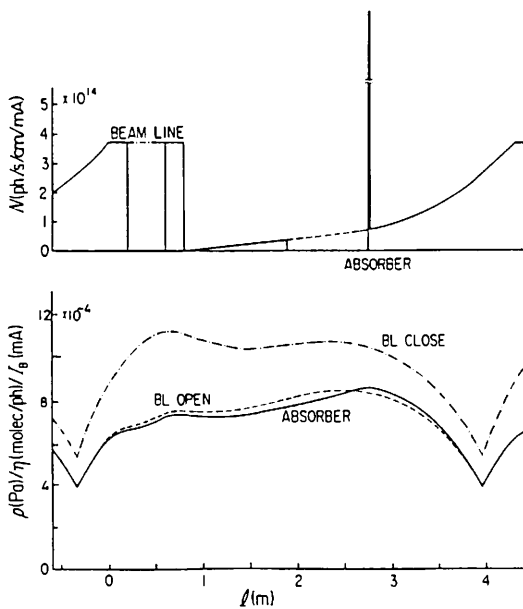


Fig. 2.4.1 Calculated local pressure along the vacuum duct in a normal cell of the Photon Factory.

computer. Figure 2.4.3 shows the average pressures of the improved ring and those of the old ring when the electron beam was stored. Although all the ducts of the ring were exposed to the atmosphere for three months during the summer shut down, the average pressures of the improved ring was less than the pressures of the old ring. When the accumulated current was over 50 amp·h, the difference in the average pressures became small. This difference of the average pressures is more clearly shown by comparing the pressures near the newly installed B-ducts (B-03, B-05 and B-17; filled circles) which have not been irradiated by photons with those near the old ducts (B-14 and B-23; squares). Figure 2.4.3 shows both results. The pressures near the old ducts were 1/30-1/40 of those of the new B-ducts. These results indicate that the irradiation effect is memorized not only on the surface but in the surface layers or in the bulk of the duct.

Analyses of this pressure variation will be submitted elsewhere; here, it is only briefly

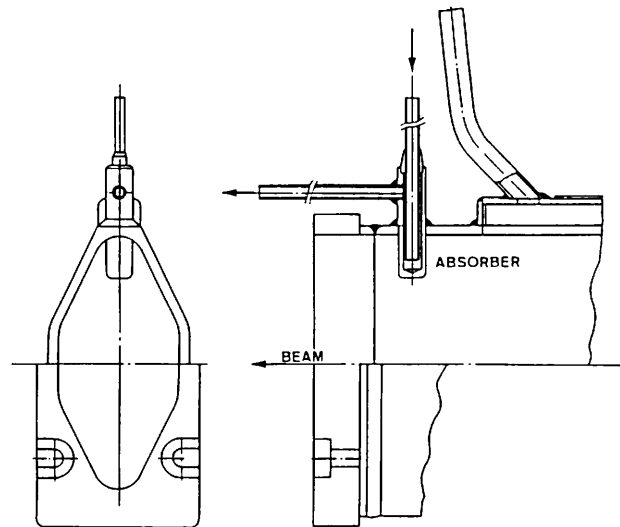


Fig. 2.4.2 Cross-sectional view of photon absorber (weld on the vacuum duct at the downstream of the quadrupole magnets).

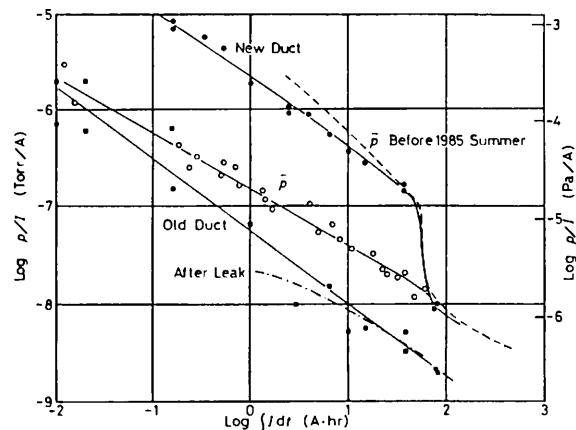


Fig. 2.4.3 Pressure variations against the beam dose.

described. Average pressures of the ring (dashed line) decreased gradually with an increase of accumulated current and then between 50 and 60 A·h the pressure decreased rapidly; over 70 A·h the pressures decreased gradually again. The rapid decrement of pressures was considered to be caused by an increment in the pumping speed of the system; titanium getter pumps were added to the system. The calculations for the ring pressures show that this rapid decrement could not be explained by these additional pumps. We have to present the new model in order to explain both the rapid decrement of pressures and the memory of the irradiation effect.

Usually, photodesorption is considered to occur on the surface on which photons irradiate the adsorbed molecules. The molecules are supplied from the space by an adsorption process. Analyses of photodesorption in the electron storage ring shows that the adsorbed molecules can quickly desorb by photon and photoelectron irradiation. Thus, the practical rate of photodesorption depends on the adsorption process of molecules. Here, a new model is proposed in which molecules are considered to be supplied not only from the space but from the bulk. In the usual case i.e., "not-hot vacuum" flow of atoms from the bulk to the surface is governed by thermal diffusion. On the duct wall of the electron storage ring a part of the photons incident on the surface can penetrate into the bulk; the penetration depth calculated for the Photon Factory is about 1 micron meter. In this photon penetrating layer, photons lose their energy and generate hot electrons. In the model, the diffusion process is assumed to be different in the layer from the usual diffusion process. The diffusion constant D_1 in the layer is larger than those D_2 in the bulk in which thermal diffusion occurs. Figure 2.4.4 shows the theoretical outgassing rate against the normalized time T . The outgas rate is multiplied by $\pi/2/C_0$, and the time is normalized as $\sqrt{D_1 \cdot t}/L_1$, where C_0 is the initial concentration, and L_1 is the depth of photon penetration. Parameters are $\sqrt{D_1/D_2} = k$. Below $T=1$ the outgassing rate depends on the

diffusion in the layer. Between 1 and 3 of T , the desorption rate abnormally decreased because the atoms absorbed in the layer quickly diffuse out and the layer became vacant. For $T>3$ the desorption process obeys the ordinary thermal diffusion process. The abnormal pressure decrement shown in Fig. 2.4.3 gives $D_1/D_2=1000$. Next, when the ducts were left exposed to the atmosphere for three months, gas molecules once became adsorbed again on the surface and could diffuse in this vacant layer though the usual thermal diffusion process. Calculation show that the concentration in the layer gradually in-

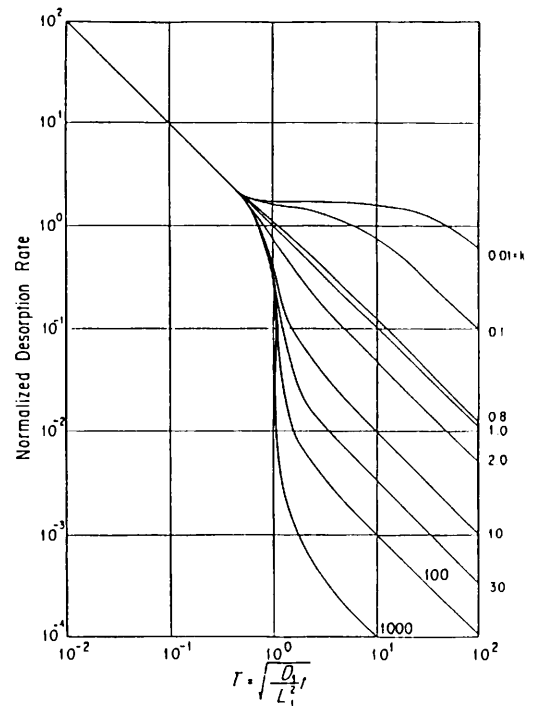


Fig. 2.4.4 Theoretical outgassing rate from the surface layer, in which there are two different diffusion constants.

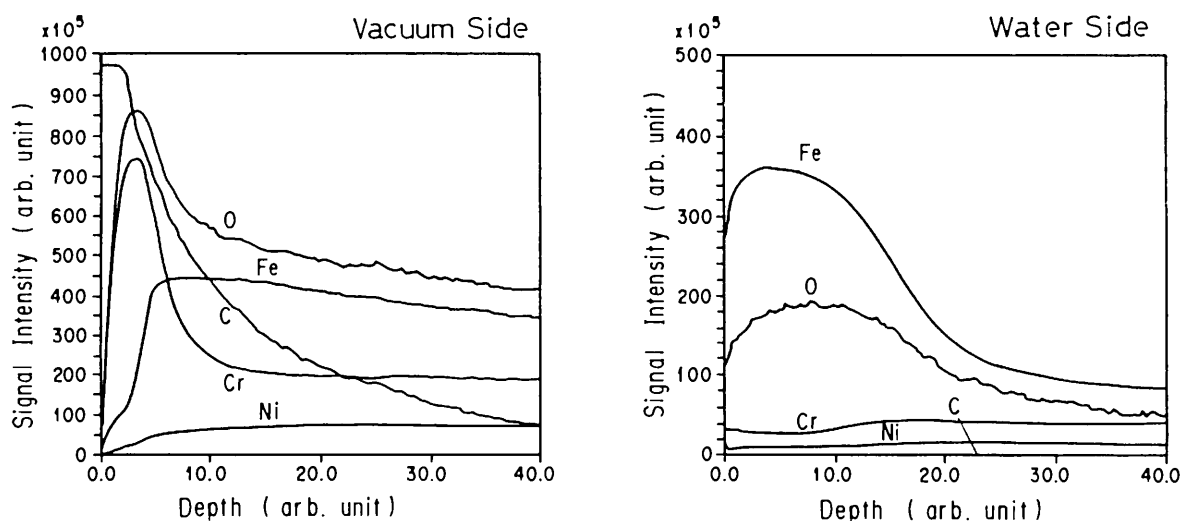


Fig. 2.4.5 Depth profiles of the chemical composition of stainless steel irradiated by synchrotron radiation from the 5-T vertical wiggler of the Photon Factory.

creases with time. The surfaces were covered by adsorbed molecules and the concentration of atoms slowly increased at the deeper layer near the boundary of photon penetration. The estimated concentration near the boundary is only 2% or less of those that for a new duct after three months of exposure to air. This low concentration indicates that the pressure at the old ducts were lower than those at the newly installed ducts (Fig. 2.4.3). This model is useful for the analysis of hydrogen diffusion under the irradiation of high energy photons.

2.4.4 Radiation effects of stainless steel

Down stream of the vertical wiggler, absorbers were inserted to protect the internal surfaces of the top and the bottom of the vacuum duct. Those surfaces were not cooled by water since the water channels would cut off the beam aperture of the duct in the bending magnet section. Absorbers were inserted in the duct in a quadrupole magnet section. They were U-shaped tubes made of stainless steel and cooled by water. After operations of the wiggler throughout this year, the absorbers were removed and their chemical composition were analyzed. The radiation effect could be clearly observed on the vacuum side of the tube at the position where photons directly irradiated. The effect was also observed on the cooling water side of the tube. Radiation could pass through the stainless-steel tube with a thickness of 2 mm. Figure 2.4.5 shows the results of chemical compositions analyzed by AES/SIMS against the depth which was designated by the etching time. The composition of stainless steel did not change in the other parts of the tube; thus, these results were not caused by a baking process but by penetrating photons.

2.4.5. Improvements of the cavity vacuum system

Extermination of abnormal pressure rise in the RF cavity section

Between 1984 and 1985, the storage ring operation sometimes suffered considerable disturbance from an abnormal rise in the vacuum pressure in the south RF cavity section. It occurred one or two hours after routine beam accumulation and made the average pressure of the storage ring worse, resulting in a poor lifetime. An outgassing from the graphite contactors used in the tuner was a cause of this phenomenon. During last summer, we found a proper bake-out method: the tuner inside was cautiously baked out and care was taken not to again absorb once released gases on the beam ducts.

It was also found that one of the tuners of the south cavities was set eccentrically (0.5 mm off-axis). Gap widths between the plunger and the tuner port were 2 mm at the wider side and 1 mm at the narrower side. This tuner pulled in the RF power of some frequency components. It caused outgassing by heating or discharging. This explains why it occurred only at the south section. A correction of the tuner axis was made immediately.

After the above improvements, we never again

observed such abnormal behavior of the cavity vacuum.

Reinforcement of the pumping system

Storage ring components, such as accelerating cavities, are sometimes exposed to the atmosphere (for instance, while changing of some cavity parts).

Insertion of the damping coupler into the cavity (described below) is such a case.

It would be remarkable if we could find a method by which we could quickly recover a vented system to the ultra-high vacuum (UHV) condition. For this purpose, a new pumping assembly was installed close to each cavity at both the south and north RF stations. The assembly consists of a large conductance chamber with a pumping unit having an old and a new sputter ion pumps with a nominal pumping speed of 400 l/s. Figure 2.4.6 is a schematic drawing of the new system; its effective pumping speed was expected to be 200 l/s at each cavity. At both the up and down stream sides of the cavity section, metal isolation valves with RF shields were installed.

Installation of damping coupler and vacuum recovery without bake-out

A damping coupler was installed in the down-stream cavity at the south RF* section. Isolation valves at both ends of this section were kept closed while venting. It was our first attempt to recover the vented RF section to UHV without a bake-out procedure by using the new venting system under similar pumping condition to that during the last summer.

After beam termination for venting, it took only 19hrs to once again achieve UHV; the ring stored 200 mA with a lifetime₉ of 700 min and the cavity pressure was 2.5×10^{-9} Torr.

The venting of the cavity section using a dry nitrogen supply system went very well (Fig. 2.4.7). It consists of a liquid-nitrogen reservoir, an evaporator, a liquid-nitrogen trap, and tubings with valves. The system can be evacuated with a turbomolecular pump. A liquid-nitrogen trap is necessary to adsorb impurities, especially water. A mesh filter is used in the trap to obtain high-efficiency adsorption. The system is made of stainless steel and bakeable valves. For carrying convenience, the system can be divided into three parts (Fig. 2.4.7). The

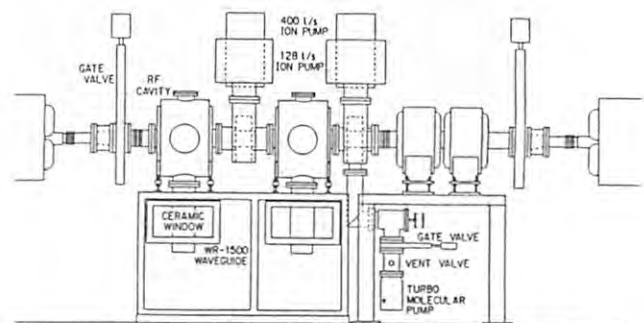


Fig. 2.4.6 New pumping system for the RF cavity section, having a large pumping speed.

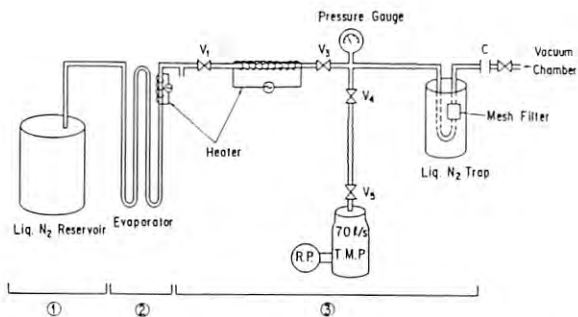


Fig. 2.4.7 Schematic view of the dry-nitrogen supply system. V1 ~ V5 are bakeable valves and C is the outlet for dry nitrogen (also shows the connection to the vacuum chamber).

inside of the tubes can be cleaned by flowing hot nitrogen gas. Hot nitrogen gas is easily obtained by heating tubes (Fig. 2.4.7).

Figure 2.4.8 shows vacuum recovery after the installation of the damping coupler. A vacuum pressure of 3.3×10^{-9} Torr was achieved only half a day after initiating evacuation. The RF accelerating cavities were conditioned with a high RF input power. The pressure rose to 7×10^{-9} Torr at an RF input power of 40 kW/cavity. However, no trip of the reflection interlock due to discharge was observed. The pressure fell to 1.2×10^{-9} Torr after a total conditioning period of three hours and did not rise at an operating RF power (without the vertical wiggler) of 22.3 kW/cavity.

The beam was stored, at first, up to 200 mA. The pressure increased from 1.2 to 2.9×10^{-9} Torr and gradually decreased. Two and half hours later, the stored current was increased to 300 mA. The pressure increased from 2.7 to 3.4×10^{-9} Torr and reached a maximum value of 4.2×10^{-9} Torr about two hours after the accumulation of 300 mA. The pressure then gradually decreased with the decrease of the beam. Since there were

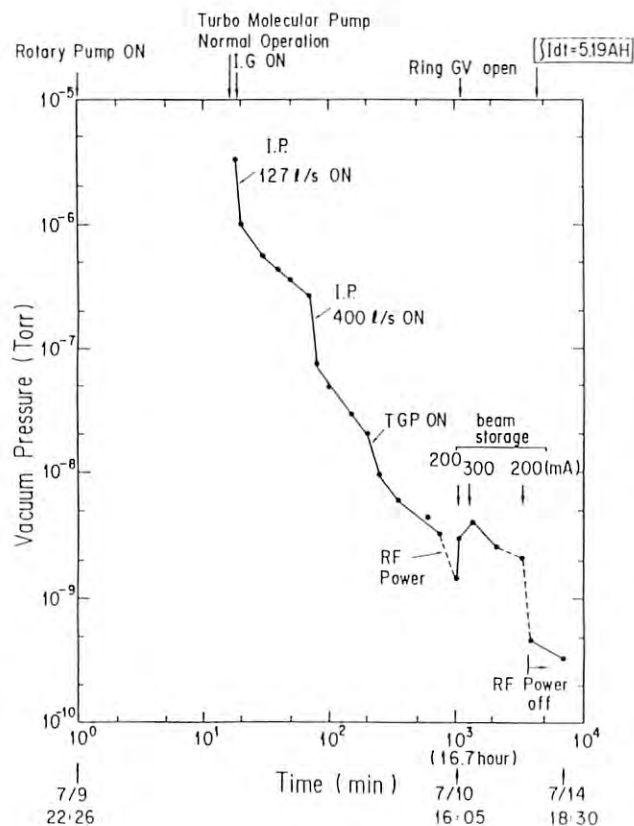


Fig. 2.4.8 Vacuum recovery without a bake-out. I.G. is the ionization gauge (B-A gauge), I.P. the ion pump, TGP the Titanium sublimation pump and Ring GV the isolation valve installed in the ring.

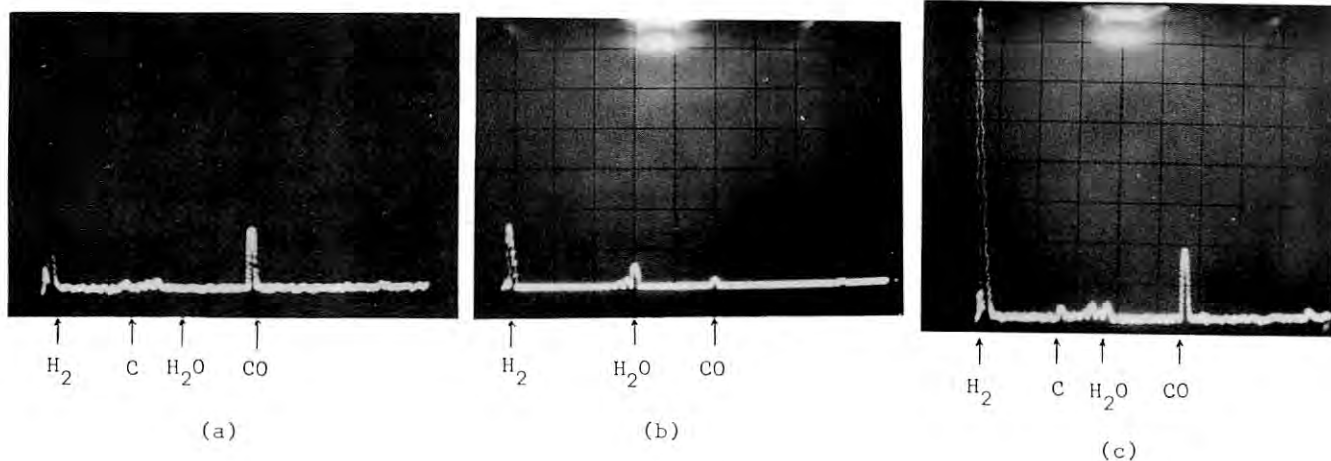


Fig. 2.4.9 Comparison of the mass spectrum of the residual gases before and after the venting. (a) A typical example before venting. (4.4×10^{-10} Torr) (b) After conditioning the cavities. (1.7×10^{-9} Torr). (c) After 5.2 ampere-hours of beam conditioning. (3.5×10^{-10} Torr). The sensitivity of (b) is lowered by a factor of 35. The sensitivities of (a) and (c) are almost the same.

no problems in the vacuum and the RF cavities, a machine study of the damping coupler was carried out. During this study, the accumulation of 200 mA was tried after the time integrated beam current of about 5 ampere-hours (the elapsed time of about 55 hours after the start of pumping). The pressure was 2.1×10^{-9} Torr at a current of 200 mA and 7×10^{-10} Torr without the beam. These values are only two times larger than those recorded before venting. The vacuum pressure without beam and RF power was 5.0×10^{-10} Torr. The pressure continued to decrease; two days after it reached 2.5×10^{-10} Torr.

The quick recovery of the UHV pressure was partly due to an increase in the pumping speed. As can be seen in Fig. 2.4.8, turning on the ion pumps (400 l/s) caused a lower pressure by a factor of 10. However, the rate of evacuation strongly depends on the components of the residual gases. Figure 2.4.9 shows the mass spectrum of the residual gases before and after venting. The peak of H_2O increased after venting (Fig. 2.4.9(b)) but the height was very small. After 5.2 ampere-hours of beam conditioning, the H_2O peak was decreased greatly (Fig. 2.4.9(c)). No other peaks, which contributed to the contamination of vacuum chamber, were observed. This fact shows that the dry nitrogen supply system worked very well.

The following records, taken from the logbook, are presented as a summary of this procedure:

July 9, 1986

- 21:00 All beam channels were closed and the beam was dumped. All isolation valves in the storage ring and beam channels were closed for protection against an accidental vacuum disaster.
- 21:10 Cavity power was turned off. All titanium sublimation pumps of the ring were turned on once.
- 21:16 Cavity cooling water was stopped. Started to establish a dry nitrogen supply system at the south cavity section.
- 21:45 Mass analyser, ion gauges and ion pumps for the south cavities were all turned off.
- 21:56 Started to slowly introduce dry nitrogen.
- 22:12 Cavity pressure (P_{ca}) became 1 atm. Opened the flange^{ca}, installed the damper and then shut it. Nitrogen flow was kept on during installation. No leakage of the isolation valves.
- 22:26 Rotary pump was turned on.
- 22:35 $P_{ca} = 0.1$ Torr (pirani gauge readings)
- 22:42 Turbo-molecular pump normal operation.
- 23:00 Turned on ion gauge: 2.3×10^{-6} Torr.
- 23:02 Ion pumps (128 l/s) turned on: 1×10^{-6} Torr.
- 23:58 Ion pump (400 l/s) turned on.

July 10

- 2:30 Titanium sublimation pumps turned on.
- 11:35 Started RF conditioning

- 16:05 Injected beam: $I = 200$ mA, $P_{ca} = 2.5 \times 10^{-9}$ Torr, $\tau \sim 700$ min.
- 19:00 $I = 300$ mA, $P_{ca} = 4.2 \times 10^{-9}$ Torr, $\tau \sim 800$ min

July 11

- 9:00 Beam studies for the damping coupler.

July 12

- 9:00 Studies with a single-bunch beam.
- 12:30 End of beam studies. Integrated stored current after the installation was 5.2 ampere-hours.

July 14

- 18:30 $P_{ca} = 2.5 \times 10^{-10}$ Torr with no RF power.

2.5 BEAM MONITORING

2.5.1 Introduction

The beam monitoring system for the storage ring has been properly working on the whole. Accordingly, our major effort has been made to solve some of the questions concerning beam position instability raised by synchrotron radiation users. Some users occasionally reported that they had been disturbed by short- and long-term shifts or drifts of the beam position.

The pre-existing beam position monitors were incapable of giving information on beam behavior, such as sudden changes in the beam position or long-term drifts. For instance, the information obtained by a position-sensitive quadrature photodiode was often on weak grounds. A copper mirror reflecting the synchrotron light to the photodiode was doomed to be fully responsible for producing an unreal beam movement because the mirror was found to be easily susceptible to thermal deformation or mechanical vibration.

To complement the present beam diagnostic system, it was proposed to monitor the beam position without using a mirror in the system. A plan to extend BL-21 beyond the shielding wall was thus put into practice.

After extending BL-21, two highly position-sensitive detectors, were installed: a photo-emission wire monitor and a split ionization chamber. These position detectors are one order of magnitude more sensitive than the pre-existing means (position monitors with pick-up electrodes and the optical beam monitors). They became not only very powerful for analyses of beam position noise, but also quite useful for eliminating some of the noise sources causing undesirable position movements which had been beyond the capability of the preexisting beam monitors.

To suppress beam position noise, a feedback system was thus devised by combining either one of the two new position monitors with the beam steering magnet system. A search for noise sources was also carried out by using a seismological method. Vibrational modes of the storage ring building were measured with a number of vibrometers evenly laid throughout the building. The major noise sources were then identified by analyzing the data with the Fast Fourier Transform method.

2.5.2 Extension of BL-21 to the Experimental Hall

BL-21, which had been used within the ring tunnel until last fall, was readily extended to the experimental hall in order to accommodate more flexible use of synchrotron radiation. Figure 2.5.1 shows a layout of the beam line (both inside and outside of the tunnel). The synchrotron light beam is split into three parts within the line. The central part of 7.35 mrad (line B) is first reflected down by the copper mirror as it was before. The rest of the beam forks out beyond the mirror to form two more beams (A and C). The vacuum duct laid inside the shielding wall contains a copper mirror, a beam mask, and a pair of beam shutters for the two lines. The vacuum duct beyond the wall is split into two branches: A for beam monitoring and C for desorp-

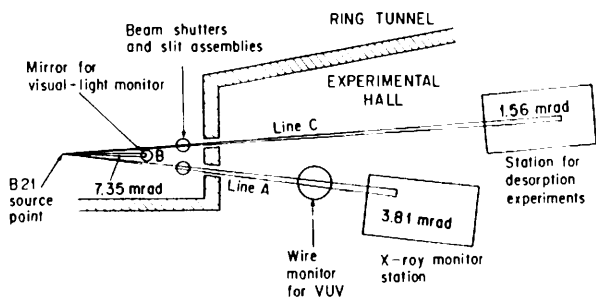


Fig. 2.5.1 Beam-line 21 extended beyond the shielding wall.

tion experiments. Here, we describe only line A (a description of line C will be given in the section on the vacuum system). Line A is closed at the downstream end with an Al window (2-mm thick) through which X-rays are extracted to the atmosphere. At 100 mm upstream of the Al window, a graphite plate was added to protect the window from heating due to radiation. The outer surface of the Al window is protected from oxidation, being covered with a container of He gas. The whole line inside and outside of the shielding wall was baked for vacuum pumping. It took about 10 hours to obtain a vacuum pressure of the order of 10^{-10} Torr by beam-cleaning with an average beam current of 100 mA.

2.5.3 Beam Monitoring at the Extended BL-21

The extension of BL-21 has made room for the installation of new types of beam monitors: a photoemission wire monitor, a fluorescent screen and a split ionization chamber (all placed in this order in line A).

Photoemission wire monitor (WM)

A two-wire position monitor was mounted in a vacuum chamber connected near the end of line A. The structure of the wire monitor is shown in Fig. 2.5.2a. Two tungsten wires of 100 μm in

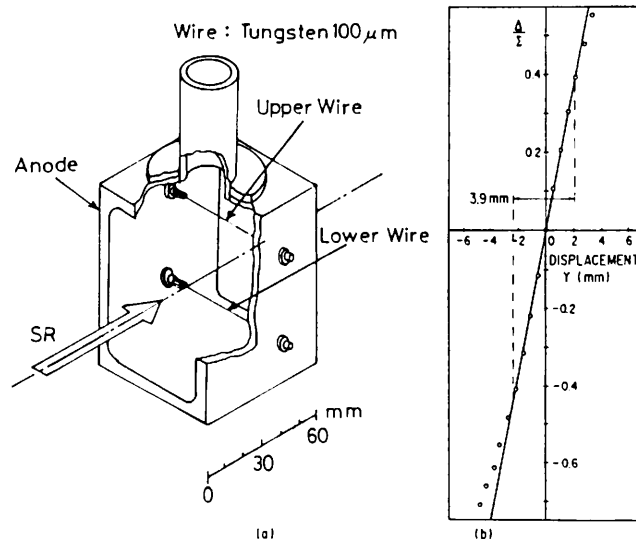


Fig. 2.5.2 (a) Structure and (b) position response of the photoemission wire monitor.

diameter are stretched horizontally and separated by 30 mm. The two (upper and lower) wires are supported on a wire frame which is made vertically moveable to be centered to the beam. The photocurrent from each wire is amplified with a current amplifier. Two current signals from the upper and lower wires are then fed to a difference amplifier in order to obtain a signal proportional to the beam displacement from the center. Figure 2.5.2b shows the position response of the monitor measured with the synchrotron radiation beam. The slope of the response curve gives a position coefficient of 0.20/mm.

Fluorescent screen with TV image processor

A fluorescent screen was placed at the point where X-rays are extracted from the end of line A through the Al window. The beam spot on the fluorescent screen can be observed by a TV camera. The TV image of the beam spot is digitized by using an image processor with 256×256 6-bit memories. Then, the spot center and width are computed to obtain the vertical beam position and size. This fluorescent screen and TV image processor system works with an over-all position accuracy of 0.1 mm.

Split ionization chamber (SIC)

An ionization chamber with its collector plate split into two triangles was placed next to the fluorescent screen monitor. The chamber receives a collimated X-ray beam coming out of the line. Figure 2.5.3 shows the structure of the SIC. The position signal is obtained by using the same kind of electronics (Fig. 2.5.4) as that used for the wire monitor described above. The ionization chamber has its a position coefficient of 0.10/mm.

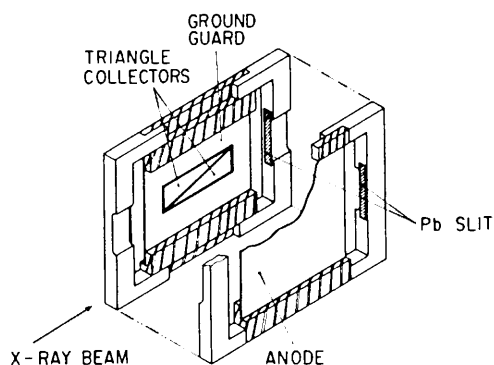


Fig. 2.5.3 Structure of the split ionization chamber.

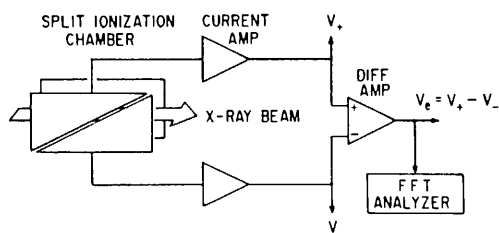


Fig. 2.5.4 Split ionization chamber and its electronics to produce a beam position signal.

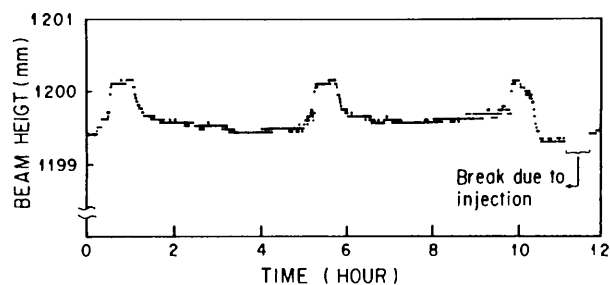


Fig. 2.5.5 Beam position hunching occurring every 5 hrs seen by using the fluorescent screen located and at 11 m from the source point and its TV image processor system.

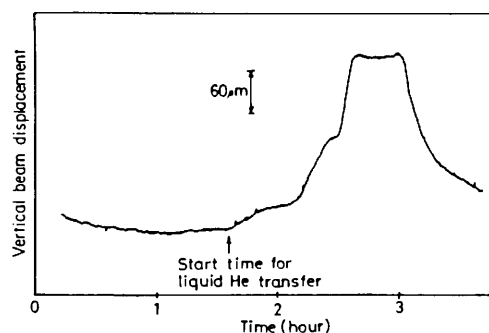


Fig. 2.5.6 The same beam position hunching as in Fig. 5 seen by the wire monitor located at 10 m from the source point.

2.5.4 Beam Position Noise and its Suppression by Beam Steering

Observation of beam position noises

The new position-sensitive detectors installed in the extended BL-21 turned out to be quite powerful in measuring beam position noise with many different characteristics, such as sudden shift, long-term drift and vibratory movement. These newly installed detectors have a good position accuracy (order of 1 micron) and a fast frequency response (about 1 kHz).

Upon the operation of these new position detectors very worthy evidence was found for noise sources which had been causing undesirable beam movements during runs.

The first evidence appeared in the following way. The fluorescent screen system started constantly monitoring the beam position with a higher position sensitivity (50 $\mu\text{m}/\text{digit}$) than that previously used at BL-15 (the observation of beam position could be made only intermittently because the beam shutter was closed at user's will). This system quickly gave us a clear view of a peculiar beam position hunching which lasted about 30 min. and repeated every 5 hours. Figure 2.5.5 shows this phenomenon taken with the fluorescent screen. Together with the fluorescent screen, the two-wire photoemission monitor reproduced the same shifting patterns with a much higher position sensitivity. Figure 2.5.6 is an example of the same beam position hunching taken with the wire monitor. The repeating pattern of the hunching was suspected to be quite similar to that of liquid-He transfer to the superconducting wiggler. It was soon con-

firmed that both patterns of beam position hunching and He transfer period matched each other when compared at corresponding times.

In this same search, some users reported that unusual pulsating noise patterns with a period of 2 min. were observed in their data. This phenomenon lasted about 8 hrs during the day time for two consecutive days. All of our detectors at BL-21 were hastily turned on to solve this problem. The pulsating noise was very clearly observed by both the ionization chamber and the photoemission wire monitor. It was soon proved that this pulsation was caused by the communication beeper system which happened to be receiving a checkup in a building several hundred meters away and was occurring only when the wiggler was in operation. Figure 2.5.7 shows the results of beeper noise detection made for both cases when the wiggler was turned off and when it was turned on. (Also, it should be noticed that the beam-position noise level is by 2- to 3-times greater with the wiggler on than that with it off).

Both of these phenomena, the position hunching every 5 hrs and the beeper-caused pulsation, were found to be induced from a single common cause. The feedback circuit for the wiggler current supply was very susceptible to such noise because its shunt resistor for current sensing was followed by a set of protection resistors and diodes connected to the coil in

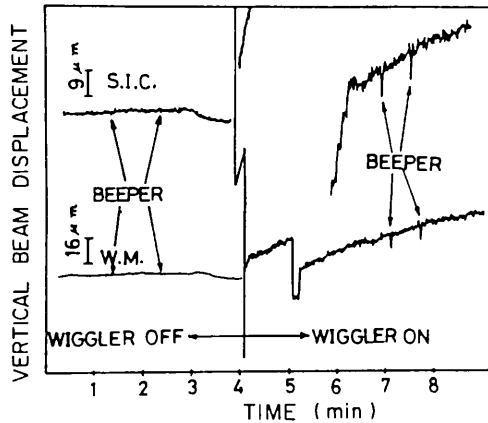


Fig. 2.5.7 Beeper noise appearing only when the superconducting wiggler was turned on.

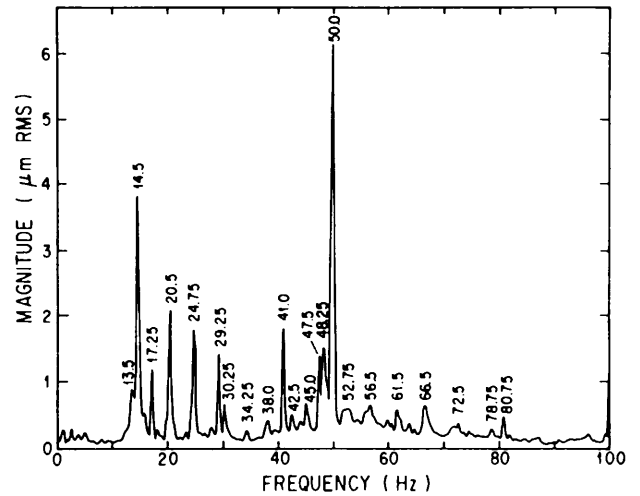


Fig. 2.5.9 Beam noise spectrum taken with the wire monitor.

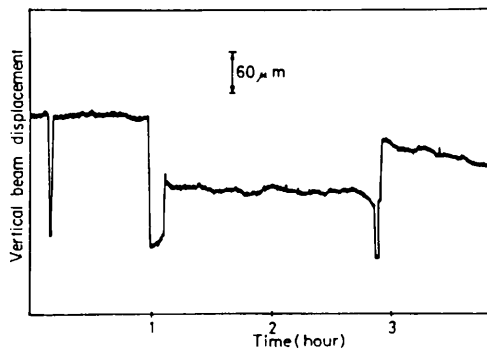


Fig. 2.5.8 Beam position jumping occurring irregularly in time, duration and amplitude, observed by using the SIC (The same pattern was seen by the WM as well).

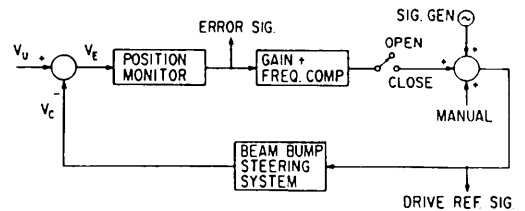


Fig. 2.5.10 Beam position feedback system comprising of a beam position monitor (SIC or WM), a servo controller (including a frequency compensator) and a bump steering system (magnets and power supplies).

parallel. By moving the shunt closer to the coil to measure only the coil current, these peculiar phenomena disappeared.

The second evidence worthy of mentioning is that the two highly position-sensitive monitors (SIC and WM) exquisitely unmasked a beam-position jumping phenomenon which had also avoided being detected during our search. Figure 2.5.8 shows a pattern of beam position jumping but occurring quite irregularly in time, duration and amplitude. This time, the undulator was the suspect; it had long survived from many earlier investigation. Nonetheless, the irregularity of the jump occurrence was the signature. Experimenters of the undulator changed the magnet gap at their will. Systematic experiments were made to correlate the amount of beam shift to the gap size. However, it is not yet well-understood how a horizontal field component is induced in varying the gap size.

Such types of beam position movements as described above were removed once each relevant causes was corrected. There, however, remain some other kinds of beam position noise.

Beam position noises were further precisely analyzed by observing noise spectra with an FFT analyzer. Figure 2.5.9 shows a beam noise spectrum taken with the wire monitor. The same spectrum is reproduced with the split ionization chamber. The spectrum ranges in frequencies from DC to a few 100 Hz including large peaks at 14.5 and 50 Hz.

Suppression of beam position noises

To suppress beam position noises, we introduced a beam steering servo system. The fundamental scheme was developed at SSRL. The servo system comprises three components: a beam position monitor, a steering magnet system and a servo controller which feeds back position signals to the electron beam. Figure 2.5.10 shows a feedback loop made up of the three components. The beam position signal is obtained with either the wire monitor or the split ionization chamber described in the previous section. To feed the signal back to the beam, the frequency responses of the steering magnet and its power supply were first measured for the frequency region of our concern. Figure 2.5.11

shows the frequency response of one of the ordinary steering magnets which had been in use for the correction of DC orbit bumps. This type of magnet is naturally made slow in frequency response with a large inductance of 2100-turn winding on an iron core. Also, the feedback was effective only up to a few Hz.

To make the response faster, we prepared two types of steering magnets with a small inductance. First, a 120-turn winding was added on top of the coil of the existing steering magnet. The frequency response of this 120-turn magnet is also shown in Fig. 2.5.11 for a comparison with the ordinary one. It performed well beyond several tens of Hz. Also, a fast magnet with a 150-turn winding wound on a ferrite core was fabricated to make its installation simpler as well as the frequency response faster. With all these improvements, the steering servo system was made to work smoothly over a few hundred Hz.

The beam position feedback system effectively suppressed position noise. Figure 2.5.12 shows an example of the beam noise spectrum taken with the feedback loop closed. The 14.5-Hz peak was reduced by a factor of 10 and the beam drift was made less than 0.1 μm .

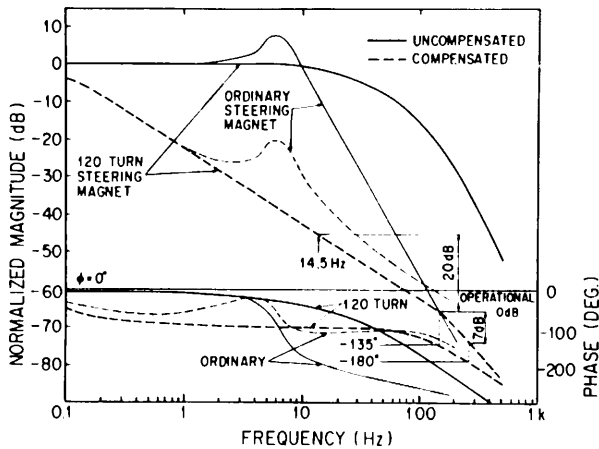


Fig. 2.5.11 Frequency responses of the magnet and power supply measured with electron beam steered at frequencies between 0 to 1 kHz. Data are plotted for both the ordinary steering magnet and the steering magnet with 120 turn winding. Compensation is added by the compensator included in the servo controller to give a noise reduction of about 20 dB at 14.5 Hz. The solid lines are for the responses measured before compensation was added and the broken lines for those measured after.

2.5.5 Search for Beam-Position Noise Sources

Seismometry of building vibrations

Many of the beam position noises were naturally coming through the storage ring building which encloses various vibrating machines and hardware. Vibrations of the building were measured by placing a number of vibrometers in both the tunnel and basement below. Figure 2.5.13 shows the locations of vibrometers used: 12 in total, 10 for vertical vibration only and 2 for the 3-dim directions. All possible sources of vibration are also indicated on the map as refrigerator, air conditioners etc.

Data of building vibration were taken under several different conditions, starting with all possible sources turned on, stepping down with one of them turned off at a time, and coming to a complete shutdown.

Data analysis and identification of noise sources

The data of building vibration collected above were treated with a Fourier analysis in order to determine spectral components. The frequency spectrum is quite similar to that which is taken with the SIC or the WM. Figure 2.5.14 gives an example of the vibrational noise spectrum taken at location 9 during full operation. Most of the spectral peaks were identified as coming from certain hardware shown on the map by correlating their occurrence to the conditions taken in the measurement. The direction of propagation of vibrational modes was also a signature to differentiate the vibrational source. Figure 2.5.15 shows how a vibrational mode dies down as it propagates.

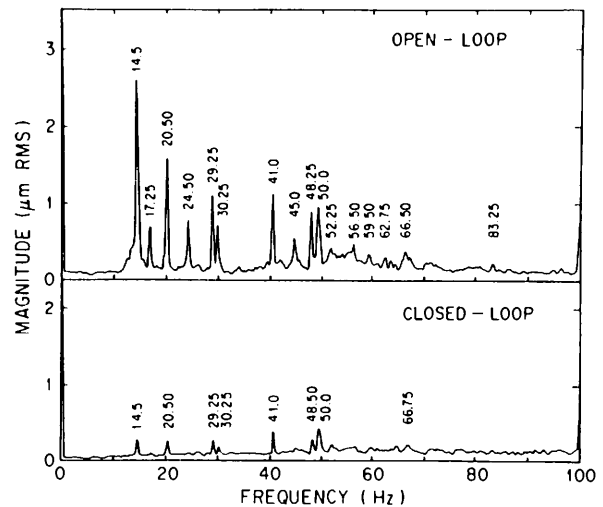


Fig. 2.5.12 Noise spectra taken before and after the feedback loop was closed.

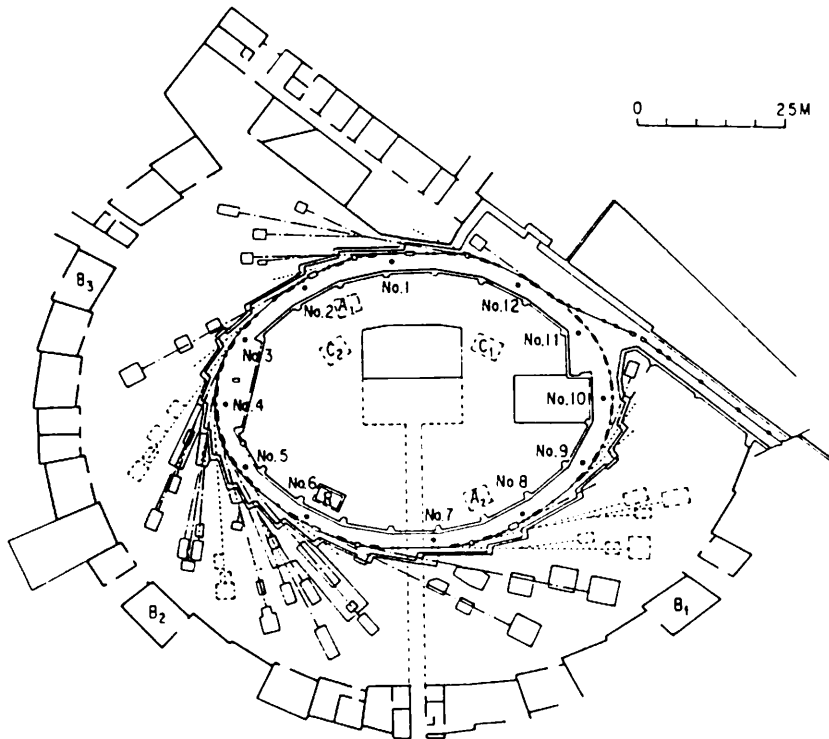


Fig. 2.5.13 Locations of vibrometers used in the search of the noise sources. The vibrometers are numbered 1 to 12. Air conditioners are labeled as A_1 and A_2 for those installed in the ring tunnel and C_1 and C_2 for those installed in the computer room on the second floor. B_1 , B_2 and B_3 are airconditioners located around the experimental hall. The refrigerator R used for the superconducting wiggler is located in the basement and is indicated R .

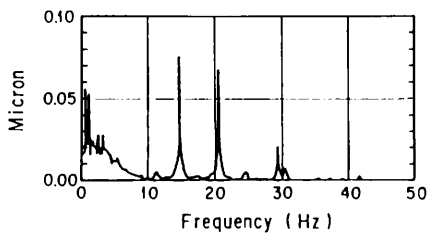


Fig. 2.5.14 Vibration noise spectrum taken at location 9 during full operation.

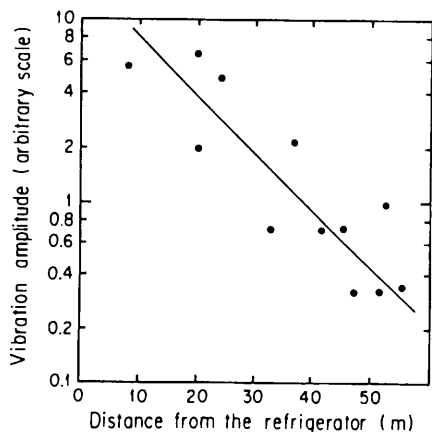


Fig. 2.5.15 Attenuation curve of the 24.7-Hz component in the storage ring building.

2.5.6 Summary

Participation of the new position-sensitive monitors, such as the split ion chamber and the photoemission wire monitor, produced several fruitful facts for understanding the causes of beam position movement. After removing some of these causes, the beam position became more stable to the extent that most of the users are satisfied with it. However, there still remain various kinds of beam position noise, shifting and drifting motion although they are small and are only detectable with highly position-sensitive measurements. These problems will become important issues as the machine enters the era in which low-emittance operation will be put into practice. Hence, it is planned to continue monitoring the beam position movement in order to resolve specific causes for different types of beam motion.

Noise-suppression experiments which have been carried out at the beam diagnostics line (BL21) will also be continued in order to apply the beam steering servo system to other beam lines for users.

1. T. Katsura, Y. Kamiya, K. Haga, T. Mitsuhashi and R.O.Hettel, KEK preprint 86-46 (1986)
2. K.Huke, to be published in Jpn. J. Appl. Phys. Vol. 26, No.2 (1987)

2.6 CONTROL

The control system of the PF storage ring uses four "super"-minicomputers (FACOM S-3500 and S-3300's) as device controllers and a general-purpose computer (FACOM M-360MP) as the library computer. These computers are connected to each other by a token ring-type network. Furthermore, many microcomputers are incorporated as local intelligences.

An operator console is to be rebuilt. Such components of the new console system as displays, touch screens and so on, have been installed and tested. Operation information services were refined after replacement of the control computer (Apr. 1985).

A proto-type database system for operation logging has been completed and is running for test.

2.6.1 Operator Console

Basically, the console comprises several equivalent units which can control any component of the storage ring. Besides these fundamental units, there are several displays assigned to fixed information services (Fig. 2.6.2).

A console unit comprises two 20" color CRT's and a touch screen. One CRT, which is driven by CAMAC display driver (KINETIC 3232) directly connected to the control computer, is used mainly for character-based representation. The other for graphic display is controlled by a microcomputer (FACOM 9450-II) which communicates with the control computer through GPIB. The touch screen system is made of a 14" color CRT with an optical touch sensing frame (Carroll

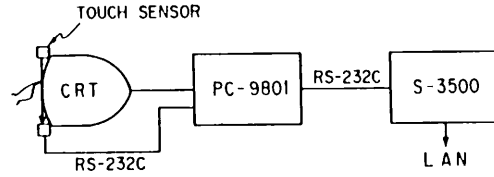


Fig. 2.6.1 Touch screen system

Touch) in front of it. Its sensing resolution is 2.92 mm x 3.12 mm. To reduce the load of the control computer, the touch system is locally controlled by a microcomputer (NEC PC-9801-VM4) which generates display pictures and processes touch signals (Fig. 2.6.1). It exchanges data with the control computer through a RS-232C link.

2.6.2 Operation Information Services

The control program for operation and the interlock system has been rewritten from PF-BASIC to FORTRAN77 owing to the replacement of the control computer. The program is refurbished for its algorithm and man-machine interface as follows:

- 1) The lifetime calculation method was modified from the fixed 5-point (about 4 sec interval) fitting of decay slant to the variable point (maximum 100 point, each interval of about 3 sec) least-squares fitting. The number of fitting points is increased by one with every sampling up to the maximum number 100, and is reset to two when the program detects a rapid change of lifetime. This method has a good signal/noise ratio in case

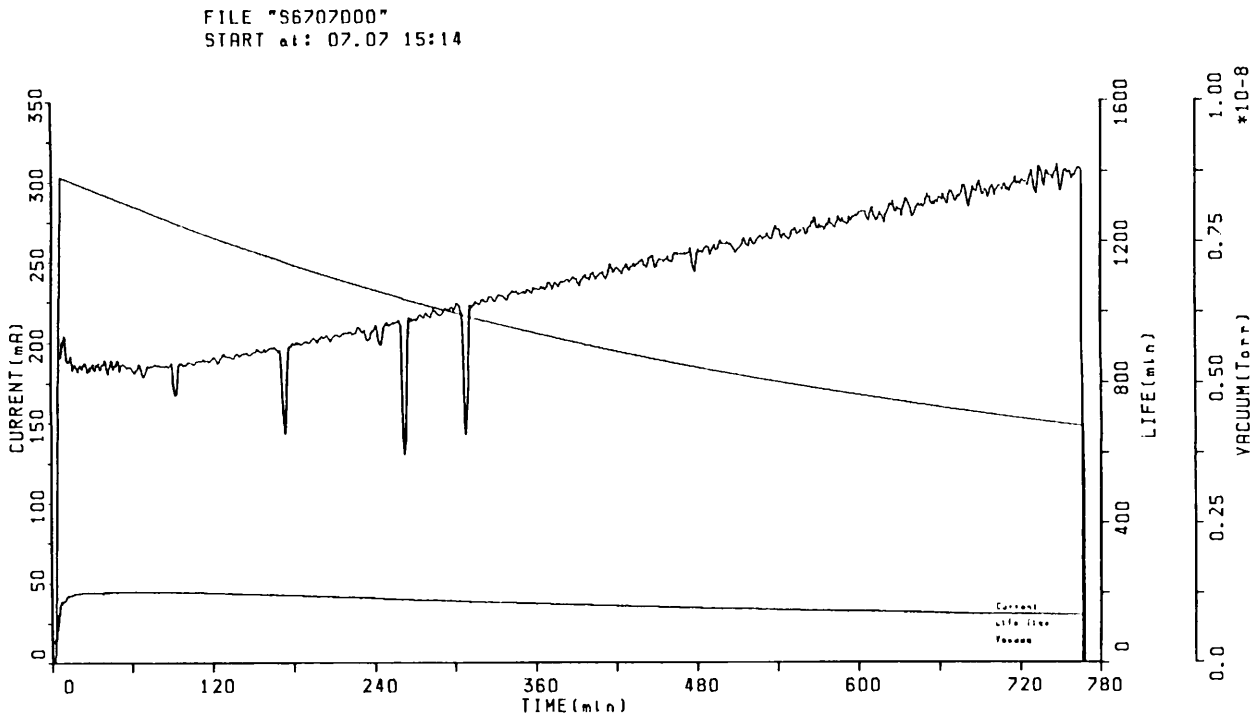


Fig. 2.6.2 Run summary plot

SR#	0	START	86/07/07 15:14:42	STOP	86/07/08 04:02:13
RUN	S6707D00	START I	0.0 (mA)	STOP I	0.0 (mA)
NORMAL RUN	ELAPSED	767.4 (min)	TOTAL I*T	2649.8 (mA.H)	
INJECTION	15:14:42 TO 15:21:32	ELAPSED	6.8 (min)	CURRENT MAX.	302.9 (mA)
		EXECUTE	5.9 (min)	CURRENT CHANGE	302.8 TO 302.7 (mA)
		VACUUM CHANGE	0.34E-09 TO 0.10E-08 (Torr)		
STORAGE	15:21:33 TO 04:02:12	ELAPSED	760.7 (min)	I*T	2639.2 (mA.H)
		AVERAGE	208.2 (mA)	MAX. LIFETIME	1418.7 (min)
		AT	03:42:45	CURRENT CHANGE	302.7 TO 93.4 (mA)
		LIFETIME CHANGE	0.0 TO 0.7 (min)	VACUUM CHANGE	0.10E-08 TO 0.49E-09 (Torr)
		CURRENT (mA)	TIME(min)	LIFETIME(min)	VACUUM (Torr)
		50.0	-	-	-
		100.0	-	-	-
		150.0	740.6	1389.6	0.85E-09
		200.0	386.3	1090.4	0.10E-08
		250.0	170.7	853.9	0.12E-08
		300.0	15.1	862.8	0.12E-08
EXPERIMENT	15:21:42 TO 04:00:07	ELAPSED	758.4 (min)	I*T	2634.9 (mA.H)
		AVERAGE	208.4 (mA)	CURRENT CHANGE	302.7 TO 147.4 (mA)
		LIFETIME CHANGE	0.0 TO 1407.8 (min)	VACUUM CHANGE	0.10E-08 TO 0.84E-09 (Torr)
		SHAR(min)	SHAR(mA.H)	SHAR(min)	SHAR(mA.H)
	BL01	748.2	2582.3	BL02	328.2
	BL03	-	-	BL04	753.2
	BL05	-	-	BL06	-
	BL07	746.3	2572.6	BL08	530.3
	BL09	401.4	1551.5	BL10	754.6
	BL11	795.4	2619.2	BL12	754.5
	BL13	-	-	BL14	-
	BL15	749.3	2589.4	BL16	-
	BL17	-	-	BL18	-
	BL19	-	-	BL20	-
	BL21	-	-	BL22	-
	BL23	-	-	BL24	-
	BL25	-	-	BL26	-
	BL27	-	-	BL28	-
COMMENT	CTR1.FITV.DATA(S6707D00) DATA COUNT= 1059				

Fig. 2.6.3 Run summary table

- of fast decay or large current, but fails to give the correct lifetime owing to the DCCT drift for an extremely long lifetime or low stored current.
- The operation status is displayed on a high-resolution dynamic scan graphic system (HP-1351A). A 17" monochrome display is divided into three frames. The first is for plotting long-range changes of stored current and lifetime with respect to the elapsed time after injection start. The second represents the injection rate with respect to the stored current. The last one shows short time current change, necessary for understanding precise status of decaying current.
 - All time-domain data are stored in common files with individual "RUN NUMBER" keyed in, so that the machine status is reported and plotted later. Operation data such as injection time, storage time, duration of channel use, and integrated current are stored in another file named local database. Figs. 2.6.2 and 2.6.3 show examples of a summary plot and a run report, respectively.
 - A graphic display for public information such as a plot of stored current decay is created by a microcomputer (SONY SMC70G), connected to the control computer via GPIB. The microcomputer sends an SRQ signal as "ready for new data" to the control computer

when a graphic data process is completed. A video display of the beam channel status from the control computer is also superimposed on this graphic frame.

- 5) A display of a safety interlock status is made as follows. In the normal operation, only a "ready to operate" message is presented and the detailed interlock status is hidden from the operator. When any trouble occurs, the wrong condition of interlock appears on the display in red or yellow letters so that the operator can easily see it.

2.6.3 Data Logging

Data on machine parameters are transferred from the front-end control processors to the M-360 library computer via a data-routing computer (Fig. 2.6.4). The front-end processors always determine the timing to send data; the library computer receives them at any time and then stores them into its database. In case that a fast control feedback is required, transfer and control tasks are processed separately in a multitask scheme. The routing computer, which receives various quantities of data with arbitrary timing, reserves data to control the network traffic. It also makes plots of data for monitoring if necessary.

Data are stored into a relational-type database of the library computer. First, the corresponding time and beam current of the data and indexes for a search are written in an index table; then, the data are saved into their own table (Fig. 2.6.5). This method makes it easy to accept various types and sizes of data and to add a new entry of data. The utility, ILM (Interactive Log data Manager) serves as an interactive tool to retrieve data and to make graphic plots from a TSS terminal without special programming. The flow of ILM is shown in Fig. 2.6.6.

Though only the data on RF and beam orbit position are currently logged for testing, about 0.3 Mbyte data are acquired a day during ordinary operation. It is scheduled to add such data as vacuum and magnet to the logging; thus, some data condensation will be necessary in the future.

Reference

1. Photon Factory Activity Report 1984/85 P. IV-14.

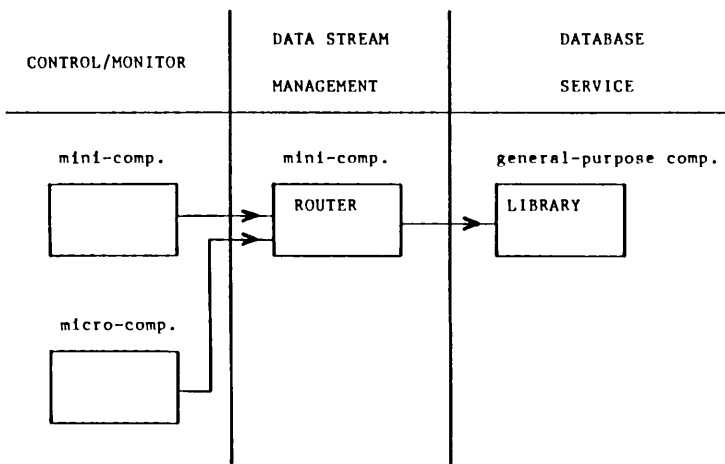


Fig. 2.6.4 Data transfer diagram

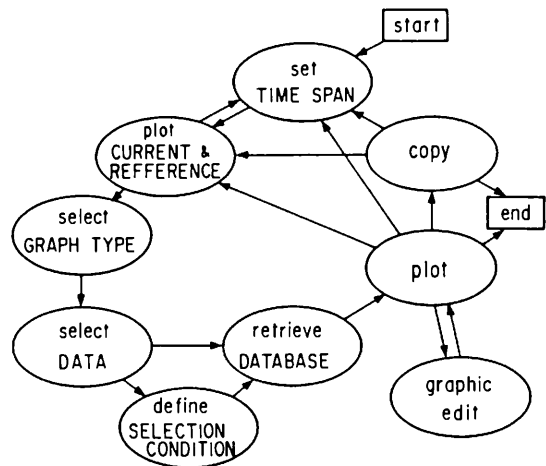


Fig. 2.6.6 Flow of ILM.

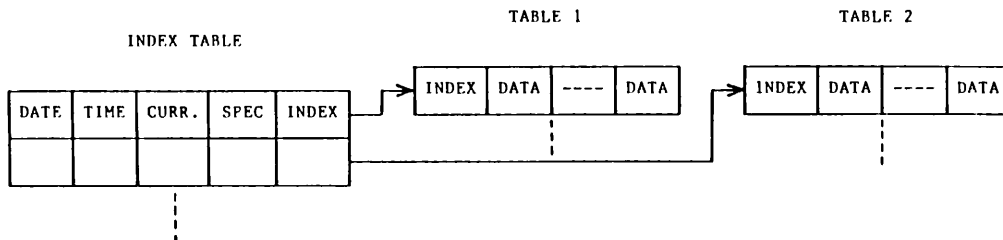


Fig. 2.6.5 Table format of the database

3. BEAM CHANNEL

3.1 GENERAL

The section concerning the beamline, which is almost common to all branch lines, is referred to as the front end. The front end, installed inside the shielding wall, was designed to utilize both vacuum ultraviolet (VUV) and X-ray parts of synchrotron radiation (SR) for many fields of science and technology. Because of spatial limitations arising from an adjacent quadrupole magnet on the straight section, most of the front ends were fabricated to extract an SR with a horizontal acceptance of 40 mrad. The front end consists of a vacuum protection system, a radiation safety system and an evacuation system with gauges and valves. At the termination of the front end, a beam-splitting section is connected. For VUV studies, splitting mirrors are installed in the section for delivering VUV parts of SR to spectrometers. First mirrors are made of CVD (chemical-vapor-deposited) SiC because of the high power density of SR. SiC is very resistant to thermal deformation and radiation damage. In contrast, pairs of beryllium windows are attached to the end of the splitting section for X-ray experiments.

The vacuum protection system consists of an acoustic delay line (ADL), a fast closing valve (FCV) and pneumatic isolation valves. Characteristics of the ADL and the FCV are described in elsewhere in some detail. The radiation safety system includes a water-cooled SR absorber and a 40 cm-thick stainless-steel beam shutter. The vacuum in the front end is kept in the order of 10^{-10} Torr by using three or four 110 /s triode ion pumps and two titanium sublimation pumps. Every front end with such components is controlled independently by the distributed control system, an application of computer network with a star topology. In this system, "outlying node" microcomputers (Z - 80 A) are distributed over all the front ends. They are concentrically connected to the "central node" computer (LSI - 11/23) via optical fiber links in a star topology. Under normal conditions, the outlying node controls all components of the beam lines without interference by the central node. When the control process monitor of the outlying node directly receives a Beamline-Open-Request (BLREQ) signal from the branch beamline users, the monitor in turn checks whether the status of the front end satisfies desired conditions or not. If all conditions are met, the monitor then sequentially opens all components on the front end. After completion of each opening, the monitor transmits the current status information to the central node via the network. Control information on the status of all front ends is observed at the central node by using an intelligent color graphic display. When an accidental failure occurs at a beamline, the outlying node shuts down the beam line; in turn, the central node will directly operate it in order to recover from the failure.

Users experiments stated with 8 front ends (25 experimental stations) in FY 1983. Up until the December of FY 1986, twelve beamlines (BL-1, 2, 4, 7, 8, 9, 10, 11, 12, 14, 15, 21) are in operation.

Status of beamlines is summarized in Table

3.1.1

3.2 NEW BEAM CHANNELS

BL-6 and BL-16

BL-6 is the fourth X-ray beamline from bending magnet B6. Front end components as well as branch beam shutters have been installed inside the shielding wall. The length of the front end is approximately 4.8 m and two thirds of that for BL-10. As a result, SR of a larger horizontal aperture is extracted for experiments even when the beryllium window with the standard size is attached to the downstream termination of the front end. As the termination of BL-6, three pairs of standard windows, such two "2 mrad" types and one "4.5 mrad" type, have been prepared. They are able to supply SR of 3.3, 7.1, 3.3 mrad in horizontal aperture to three branch lines; high angle-precision X-ray optics and protein crystallography (6A), a free port for white X-ray and EXAFS (6B), and diffraction studies under extreme experimental conditions (6C).

BL-16 is a new beam line specifically designed to exploit high-brightness synchrotron radiation from a 53-pole permanent-magnet wiggler in the wiggler/undulator regime. The wiggler can provide a photon flux two orders of magnitude higher than that obtained at bending-magnet beam lines. Consideration of this high power density is of essential importance in the design of beamline components which are to be struck by the beam. Table 3.2.1 shows some expected operating modes and corresponding radiation power densities produced by the wiggler at the designed maximum magnetic-field strength of $B_0 = 1.5$ T (wiggler mode). For a comparison, values are also given for a bending-magnet beam line (BL-11) and a superconducting vertical wiggler (3-pole wavelength shifter) beam line (BL-14). The average power density per unit solid angle ($P_{D,av}$) obtained from the wiggler is seen to be 77 and 16 times as high as those available at the bending-magnet and the superconducting wiggler lines, respectively. Hence, the beam-line components, which will be subjected to wiggler radiation, should have water-cooled sloping surfaces.

Figure 3.2.1 shows a side view of BL-16. The overall arrangement is similar to that of existing beam lines but several specific modifications have been made for some components. The first mask has a horizontal opening angle of 7 mrad. The maximum horizontal divergence of wiggler radiation is 2.5 mrad (standard deviation), so that the mask would not almost be struck by the beam. However, the mask was designed to have water-cooled sloping side walls by taking account of possible impingement of wiggler radiation caused by a variation in the electron-beam orbit as well as irradiation by the beams from bending magnets, B15 and B16. The absorber will intercept wiggler radiation to receive the full power. It is located 9.5-m away from the midpoint of the wiggler and the surface power density loaded on it ($W_{D,av}$) is 6.8-times higher in the wiggler line than $W_{D,av}$ in the bending-magnet line (Table 3.2.1). This ratio is considerably lower than that for the solid-angle

Table 3.1.1 Summary of Beamlines in FY 1986

Beamlines	Affiliation	Source	Spectral range	Status
BL-1	Nippon Telegraph and Telephone Corp, (NTT)	bending magnet, (B1)	VUV and Soft X-ray	in operation
BL-2	KEK-PF	60-period permanent magnet undulator	Soft X-ray	in operation
BL-4	KEK-PF	bending magnet (B4)	X-ray	in operation
BL-5	KEK-PF	permanent magnet wiggler/undulator	VUV and Soft X-ray	under designing
BL-6	KEK-PF	bending magnet (B6)	X-ray	completed (front end) under installation (branch lines)
BL-7	University of Tokyo	bending magnet (B7)	VUV and X-ray	in operation
BL-8	Hitachi Ltd.	bending magnet (B8)	VUV and X-ray	in operation
BL-9	Nippon Electrical Corp. (NEC)	bending magnet (B9)	VUV and X-ray	in operation
BL-10	KEK-PF	bending magnet (B10)	X-ray	in operation
BL-11	KEK-PF	bending magnet (B11)	VUV and Soft X-ray	in operation
BL-12	KEK-PF	bending magnet (B12)	VUV	in operation
BL-14	KEK-PF	super conducting vertical wiggler	Hard X-ray	in operation
BL-15	KEK-PF	bending magnet (B15)	X-ray	in operation
BL-16	KEK-PF	53 poles permanent magnet wiggler/undulator	Soft X-ray	under construction
BL-17	Fujitsu Ltd.	bending magnet (B17)	VUV and X-ray	completed (front end) under construction (branch lines)
BL-19	ISSP and KEK-PF	permanent magnet multi-undulator	VUV	under construction
BL-21	KEK-PF	bending magnet (B21)	white, visible light and X-ray (branch line)	in operation under construction
BL-27	KEK-PF	bending magnet (B27)	infrared and white	under installation
AR line	KEK-PF	bending magnet of Accumulation Ring (AR)	Hard X-ray	under installation

Table 3.2.1 Radiation power densities and other related parameters for a 53-pole wiggler (BL-16), a bending magnet (BL-11) and a superconducting vertical wiggler (3-pole wavelength shifter; BL-14) beam lines. Here, K is a field parameter, P_T total radiated power, $2\Delta\theta_x$ and $2\Delta\theta_y$ horizontal and vertical power divergence, $P_{D,av}$ average power densities per unit solid angle, L_{ab} the distance between the midpoint of the source and an absorber, and $W_{D,av}$ average power densities per unit area at the location of the absorber. The powers for the 53-pole wiggler are shown at its maximum field strength ($B_0 = 1.5$ T).

	MPW (53p)		BEND	VW (3p)
I (mA)	350	500	500	500
B_0 (T)	1.5		0.963	6.0
K	16.8			
P_T (kW)	10.2	14.6		20.7
$\Delta\theta_x$ (mrad)	2.48			0.19
$\Delta\theta_y$ (mrad)	0.21		0.21	
$P_{D,av}$ (kW/mrad ²)	3.2	4.6	0.06	0.28
$W_{D,av}$ (kW/cm ²)	3.6	5.1	0.75	0.57
L_{ab} (m)	9.5		2.8	7.0

power density ($\times 77$), which is the result of a longer distance between the absorber and the source in the wiggler line than in the bending-magnet line. Thus, the absorber was designed to have a horizontal slope of $\sim 1/3$ to reduce the surface power density to a level only 2 times as high as that in BL-11. Cooling is made with water flowing through the inside. The most severe problem is protection of the shutter blade of a fast valve from exposure to wiggler radiation, anticipated in the case of a downstream vacuum failure. Although the fast valve can be closed within ~ 15 msec, closing the absorber needs at least ~ 1 sec. With a 1.5-T wiggler field and a 500-mA circulating beam, the temperature of the shutter blade (made of titanium) will reach the melting point of Ti in ~ 80 msec if the blade is subjected to a high power load. It is practically difficult to make the fast valve be water-cooled. Therefore, to cope with this problem, the only feasible method of damping the electron beam by turning off the RF power with initiation of the fast-valve closure was employed; such a system has been used for the 55-pole wiggler/undulator beam line at SSRL.

BL-19 and BL-5

The construction of BL-19 is a joint project between ISSP (Institute for Solid State Physics), University of Tokyo and KEK-PF starting in FY 1986. BL-19 is a beamline for a new type of the multi-undulator which is designed to span spectral range of 10 \sim 1000 eV. Four combinations of undulator periods are possible by using a rotation mechanism. As a result, undulators with 13, 22, 31 and 45 periods are installed in the available straight section between B18 and B19. The corresponding period lengths are 16.4, 10, 7.5 and 5 cm, respectively. BL-19 accepts undulator radiation of 7 mrad (H) \times 3.5 mrad (V). Proposed experiments are spin-polarized photoemission experiments, photoemission studies at

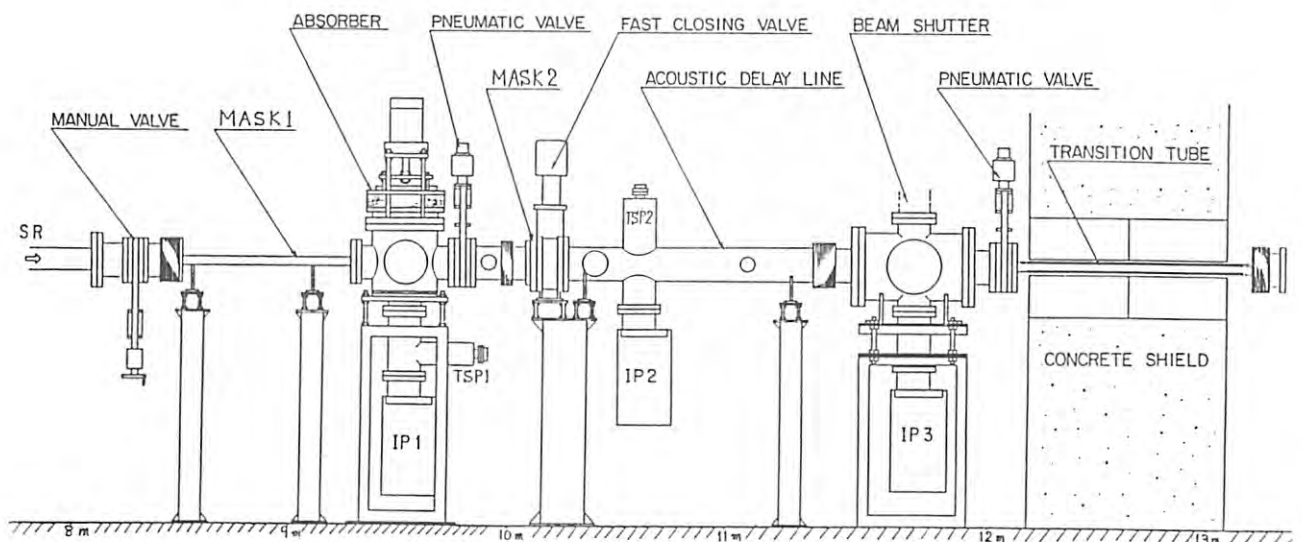


Fig. 3.2.1 Elevation view of the 53-pole wiggler/undulator main beam line (BL-16).

variable temperatures and experiments on photo-emission from surfaces and interfaces.

The radiation source of BL-5 is planned to be a multipole wiggler/undulator. Specifications for the source is not definite at present. However, the front end of BL-5 is designed to endure irradiation by the high photon flux from the multipole wiggler. The structures of BL-5, therefore, have many similar features to those of BL-16.

4. INSERTION DEVICES

4.1. GENERAL

The first step in the development of the insertion devices of the Photon Factory (PF) was the successful test operation of the 10-period undulator, which was carried out in FY1981. At that time the PF ring was under construction, so the undulator was installed in the SOR-RING of ISSP, the 0.38-GeV storage ring dedicated to spectroscopy. In the test, the absolute intensity of the radiation was measured and the polarization characteristics were studied. The results confirmed that the undulator will be an important device as a highly brilliant synchrotron radiation source in the near future. In addition to the requirements for such brilliant radiation, a high-energy radiation up to 100 keV with vertical polarization is also required.

Therefore, the construction of the superconducting wavelength sifter was proposed in 1975, and the preliminary study concerning the technology of superconducting magnets started in 1976.

The PF ring was successfully operated at the end of FY1981; in FY1982 two insertion devices were installed in the straight sections of the ring. One is the superconducting vertical wiggler (VW: wavelength shifter), located at the B13-B14 3.55-m straight section (Fig. 4.1.1) with a maximum magnetic field of 6 tesla for the utilization of vertically polarized high-energy photons up to 100 keV. The other is a 60-period undulator (B02 undulator) located at a B01-B02 5-m straight section, with a spatial period length of 6 cm. The undulator consists of a rare earth-magnet of SmCo_5 (pure configuration) with a maximum field of 0.31 tesla; it can deliver highly brilliant radiation from 400 to 5000 eV. As these insertion devices work well so far with improvements of the beam performance with the stability of the stored beam, requirements for high-energy or highly brilliant radiation have increased.

Under the above situation, a project involving a 26-period multi-pole wiggler (B16 MPW) started in 1984. The MPW with a period length of 12 cm is intended to be a highly brilliant source in the photon energy range from 0.03 to 30 keV. The magnet structure is a hybrid type. It consists of a NdFe permanent magnet (NEOMAX30H) and

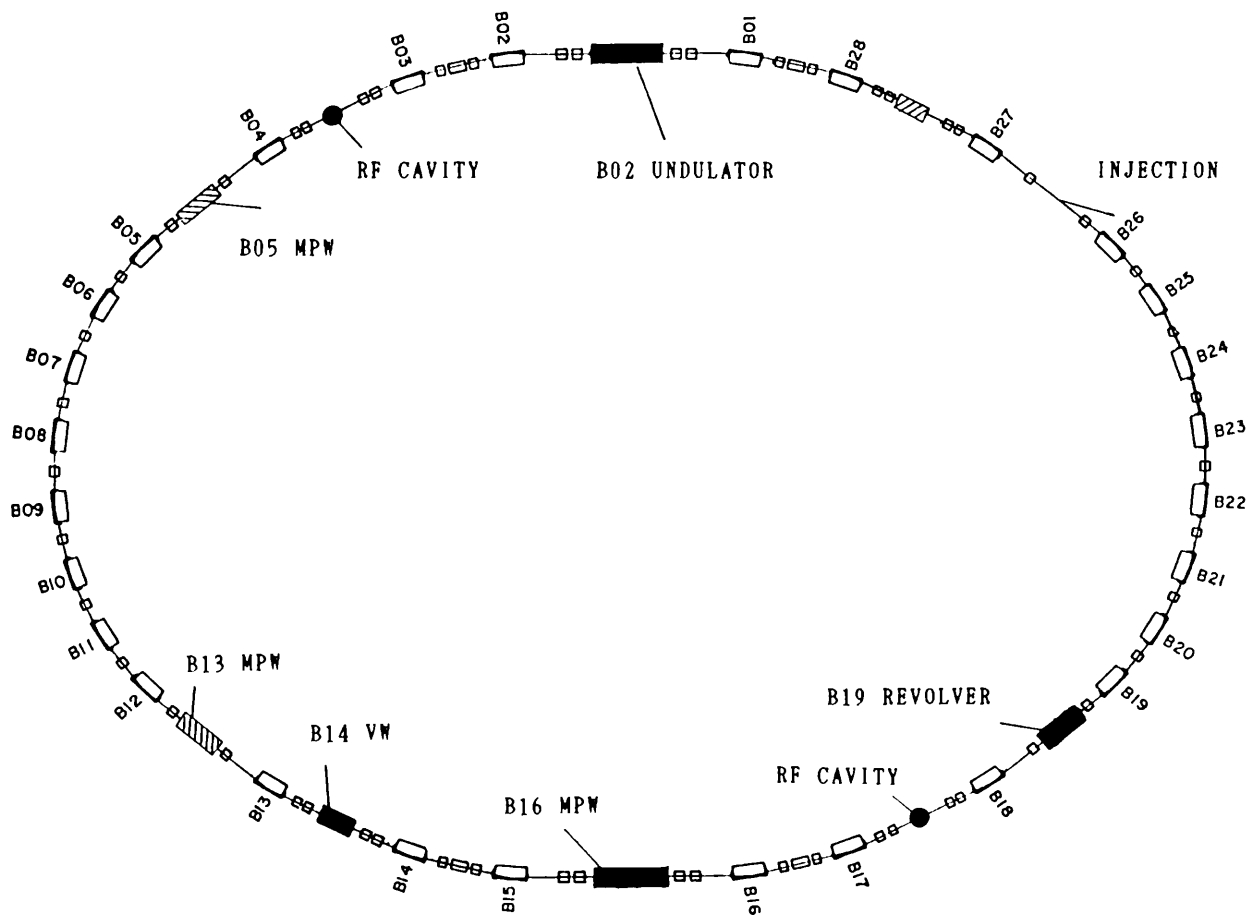


Fig. 4.1.1. Locations of the insertion devices in the PF ring.

a permendur. The magnetic field is variable up to 1.52 tesla; thus, different operation modes (wiggler mode (fixed at 1.52 tesla) or undulator mode (0.05 ~ 0.5 tesla)) can be chosen. This device will be installed in the B15-B16 5-m straight section at the end of FY1986.

On the other hand, the requirement for high-energy radiation up to 100 keV has been left unsatisfied. However, all of the unoccupied straight sections (B04-B04, B12-B13, B18-B19) have relatively large dispersions ($\eta \geq 1$ m). Therefore, the installation of the next superconducting wiggler as a high-energy radiation source is quite difficult because the existence of such a high field device sometimes increases the beam emittance while lowering the brilliance of radiation if it is located at the section with finite dispersion.

Fortunately, the Accumulator Ring (AR) of 6 GeV, which has been operated as an injector for the main ring of TRISTAN project, is available as the synchrotron radiation source. It was confirmed that the spectral intensity of the radiation from the bending magnet of AR is not lower than that of VW in the PF ring. Therefore, it has been concluded that the PF ring should be developed as a brilliant source while the facility for high energy radiation source should be constructed around the AR ring.

According to the above strategy, the reconstruction of the PF ring for lowering the emittance from $\epsilon = 4.0 \times 10^{-7}$ to 1.3×10^{-7} m \cdot rad was made in Aug. 1986^x. It is expected that the characteristics of the radiation emitted from the insertion devices will be greatly improved. In addition to this advantage, the other straight section (B27-B28) will be available for an insertion device, since one of the quadrupole magnet located there can be removed with the kicker magnet being made small by using ferrite as the core material, after establishing low-emittance operation. Hence, we have 7 straight sections for insertion devices, three of which are occupied or reserved by the devices above mentioned. Furthermore, two more insertion devices are scheduled as mentioned below.

The gain of the spectral brilliance obtained by lowering the emittance is quite remarkable. Fig. 4.1.2 shows the spectra of the radiation from the B02 undulator calculated for both low and high emittance modes. Furthermore, other characteristics are improved. Table 4.1.1 shows the peak value, bandwidth and polarization of each odd harmonic compared between both modes. Figure 4.1.3 shows the spectra of various insertion devices calculated based on the beam parameters of low-emittance optics. In this figure, the spectral curve of each undulator is a

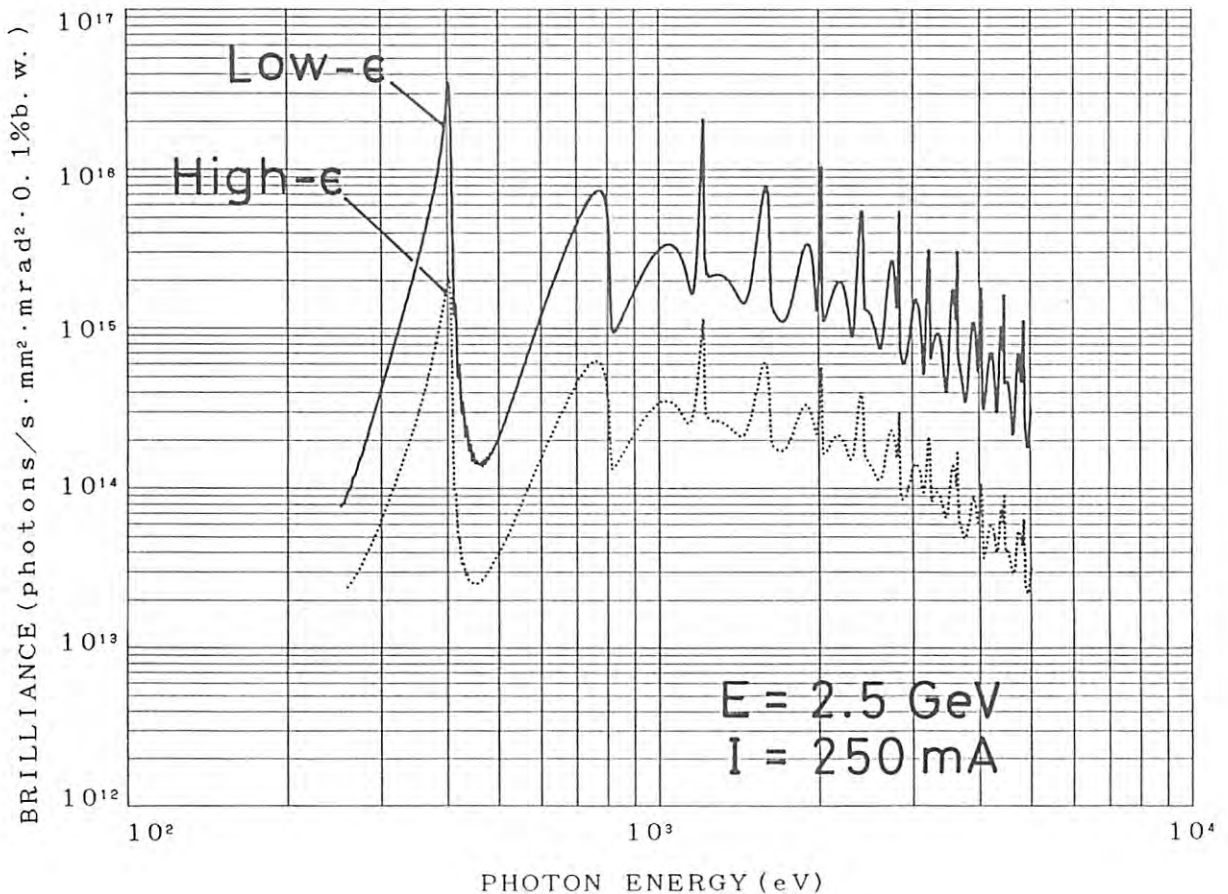


Fig. 4.1.2. Spectra of B02 undulator at the K value of 1.7. The full or dotted curve shows the spectrum in the low-emittance mode ($\epsilon_x = 1.3 \times 10^{-7}$, $\epsilon_y = 4 \times 10^{-9}$ m \cdot rad), or high-emittance mode ($\epsilon_x = 4 \times 10^{-7}$, $\epsilon_y = 1.2 \times 10^{-8}$ m \cdot rad), respectively.

Table 4.1.1 Spectral characteristics of the radiation obtained from the B02 undulator (K=1.7) in the low emittance mode with the beam current of 250 mA. The values in the brackets correspond to the high emittance mode.

n	BRILLIANCE	$\Delta \lambda/\lambda$	POLARIZATION
1	3.47E16 (2.08E15)	0.031 (0.050)	99.96 % (99.67)
3	9.47E15 (1.15E15)	0.0059 (0.023)	99.79 % (99.51)
5	4.92E15 (5.74E15)	0.0036 (0.0136)	99.70 % (99.15)

locus of the peak of the first harmonic generated by changing the K value up to its maximum.

The brilliance of the bend sources is also improved by a factor of 3 ~ 20 (Fig. 4.1.4). However, the gains at the bending magnets of the normal cell are found to be relatively low, because the beam sizes σ_x and σ_y in these magnets are not decreased remarkably. Table 4.1.2 shows the parameters related to the bend sources of five different types: normal cell-A (B06, B08, B10, B12, B20, B22), normal cell-B (B07, B09, B11, B21, B23, B25), B01 (B15), B03 (B17), and B04 (B18).

The multi-undulator (REVOLVER, ISSP-KEK) is under construction and will be installed in the B18-B19 3.75-m straight section in FY1987. This undulator consists of four magnet systems with different period lengths, so that the problem related to wide range tunability (from 10 to 1100 eV) may be resolved. Since the magnet systems are arranged around a beam made of stainless steel, the choice of each magnet system can be achieved by rotating the beam like a revolver of the pistol. The reason why we adopted such a design is that the tunnel of the PF ring is too

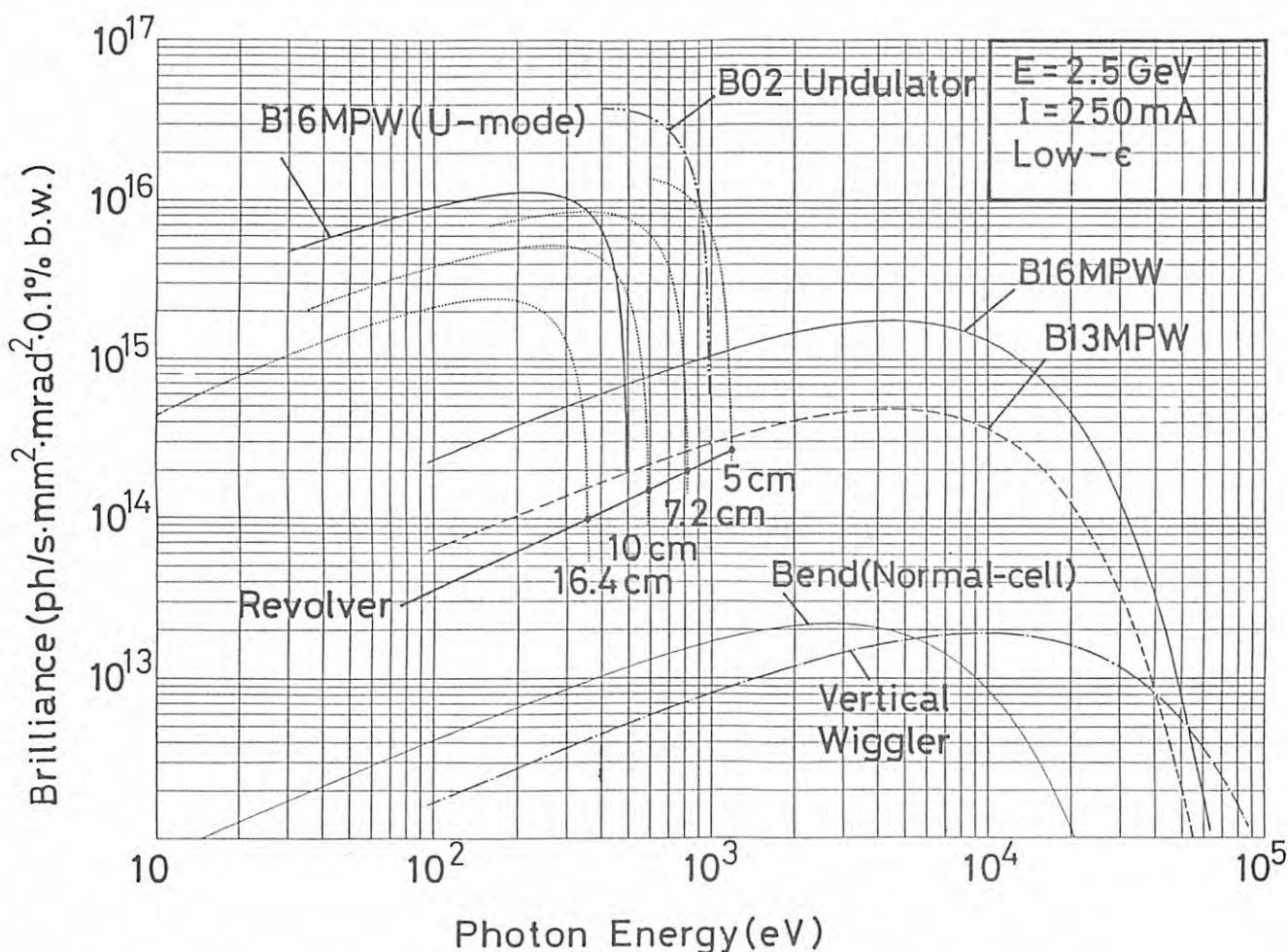


Fig. 4.1.3. Spectra of the insertion devices in the PHOTON FACTORY. The spectral curve of each undulator is a locus of the peak of the first harmonic generated by changing the K value up to its maximum.

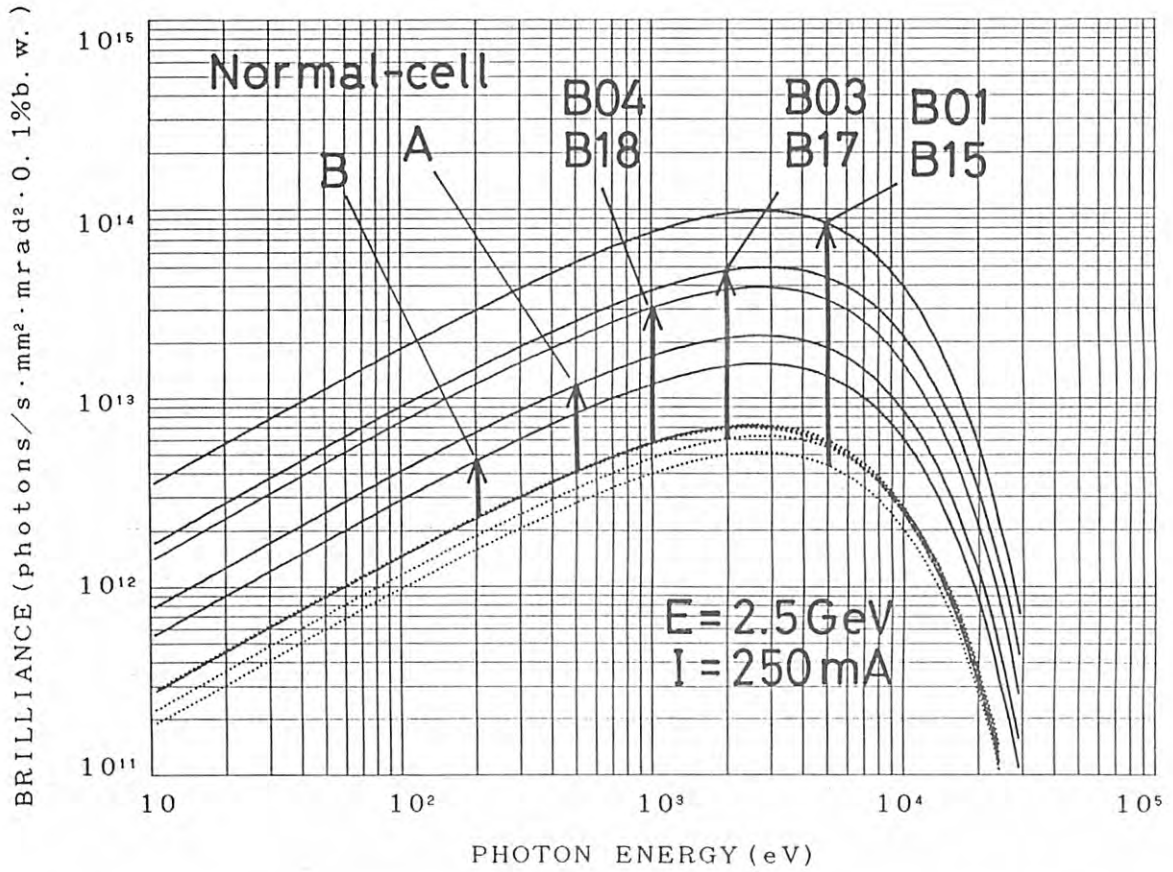


Fig. 4.1.4. Spectra of the bend sources of five different types. The full or dotted curves show the spectra in the low-emittance mode ($\epsilon_x=1.3 \times 10^{-7}$, $\epsilon_y=4 \times 10^{-9}$ m·rad), or high-emittance mode ($\epsilon_x=4 \times 10^{-7}$, $\epsilon_y=1.2 \times 10^{-8}$ m·rad), respectively.

Table 4.1.2 Main parameters related to the bend source of five different types in the low-emittance mode. Normal cell-A: B06, B08, B10, B12, B20, B22. Normal cell-B: B07, B09, B11, B21, B23, B25. The values in the brackets correspond to the high-emittance mode.

CHANNEL	BRILLIANCE 1 keV	BRILLIANCE 10 keV	σ_x mm	σ_y mm	$\sigma_{x'}$ mrad	$\sigma_{y'}$ mrad
Normal cell-A	1.68E13 (5.69E12)	8.55E12 (2.41E12)	0.753 (1.805)	0.330 (0.387)	0.388 (0.530)	0.047 (0.084)
Normal cell-B	1.19E13 (5.80E12)	6.04E12 (2.46E12)	1.443 (2.674)	0.244 (0.256)	0.413 (0.546)	0.047 (0.084)
B01,B15	7.60E13 (4.01E12)	3.91E13 (2.01E12)	0.397 (2.439)	0.139 (0.427)	0.399 (0.283)	0.044 (0.049)
B03,B17	3.76E13 (4.82E12)	2.13E13 (2.58E12)	0.476 (1.834)	0.238 (0.479)	0.336 (0.375)	0.017 (0.035)
B04,B18	3.05E13 (5.80E12)	1.52E13 (2.62E12)	0.605 (2.621)	0.226 (0.267)	0.294 (0.465)	0.050 (0.071)

Table 4.1.3 Main parameters of each insertion device in the PHOTON FACTORY. MPW-U: wiggler or undulator mode available. U: undulator. WS: wavelength shifter. P: pure configuration. H: hybrid configuration. U_{1s} : radiation loss. F: magnetic force.

CHANNEL TYPE	λ_u cm	N	G_{min} cm	B_{max} T	K_{max}	$h\nu$ keV	U_{1s} keV	σ_x mm	σ_y mm	$\sigma_{x'}$ mrad	$\sigma_{y'}$ mrad	F kgf	STRUCTURE	COMPLETION
B02	U	6.0	60	2.8	0.3	1.7	.4~5.0	1.37	0.655	0.225	0.203	.0177	630 P(SmCo ₅)	'83 Jan.
B05	MPW-U	8.0	24	1.8	0.8	6.0		7.6	1.681	0.219	0.148	.024	3500 H(NdFe-PR)	
B13	MPW-U	12.0	18	1.8	1.5	16.8	.03~70	17.1	1.681	0.219	0.148	.024	7800 H(NdFe-PR)	'88 Sept.
B14	WS			5.0	6.0		≤100	50.0	1.205	0.15	0.193	.027	S.C.	'82 Dec.
B16	MPW-U	12.0	26	1.8	1.5	16.8	.03~70	27.8	0.655	0.225	0.203	.0177	13500 H(NdFe-PR)	'87 Jan.
B19	U	5.0	45	3.0	0.3	1.4	.01~1.1	0.80	1.681	0.219	0.148	.024	380 H(NdFe-PR)	'87 Sept.
		7.2	31	3.0	0.4	2.7		1.41					670 H(NdFe-PR)	
REVOLVER		10.0	22	3.0	0.6	5.6		3.1					1500 H(NdFe-PR)	
		16.4	13	3.0	0.6	9.2		3.0					2000 P(NdFe)	

narrow to allow an SSRL type multi-undulator where the period length is chosen by sliding the magnet systems in the transvers direction. In addition to the above undulator, another multipole wiggler (B13 MPW) with a design similar to that of the B16 MPW (except for the number of periods) will be installed in the B12-B13 3.75-m straight section in FY1988. Table 4.1.3 shows the main features of each insertion device in the PF ring; here, the design parameters of B04-B05 device are tentative.

4.2. OPERATION OF B02 UNDULATOR

The features of the B02 undulator are listed in Table 4.2.1. Although the B02 undulator has been operated well for four years, several problems to be resolved have been encountered. One of them is that the γ -ray emitted by the scattering of stored electrons by residual gases has the same direction as that of the synchrotron radiation from the undulator, which causes not only the background in the instrumental data but a radiation hazard for the users. In order to lower the intensity of the γ -rays down to the allowable level, the vacuum chamber equipped for the undulator, which has no pumping system at present, should be exchanged for a new one with appropriate pumps so that the pressure at the location of the undulator may be improved from 5×10^{-9} to 5×10^{-11} torr. Another problem is that the permanent magnet pieces mounted on the aluminium holder by epoxy resin have sometimes been dislocated and chipped off. Therefore, the magnetic characteristics of the undulator were somewhat changed, even if they were remounted. As a result, the closed orbit of the stored beam was distorted in the horizontal and vertical directions, so that the photon beam axis fluctuated when the magnetic gap of the undulator was varied as described in the Section 2.5. In order

Table 4.2.1 Main parameters of B02 undulator.

Structure	pure (SmCo ₅)
Undulator period	6.0 cm
Number of period	60
Gap	2.8 ~ 8.0 cm
Magnetic field	.31 ~ .015 T
K value	1.7 ~
Magnet width	9.0 cm
Magnet height	1.5 cm
Transvers good field	
aperture (gap=2.8 cm, $\Delta B/B \leq 1\%$)	2.4 cm
Peak field uniformity (std)	
(gap=2.8 cm)	0.7 %
Beam vertical aperture	2.1 cm
Magnetic force (max.)	630 kgf

to correct the above situation and to increase the magnetic field, all the magnet pieces will be exchanged from SmCo₅ (Br=0.9 tesla) to NdFe (NEOMAX35H: Br=1.25 tesla) in near future, and they will be mounted by mechanical holding method. The maximum field will be 0.41 tesla (K=2.3) at the gap of 28 mm with the lower photon energy limit being extended to 270 eV.

4.3 SUPERCONDUCTING VERTICAL WIGGLER

Some improvements concerning the stability of the photon beams and the beam lifetime due to the wiggler operation have been achieved as follows.

4.3.1 Movement of the photon beam in relation to the power supplies of the wiggler magnets

The photon-beam position moved during the transfer procedure of liquid helium from a container to the wiggler cryostat.

The transfer of helium is usually performed every five hours.

During a transfer, the current feed-through of the wiggler magnets is cooled by a large quantity of the evaporated helium gas. Consequently, their electric resistance are decreased.

Though the power supplies for the wiggler are the constant-current type, a protection resistor to prevent the wiggler from destruction due to quenching has been connected to the superconducting wiggler coils in parallel.

The ratio of the resistance between the coils (including feed-throughs and the protection resistor) changes during a transfer. The power supplies control only their total output current. Therefore, the transfer produces variation in the exciting current of 8.8×10^{-2} %. This current fluctuations correspond to a photon beam movement of $300 \mu\text{m}$ in the vertical direction 12-m downstream from the source point.

By means of changing the location of the protection resistor into the control loop of the power supply where it has no influence on the coil currents, the fluctuation in the coil current became less than 2×10^{-3} %. Consequently, the movement of the photon beam due to the transfer was no longer observed.

Another movement of the photon beam caused by a pocket bell (beeper) was found. The output cables of the wiggler power supplies behave as an antenna and pick up the beeper signal. The signal was rectified in the power supplies of the wiggler so that the regulation of the coil current was affected. This gave a fluctuation of the light axis with the amount of $16 \mu\text{m}$ observed at the location as mentioned above. The beeper's antenna nearby wiggler region was removed in the meantime.

4.3.2 A new correction method of the tune shifts

Betatron tune shifts caused by wiggler operation was corrected with the ring quadrupole magnets collectively.

Instead of such total correction, a local correction has been made with two quadrupole magnets located both on the up- and downstream sides of the wiggler in the same straight section. As a result of the local correction, the effective aperture of the wiggler duct became wider than in the case of the total correction. In the Fig. 4.3.1, the dependences of the beam lifetime on the displacement of the closed orbit is shown in these two cases.

4.3.3 A cure for the non-linear field effect during operation

Non-linear fields (especially the sextupole field component) of each wiggler coil affect orbit parameters. Consequently, a shift in the betatron frequency appeared and a stable region in a tune diagram became narrow as the wiggler excitation increased.¹⁾

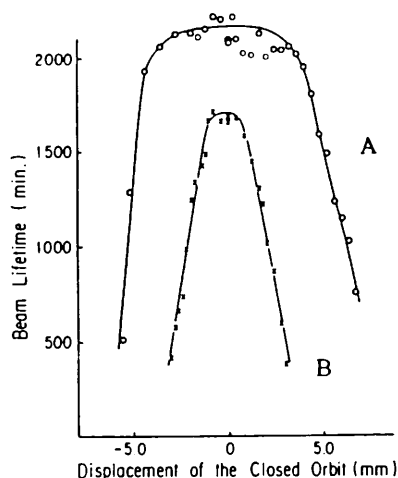


Fig. 4.3.1 Dependences of the beam lifetime on the displacement of the closed orbit. A: Local tune correction, B: Total tune correction.

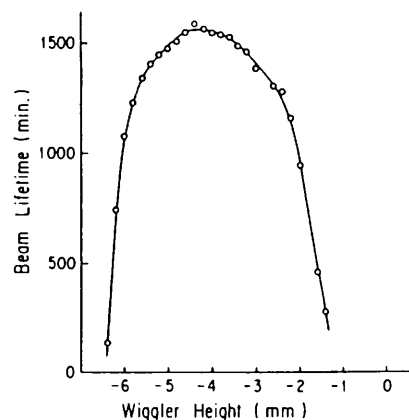


Fig. 4.3.2 Beam lifetime as a function of the wiggler height.

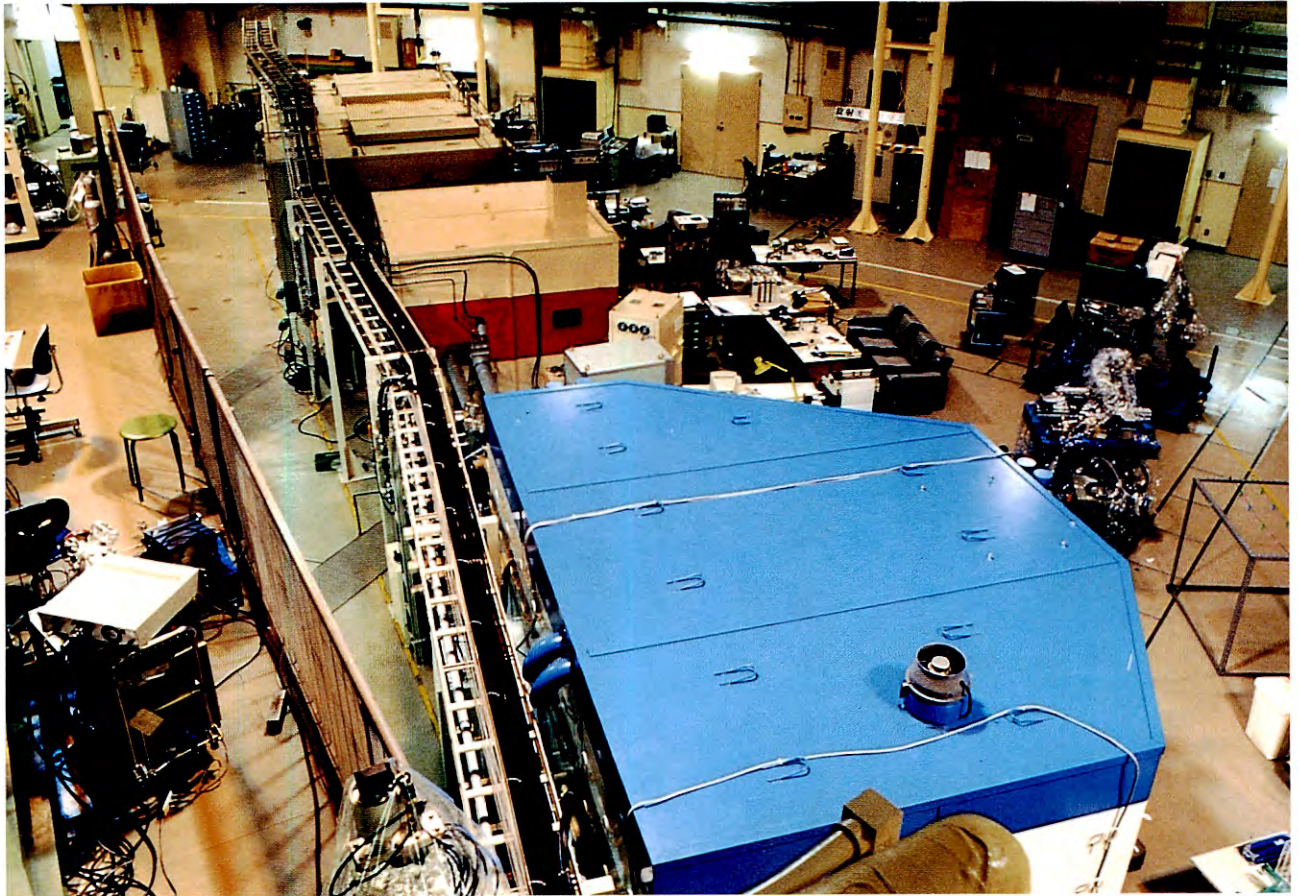
The magnitude of the sextupole field component on the electron orbit depends on both the central field strength and the orbit displacement from the center of the wiggler magnet.²⁾ Naturally, the optimum height of the wiggler depends on the wiggler excitation.

If the center of the central coil is put close to the middle point of the orbit bump in the wiggler, the sextupole field component by the central coil decreases on the orbit. On the contrary, the component having an inverse polarity by the outer coils increases. Consequently, the integration of these components along the orbit becomes smaller.

In the Fig. 4.3.2 the beam lifetime at wiggler field of 5 tesla is shown as a function of the wiggler height (which corresponds to the vertical displacement of the magnet center).

- 1) A. Araki et al Proc. of the 5th Sympo. on Acc. Sci and Tech. P283 ~ 285
- 2) T. Yamakawa et al Nucl. Instrum. and Meth. in Phys. Research A 246 (1986) 32 ~ 36

Instrumentation Department



A overhead view of the newly constructed beam line BL-6

1. BEAM LINES AND OPTICS

1. Beam Lines

At the beginning of 1986, the construction of three beam lines (BL-7, BL-8 and BL-21), whose design and performance were specified in the 1984/85 issue of this report, was almost completed and final adjustments and test measurements were made. Increasing demands for light sources for scientific research and industrial applications influenced our decision to construct new beam lines. KEK-PF, supported by the Government, has started construction of BL-6 and Nippon Electric Company (NEC), based on their research fund, has started construction of BL-9 in collaboration with KEK-PF.

Along with the construction work of the new beam lines, efforts have been made to improve the equipment designs, their control systems and the maintenance equipment of old beam lines and their branches, particularly, BL-1A, BL-2, BL-10B and BL-15B. The improvements contribute much to the levelling up of research work to be done at these lines and branch lines.

Protection against hazards due to synchrotron radiation is always an important subject and efforts to improve the quality of the safety system are being continuously made.

In the following a description is given regarding the two new beam lines, along with a description of additional features of BL-7. The following four sections show how four beam lines (and their branch lines) have been improved. The last section outlines the performance of the new safety system.

Beam Line 6

A layout of the beam line is shown in Fig. 1. Synchrotron radiation to be provided to each branch beam line is divided at 5.8 m from the source point by a water-cooled mask; directly downstream are placed three independent Be windows. An SR shutter system which functions

as a γ -ray shield is in a single box where three sets of double lead blocks are installed with water-cooled copper blocks in front. Downstream of this shutter is located three branch beam line pipes, in which a water-cooled mask is placed for better beam collimation. In order to make maintenance easier, all the branch beam lines are turbo-molecular pumped between the Be windows and the back-end windows in each hutch (they were hitherto evacuated with a rotary pump). Completion of the whole beam line system is scheduled for December 1986.

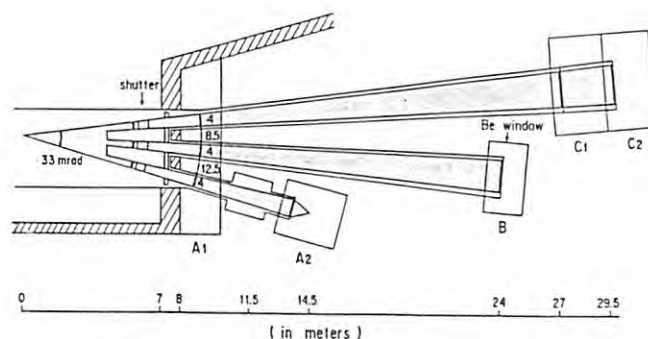


Fig. 1 Layout of Beam Line 6. Each branch line has an aperture of 4 mrad.

BL-6A

This beam line is for studies using a very high-resolution small-angle scattering (SAS) camera (6A1) and a multi-layer Weissenberg camera for macromolecular crystallography (6A2). For BL-6A1 a white beam is provided, which is monochromatized by a flat silicon crystal for SAS optics using Bonse-Hart type channel cut monochromators. For BL-6A2 a white beam of 4 mrad in aperture that is focussed by a cylindrical mirror of fused silica is provided; it is monochromatized by a bent silicon crystal installed in a hutch. Either station 6A1 or 6A2 is in operation at a particular time.

Table 1. Characteristics of BL-6.

Branch line	Horizontal acceptance (mrad)	Mirror	Monochromator	Wavelength range (Å)	Typical applications
6A1	4	—	flat silicon	0.4 — 3.0	very high angle-resolution SAS
6A2	4	vertical focussing	bent silicon	0.4 — 3.0	macromolecular crystallography
6B	4*	—	not yet installed	0.4 — 3.0	EXAFS
6C1	4	—	not yet installed	0.4 — 3.0	low-temperature diffraction
6C2	4	—	—	0.4 — 3.0	precision measurements of lattice parameters

* The shutter room inside the storage ring radiation shield is designed so that this number can be increased when necessary.

BL-6B

This branch beam line will serve for a while as a white beam station. It will be converted into an EXAFS station in the near future. The beam aperture is 4 mrad, but it can be made as large as 6 mrad when necessary.

BL-6C

This branch beam line also comprises of two stations (6C1 and 6C2) disposed in tandem. At present, no monochromator is installed. The former station is for low-temperature diffraction experiments, while the latter is for such experiments as precise lattice parameter determinations, which fully utilize the station characteristics.

Table 1. lists the characteristics of BL-6.

Beam Line 9

The principal beam available at this beam line has a divergence of 36 mrad in the horizontal direction and 4 mrad in the vertical direction; this is divided into four branch line by a beam mask. Two of them have already been constructed. One is an X-ray lithography line and the other is a hard X-ray diffraction line, called BL-9A and BL-9C, respectively. The third one, BL-9B, which is now under construction, is a VUV line designed for the investigation of photo-chemical reactions. A fourth line, BL-9D, will be constructed as a soft X-ray line in the future. The layout of the beam line is schematically shown in Fig. 2. The design and construction of the beam line were carried out by Fundamental Research Laboratories, Micro-Electronics Research Laboratories, Opto-Electronics Research Laboratories, and R & D Planning and Technical Service Division of NEC Corporation in cooperation with KEK-PF. An overhead view of the beam line is shown in Fig. 3.

Front End

The basic design of the front end follows that of the PF beam line, BL-11. In order to protect the vacuum of the storage ring from an accidental breakdown, an acoustic delay line (ADL) and a fast closing valve (FCV) were installed in the beam line. It takes about 34

msec to close the FCV from the time when the sensor (located just downstream of an ADL) detects a vacuum breakdown. A pneumatic valve, having an effective hole of 12 in. diameter with 14 in. conflat flanges, is located at the last part of the front end for maintaining a high vacuum in the storage ring against a vacuum breakdown at the branch beam lines.

BL-9A

In this branch line, the synchrotron radiation lithography system has been developed which was designed for fundamental experiments. The beam line was constructed in April 1986, followed by the installation of an exposure chamber in June 1986 (located 25.5 m from the source point). The system is evacuated up to 10^{-9} Torr, including the exposure chamber. For the purpose of enlarging the uniform exposure area vertically, an oscillating mirror system, (19 m from the source point) has been developed. Preliminary exposure results were obtained using this system.

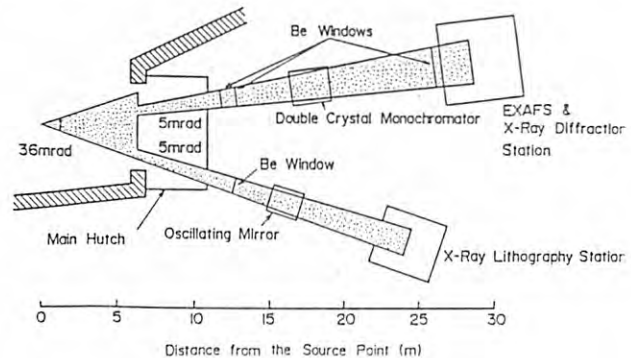


Fig. 2 Layout of Beam Line 9.

BL-9C

This branch line was designed for hard X-ray diffraction and EXAFS experiments and was constructed at the end of 1985. The line comprises (1) two Be windows located at a distance of 13 m from the source point, (2) slit systems, (3) a double-crystal monochromator located at a distance of 22 m from the source point, (4) two vertical-type diffractometers

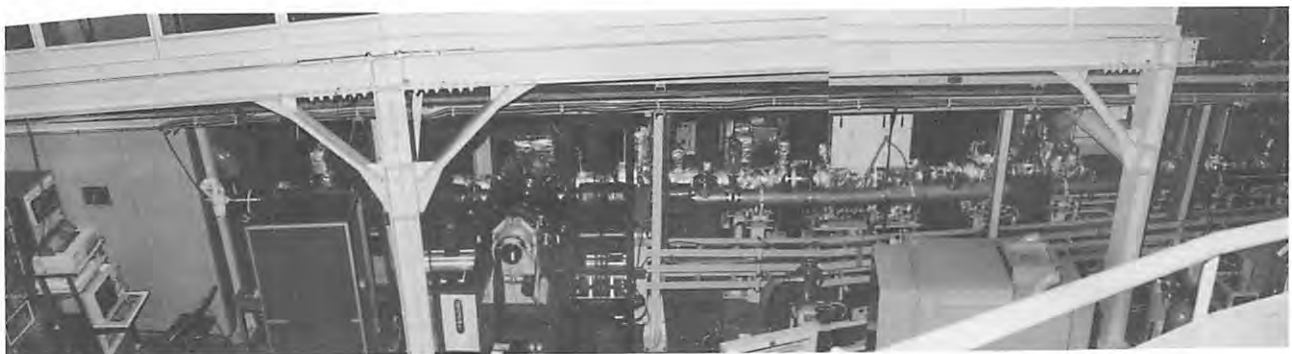


Fig. 3 An overhead view of Beam Line 9.

and/or an EXAFS spectrometer, and (5) a hutch station in which the end parts of the line and either a diffractometer or an EXAFS spectrometer are accommodated. The end part of the line comprises a Be window which separates the 10^{-3} Torr line from the atmosphere and a small space filled with flowing He gas. A Kapton window is used to separate this helium path from the air in the experimental hutch. Either a white X-ray beam or a monochromatized X-ray beam can be selectively used for the experiment. A white beam (6 in. W x 0.5 in. H as a maximum size) is available at a distance of 30 m from the source point. A monochromatized, focused X-ray beam can be obtained using the double-crystal monochromator originally designed by Prof. Matsushita of KEK-PF. The vertical position of the monochromatized beam is higher than that of the white beam by 25 mm (which is kept constant even upon changing the wavelength of the X-ray beam). The diameter of the beam line duct after the monochromator is sufficiently large to introduce these two beams.

Beam Line 7

The construction of BL-7 was completed in 1985/1986 under collaboration between the Research Centre for Spectrochemistry of the Faculty of Science, the University of Tokyo and KEK-PF. All components, including the interlock system, have been completed. The first test introduction of SR into the beam channel and that into the branch lines were successfully carried out in October 1985 and in January 1986, respectively. The prefocusing mirror apparatus and the monochromator of each branch line are presently undergoing performance tests. The beam line will be put in use within FY 1986.



Fig. 4 Side view of the plane grating monochromator (BL-7A).

BL-7A

BL-7A is a soft X-ray line which covers an energy range from 1000 to 10 eV. This branch line comprises a plane grating monochromator and a prefocusing mirror apparatus. The design principle of the branch line was described in the 1984/85 issue of this report. Illustrations of the plane grating monochromator are shown in

Fig. 4. Figure 5 shows a rotatable grating holder for selecting one of the two gratings and two of four plane mirrors acting as a high-energy cut filter (installed in the main chamber of the monochromator). The branch line is now undergoing performance tests. Experiments involving angle-resolved photoelectron spectroscopy, surface EXAFS, photon-stimulated desorption, etc. are planned.

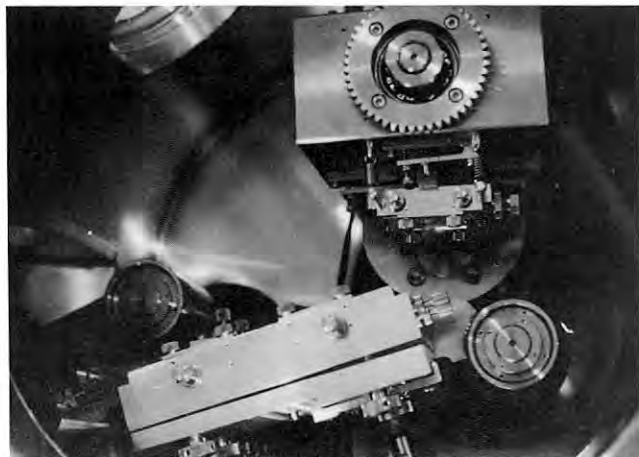


Fig. 5 Inside view of the grating chamber (BL-7A).

BL-7B

BL-7B is a VUV line comprising a 1-m Seya-Namioka monochromator with a prefocusing mirror apparatus. The optical system has been previously described. An illustration of the monochromator joined with a photoelectron spectrometer is shown in Fig. 6. This branch line is also undergoing performance tests. Experiments concerning surface photochemical reactions and photoelectron spectroscopy are in preparation.

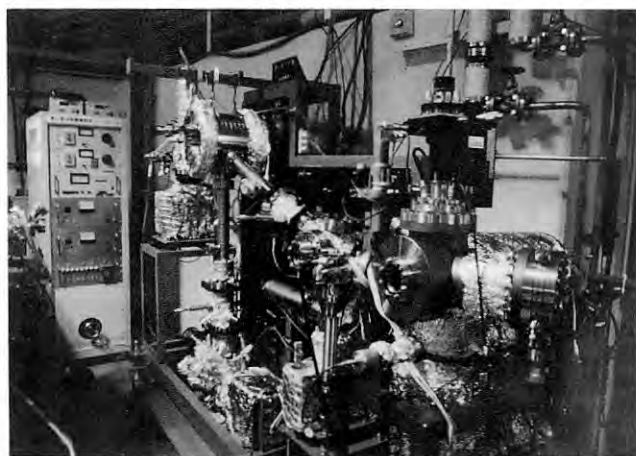


Fig. 6 An outlook of the 1 m Seya-Namioka monochromator joined with a photoelectron spectrometer (BL-7B).

BL-7C

Branch beam line 7C was constructed for X-ray spectroscopy and X-ray diffraction experiments by KEK-PF and is now partly available for many users. The branch line comprises two beryllium windows (12.2 m), a shutter which can stop γ -rays (12.8 m), a slit system (15.4 m), a double-crystal monochromator (16.3 m), and a beryllium and Kapton window assembly (21 m); distances are measured from the source point. The former beryllium windows separate the ultra-high vacuum of the front end (10^{-9} Torr) from the low vacuum of the branch line (10^{-2} Torr); the latter separates the branch line vacuum from air. The horizontal acceptance of this branch line is 4 mrad.

The monochromator was constructed based on the same design as that of BL-4C,¹⁾ which can keep the exit beam position unchanged when the energy of X-ray beam is changed. Silicon (111) flat crystals were installed to monochromatize X-ray beams of energy in the range from 4 to 21 keV. The shape of the cam was determined with an NC-milling machine and finally filed so that the movement of the exit beam position was less than 30 μ m for scattering angles between 5 and 50°. However, a test showed that the X-ray beam moved vertically by 0.7 mm. This movement was due to (1) a difference in the incident angles of the laser and X-ray beams, (2) a misalignment of the crystal position, (3) an inaccuracy of the cam shape, and (4) a change in the lattice parameter of the first crystal irradiated by a white X-ray beam. Especially the last two points are serious.

The cam is scheduled to be modified during the summer shut-down period in 1986, and the focusing of the X-ray beam by a sagittally bent second crystal will be tested in the near future.

Reference

- 1) Photon Factory Activity Report 1983/84 p.V-2 (1984).

BL-1A

In Beam Line 1, a significant improvement was achieved only at the branch line BL-1A during this year. We focus here on developments regarding this branch line. Figure 7 shows an overhead view of BL-1A. The main points of development are as follows:

- (1) A monochromatized beam from the GCM (Grating/ Crystal Monochromator) in combination with a focusing system comprising a toroidal mirror (front mirror) and a plane mirror (rear mirror) became available for photoemission spectroscopy in the VUV region.

- (2) An improvement in the monochromatized beam brightness was achieved by using parabolic mirrors instead of a toroidal mirror and a plane mirror. The resolving power ($E/\Delta E$) of the monochromator was measured to be about 570 by a gas-absorption experiment using Kr $M_{4,5}$.

- (3) A multi-functional surface-analysis system comprising an analysis chamber equipped with XPS, AES, LEED, LEELS etc and a sample preparation chamber was connected to the experimental station; then, an oxidation process analysis of

GaAs surfaces was performed with the monochromatized VUV beam for the first time.

Judging from the results of Au 4f and 5d photoemission spectra taken with a double-pass CMA on an evaporated Au film, photons with energies between 30 and 220 eV were useful for photoemission spectroscopy from the viewpoint of brightness and energy resolution in the case of a 1200 lines/mm plane grating. The beam size at the end station was measured to be 0.8 mm (vertical) \times 4 mm (horizontal).

When the direct slit which is located in front of the front mirror (17 m from the source point) is completely opened, the brightness of the SR beam increases drastically without reducing the energy resolution of the beam very much. Judging from the Au 4f FWHM (1.1 eV) measured in the same analysis chamber equipped with the double pass-CMA, the brightness of the beam is several times higher than that obtained at BL-11A at a photon energy of 120 eV.

The light vector of synchrotron radiation was measured during a comparison with the BL-1A construction line by using a theodolite and five pinholes placed in front of the front plane mirror. It was found that the SR vector was not exactly lined-up with the construction line. The discrepancy between the source point and the extended construction line was estimated to be about 2 cm. This discrepancy will be corrected in due course.

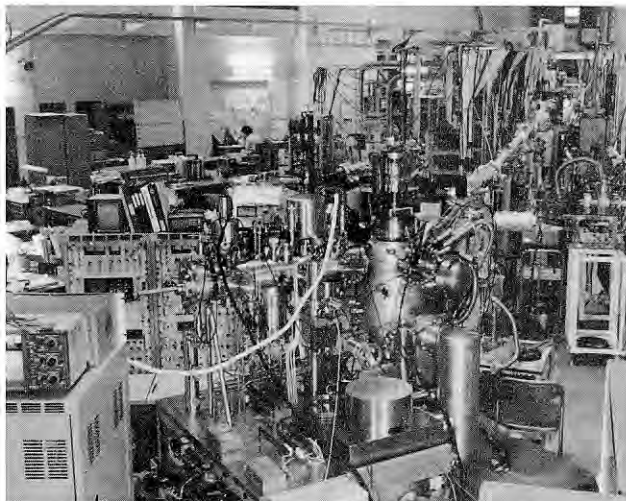


Fig. 7 An overhead view of BL-1A.

Beam Line 2

Soft X-ray radiation emitted from a 60 period permanent magnet undulator is available at beam line BL-2 which now has two branch beam lines, a straight and a deflection branch, with three experimental stations being operated in a time-sharing manner. Undulator radiation has a tunable spectral distribution comprising quasi-monochromatic harmonics which are the results of the interference of the radiation emitted through successive undulations of each electron in a periodic magnetic field. It has a high source brightness, being emitted within a narrow opening angle which is axially symmetric in an ideal case. The first harmonic of the undulator

radiation can be tuned over a photon energy range between 400 and 1000 eV by varying the gap width between the undulator magnets and the energy of associated higher harmonics extends to several keV region. The fractional bandwidth of the quasi-monochromatic first harmonic was observed to be $1/20 - 1/14$, slightly varying with an increasing gap width. The wavelength tunability of the fundamental harmonics was also well established in accordance with its dependence on the K-parameter; this corresponds to the peak magnetic field of the undulator, and was finely calibrated for the gap width. A SiC mirror coated with platinum deflects undulator radiation to the deflection branch while the straight branch becomes operational by removing the mirror from the beam axis. The photon flux at the peak of the first harmonic was observed to be 2×10^{11} photons/sec·mA·1%bandwidth after being reflected at a glancing angle of 2° by the mirror. Therefore, the flux integrated over the first harmonic region was estimated to be 2×10^{14} photons/sec for a storage ring current 200 mA when the peak of the first harmonic is tuned to 400 eV. The corresponding power density of the first harmonic is about 10 mw/mm^2 at a distance of 25 m from the center of the undulator. These values will be considerably increased by improving the storage-ring operation with low-emittance beam optics.

The straight branch has a vacuum-compatible double-crystal monochromator with a constant exit beam height in which a pair of synthetic InSb crystals ($2d = 7.4806 \text{ \AA}$) are mounted for making use of the higher harmonic components of the undulator radiation covering the photon energy range higher than 1.7 keV. The monochromator was fabricated in FY 1985 under joint collaboration between LSI Research and Development Laboratory, Mitsubishi Electric Corporation, and the synthetic InSb crystal was supplied by Research and Development Center, Toshiba Corporation (as a part of another joint collaboration). The incident glancing angle of the crystal can be mechanically scanned from 7 to 80° . Because of the narrow opening angle of undulator radiation, a highly efficient monochromatization can be achieved in this energy region only by means of simple double-reflection without any additional focussing element. The strong background gamma-radiation (inevitably accompanied by undulator radiation from electron storage ring) is stopped by a 480-mm thick lead block, while undulator radiation is separated from the gamma-radiation by double reflection and brought into an experimental chamber.

The deflection branch, now free from the gamma-ray problem owing to the first mirror reflection, has a 10-meter grazing incidence monochromator which was previously installed at BL-12C and has been transferred to the present branch in order to cover the tuning range of the first, second and third harmonics. A quasi-Rowland circle mounting with a fixed incidence angle of 89° was adopted for the monochromator in order to make a high-resolution soft X-ray spectroscopic measurements in this photon energy region. When a grating with a groove density of 1200 lines/mm and 20 \mu m slits is used, the constant wavelength resolution is 0.016 \AA and the output flux of about 10^{10} photons/sec can be expected at present for the first harmonic peak

tuned at 400 eV. Thermal resistant replicas of mechanically ruled concave gratings were supplied by Central Research Laboratory, Hitachi Ltd*. To this experimental station belongs a UHV chamber for the spectroscopy of pure metals with a sample preparation system which was fabricated in FY 1984 under joint collaboration with the above-mentioned laboratories of Hitachi and Mitsubishi.

As a main part of a soft X-ray microscope, a high vacuum compatible optical bench with a high-precision linear translator was installed upstream of the deflection branch of the grating monochromator. Condenser zone plates and pinholes can be mounted independently in a vacuum at laterally adjustable stages on the translator. Once a zone plate and a pinhole are both aligned just on the beam axis, the distance between them can be scanned through the translator to make undulator radiation monochromatized in an appropriate bandwidth for contrasted soft X-ray microscopy. However, the transmission efficiency and wavelength resolution of the system comprising the zone plate and pinhole are rather lower at present than expected because of a poor optical matching between the system and undulator radiation. They are both limited by the large size of the image on the focal plane of the condenser zone plate. In order to improve the efficiency and resolution without any loss of intensity, it is necessary to prepare a zone plate fabricated with a shorter focal length and to await the success of low-emittance operation of the storage ring. The microscope and the grating monochromator can ordinarily be operated in a time-sharing mode by removing or inserting vacuum pipes between them.

BL-10B

A beam-position monitor was installed in February 1986 in order to detect any vertical SR beam movement in the front slit box located upstream from the monochromator (21.4 m from the beam line source point). The position monitor consists of a pair of slit-blades and a signal-treating circuit, and measures photo-electron currents produced by the X-ray beam hitting the blades (Fig. 8). The magnitude of the electron current was found to be between 0.2 and 0.4 \mu A

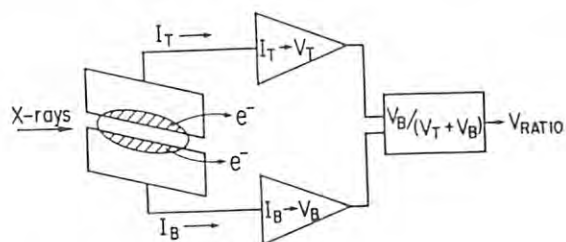


Fig. 8 Schematic diagram of the beam position monitor at BL-10B.

*When one wants to purchase the same gratings, it is only necessary to prepare blanks for replication with the same radius of curvature and the size appropriate to own demands.

for each blade at a stored 2.5 GeV electron beam of 150 mA. The beam position is expressed as the current ratio R observed at the two slit-blades. The movement Δh is given by

$$\Delta h = \alpha R \text{ with } \alpha = 4.7 \text{ mm and } R = I_B / (I_T + I_B),$$

where I_T and I_B are electron currents measured at the top and bottom blades, respectively, and α is a proportional constant for calculating the positional change from the change in R. α is determined from a change in R when the slit-blades are moved by a known distance with a fixed separation; a good linearity is obtained for a separation of ± 1 mm around $R = 0.5$. The minimum detectable positional change is about 5 μm . This beam-position monitor does not disturb the X-ray beam.

Figure 9 shows the R value and the beam current of the storage ring as a function of time (recorded from 9:00 on March 5th to 9:00 on March 6th 1986). A ratio $R = 1.0$ means that the branch beam line shutter is closed. Two types of movements of the beam heights can be seen in this figure. One is a 0.2-mm beam-height change continuing for 40 minutes every five hours. It is caused by the supply of liquid He into the superconducting vertical wiggler. However, the change cannot be detected thereafter, probably because of the improvement of the wiggler system. The other type of movement is such that the beam height changes by 0.4 mm in a one-day cycle with the highest value being at 14:00 and the lowest value at 6:00. It is likely that the beam height is affected by a temperature-induced distortion of the building.

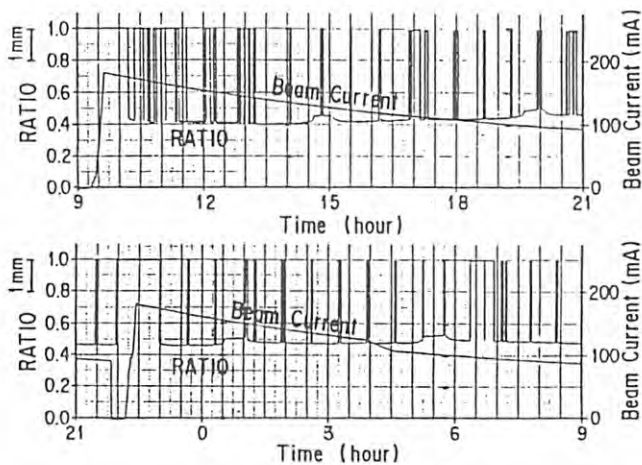


Fig. 9 Change in the beam position measured as a current ratio of the two slit-blades.

BL-15B

BL-15B is an X-ray branch line and experiments using a high-speed X-ray topography camera¹⁾, a three-axis diffractometer²⁾ and other equipment can be performed. Figure 10 shows (broken lines) the plan view of the experimental hutch previously placed at this beam line. Its sizes are 3271(L) \times 3762(W) \times 3000(H) (mm³). It can accommodate only one experimental apparatus. In order to facilitate a replacement of the equipment, we have reconstructed the hutch (shown

in Fig.10 by solid lines). The sizes of the new one are 6078(L) \times 4688(W) \times 3000(H), sufficiently large to accommodate two apparatus. It takes only a few hours to replace one by the other. The new hutch has a window at the ceiling (shown by dotted lines in Fig. 10),

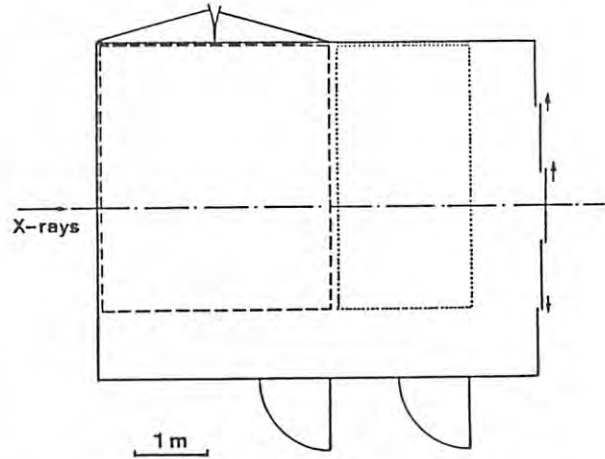


Fig. 10 A plan view of the experimental hutch at BL-15B. (broken lines: before reconstruction; solid lines: after reconstruction; dotted lines: the window at the ceiling).

through which parts of the apparatus and, if necessary, the apparatus itself can be taken out using a crane. The large sizes of the hutch allow one to do energy-dispersive small-angle scattering experiments.

Reference

- 1) S. Suzuki et al.: Nucl. Instr. and Meth. 227 (1984) 584
- 2) Photon Factory Activity Report (1982/83) V-32

Beam Line Safety

As more stations are running in their characteristic operation modes (which are very specific to the individual stations), more diversified types of programmed interlock procedures are in use. No accidents or serious failures related to the experimental area and the beam lines have occurred.

In FY 1985, self-contained interlock systems for beam lines BL-7, BL-8 and BL-9 were constructed and came into operation. BL-7 comprises three branch beam lines: two VUV lines by the Centre for Spectrochemistry, the University of Tokyo, in collaboration with KEK-PF, and one X-ray line by KEK-PF. Its interlock system was designed as an upgraded model system, and was fabricated by KEK-PF in collaboration with the Research Centre for Spectrochemistry. BL-9, currently utilizing two UHV-compatible x-ray branch beam lines, and BL-8 with one VUV branch beam line and two UHV-compatible x-ray lines, were constructed by NEC Corp., and by Hitachi Ltd., respectively, under the collaborative

supervision of KEK-PF. All these interlock systems are making full use of programmable controllers so as to accommodate logic for radiation safety and vacuum protection.

All interlock systems are being connected to a centralized monitoring system, from which individual operations of each system can be monitored and controlled. Logging data simultaneously collected for every beam line are periodically summarized, analyzed and distributed to the staff and those persons concerned, in order to provide information for smoother and safer operation and for further improvements of the beam lines.

2.2 Optics

Continuing efforts have been made to install a new monochromator and to improve the old ones at several of the branch beam lines.

BL-4B

This branch beam line has been used since 1983 for experiments using white X-rays. In April 1986, a monochromator system was installed. At the present time both monochromatic and white X-rays are available, depending on the needs of researchers. A control unit allows switching of the two modes by a vertical translation of monochromator crystals.

The monochromator system comprises a double-crystal monochromator and fore and back-X-ray slits, which are located at the distances of 17.2, 16.6, and 18.9 m from the beam line source point, respectively. The double-crystal monochromator is of an uniaxial type with a fixed distance between two crystals. The height of the out-going beam, therefore, changes as a function of the scattering angle of the monochromator. This monochromator has the following characteristics: (1) The crystal size is 125 (L) × 100 (W) mm, large enough to use a full incident beam having the horizontal size of 70 mm (4.5 mrad). (2) The crystals can be rotated with the accuracy of 4" of arc on every 1 degree rotation and 10" on a full rotation. (3) The minimum angle of rotation is 0.05" per pulse. A piezo-electric system is used for the fine adjustment of the first crystal. (4) Two flat Si(111) crystals are currently used within the energy range from 4 to 20 keV ($\sim 2 \times 10^{-4}$ in $\Delta E/E$). (5) The optical alignment of the monochromator can be made through a control unit, a Parallel I/O, and a microcomputer.

BL-4C

In order to increase the photon flux at the sample position by sagittally focusing the X-ray beam in the horizontal direction, a bent Si(111) crystal is used as the second crystal of the fixed-exit double crystal monochromator on BL-4C. As shown in Fig. 11 this crystal is diamond-shaped and has stiffening ribs on the back side in order to avoid any anticlastic bending (bending in the direction orthogonal to the direction of bending necessary for the sagittal focusing). Only the center rib (3-mm thick) is clamped to a metal support. The thickness of other ribs is 1 mm. Bending torques are applied at two apexes of the crystal. As summarized in Table 2, an intensity gain of 16 - 39 is obtained at the focus position (32.1 m from the source point) with a spot size of 4 mm × 1 mm. The smaller gain at higher energies is due to a detuning of the second crystal by undesired twists in the crystal along the plane of incidence. Continued efforts are being made to prepare a crystal which does not show any twisting by applied torques at two apexes.

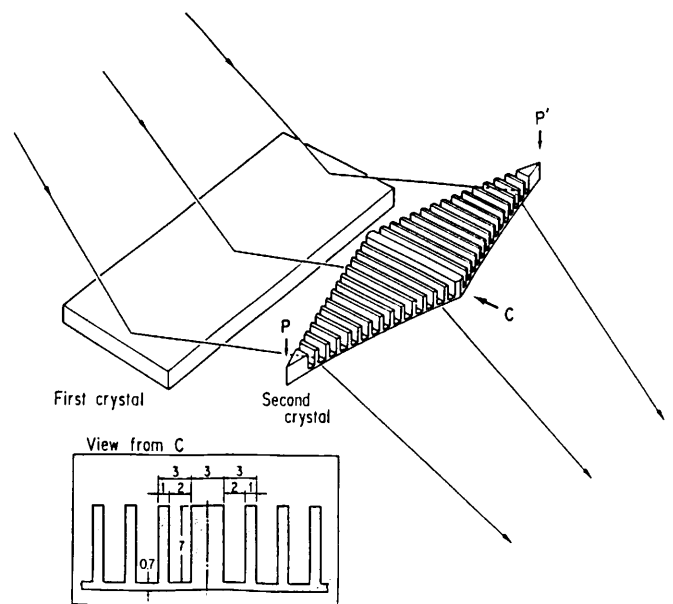


Fig. 11 A schematic view of the double-crystal monochromator with a sagittally focusing mechanism at BL-4C.

Table 2 Intensity gain by the sagittally focusing of the double-crystal monochromator at BL-4C.

Bragg angle (deg)	Photon energy (keV)	Intensity gain ($I_{\text{focused}}/I_{\text{unfocused}}$)
21.0	5.38	39
17.0	6.76	34
9.0	12.6	16

1.3 Summary of X-ray beam lines and optics

Branch Beam Line	Horizontal Acceptance Angle (mrad)	Typical Beam Size (H mm × V mm)	Photon Flux at Sample Position	Monochromator (Crystal)	Energy Resolution ($\Delta E/E$) × 10 ⁻⁴	Energy Range (keV)	Mirror	Line Vacuum (Gas)
BL-4A	6	50 × 5		None		4 ~ 35	None	Vacuum
BL-4B	4.5	50 × 5		Double Crystal Si (111)	~ 2	4 ~ 35	None	Vacuum
BL-4C	4	4 × 1		Double Crystal Si (111) Sagittal Focusing	~ 2	4 ~ 20	None	Vacuum
BL-6A ₁	0.1	10 × 3		Plane (111)	7.5	8 ~ 17		Vacuum
BL-6A ₂	4	2.5 × 1		Bent Si (111) ($\alpha = 0, 6.0^\circ, 7.8^\circ, 9.5^\circ, 11.4^\circ, 13.7^\circ, 16.5^\circ$)		5 ~ 25	Bent Plane Fused Quartz	Vacuum
BL-6B (6 if necessary)	4			None		4 ~ 30		Vacuum
BL-6C ₁ (4 in future)	0.5	10 × 5		None		8 ~ 30		Vacuum
BL-6C ₂	0.5	5 × 5		Channel-Cut Ge (111)	7.5	8 ~ 12		Vacuum
BL-7C	4	8 × 1	$4 \times 10^9/7\text{mm}^2$ (8 keV, 100 mA)	Si (111) Double Crystal	2	4 ~ 20	None	Vacuum
BL-10A	1	10 × 3		Si (111), Si (220) Ge (111), InSb (111) Quartz (100), PG (002) Curved Si (111) ($\alpha \sim 4^\circ, 8^\circ$)	50 ~ 5	5 ~ 25	None	Helium
BL-10B	2	8 × 1	$3 \times 10^8/7\text{mm}^2$ (10 keV, 100 mA) with Si (311)	Channel-Cut Si(311) Double Si (111) Double Si (220)	1	6 ~ 30 3.5 ~ 15 5.5 ~ 25	None	Vacuum
BL-10C	4	6 × 1.5	$\sim 10^{10}/9\text{mm}^2$ (8 keV, 100 mA)	Double Crystal Si (111) Fixed Beam Position	2	4 ~ 10	Bent Cylinder	Helium
BL-14A	1.28 (Vertical)	5 × 38		Double Si (111) Double Si (331) Double Si (553)	2	5.1 ~ 19.1 12.9 ~ 48 22.7 ~ 84.5	Bent Cylinder for Vertical Focusing, Pt-cated Fused Quartz	Vacuum (line) He(mono-chromator)
BL-14B	2.2	5 × 30		Double Si (111) Double Si (220) Double Si (311)	2	5.2 ~ 57	Sagittal Focusing	Vacuum
BL-14C	1.3	10 × 40		Double Si (111)	2	5.5 ~ 43	None	Vacuum
BL-15A	?	2.6 × 1.3	$9 \times 10^{10}/6\text{mm}^2$ (8.0 keV, 150 mA)	Curved Ge (111) ($\alpha=8.0^\circ$)	~ 10	5.6 ~ 12.4	Cylinder, Fused Quartz	Vacuum and He
BL-15B	0.14	5 × 5		None		3.5 ~ 34	None	Vacuum
BL-15C	2	60 × 6		None		4 ~ 35	None	Vacuum

1.4 Summary of VUV/soft X-ray beam lines and optics

Branch Beam Line	Monochromator						Pre - Mirrors							Refocusing Mirrors						
	Monochromator	Grating (Crystal)	Groove Density (λ/mm)	Blaze (A)	Resolution	Wavelength Range (Å)	Type	Radius of Curvature (mm)	Angle of Incidence	Material	Coating Material	Dimensions (mm)	Horizontal & Vertical Acceptance (mrad)	Type	Radius of Curvature (mm)	Angle of Incidence	Material	Coating Material	Dimensions (mm)	Beam Size (mm)
BL-1A	Grating/Crystal Monochromator	Au-Coated Original InSb(111) Si(111)	1200 2d=7.4806 Å 2d=6.27064 Å		$\lambda/\Delta\lambda \sim 2000^*$	2 ~ 2000	Paraboloidal		89°	Fused Quartz	Pt	500 ^h ×80 ^w ×50 ^t	4.0 ^h ×0.5 ^v	Paraboloidal		89°	Fused Quartz	Pt	500 ^h ×80 ^w ×50 ^t	4 ^h ×1 ^v
BL-1B	Filtered White						Plane		88° ~ 89°	SiC			1.2 ^h ×4.0 ^v						19 mmφ	
BL-1C	Filtered White						Toroidal		86°	Fused Quartz	Pt		2.0 ^h ×4.0 ^v						2 ^h ×10 ^v	
BL-2A	Double Crystal Monochromator with Constant Exit Beam	InSb(111)	2d=7.4806 Å			7.3 ~ 4.0														
BL-2B ₁	Fresnel Zone Plate Microscope					30 ~ 15	Plane	—	88°	SiC	Pt	120 ^h ×60 ^w ×15 ^t	—							
BL-2B ₂	10m Grazing Incidence Monochromator with Fixed Incidence Angle of 89°	Hitachi Au-Coated Replica (pyrex)	2400 1200	8 16	$\Delta\lambda=0.004 \text{ Å}^*$ $\Delta\lambda=0.008 \text{ Å}^*$ for 10μ-10μ Slits	6 ~ 25 6 ~ 50	Plane Concave Concave	— 8903 7527	86.85° ~ 88.83° 89° 89°	SiC Pyrex Pyrex	Pt Pt Pt	120 ^h ×60 ^w ×15 ^t 90 ^h ×15 ^w ×15 ^t 90 ^h ×15 ^w ×15 ^t	0.14 ^h ×0.4 ^v							
BL-11A (2GH)	Grasshopper Mark VII 2m Grazing Incidence Fixed Incidence Angle of 88°	Hitachi Au-Coated Replica (pyrex)	2400 1200	16.6 33.3	$\Delta\lambda=0.02 \text{ Å}^*$ $\Delta\lambda=0.04 \text{ Å}^*$ for 10μ-10μ Slits	10 ~ 145 10 ~ 290	Spherical Spherical	360000 28000	88° 88°	Fused Quartz Fused Quartz	Pt Au	400 ^h ×170 ^w ×40 ^t 300 ^h	1.3 ^h ×0.4 ^v	Bending Cylinder	R~3000	89°	Pyrex	Pt	220 ^h ×24 ^w ×6 ^t	8 ^h ×0.3 ^v
BL-11B (DXM)	Jumbo Jr. Double Crystal Monochromator	Ge(111) InSb(111) Beryl(1010)	2d=6.53 Å 2d=7.4806 Å 2d=15.9 Å		$\Delta E=1\text{eV at } 2\text{KeV}$ $\Delta E=0.8\text{eV at } 2\text{KeV}$ $\Delta E=0.6\text{eV at } 1\text{KeV}$	2.7 ~ 6.2 3 ~ 7 8 ~ 16	Bending Cylinder	ρ=300 R~950000	89°	Fused Quartz	Pt	580 ^h ×140 ^w ×30 ^t	4.0 ^h ×0.6 ^v							8 ^h ×1 ^v
BL-11C (SSN)	1m Seya-Namioka Constant Deviation of 70°	Hitachi Au-Coated Replica Hitachi Al-Coated Replica	2400 1200 1200	785 785 785	$\Delta\lambda=0.3 \text{ Å at } 500 \text{ Å}$ for 50μ-50μ Slits	400 ~ 1500 400 ~ 3000	Plane Concave	— 5600	77.5° 42.5°	SiC Fused Quartz	none Pt	250 ^h ×100 ^w ×40 ^t 100 ^h ×100 ^w ×20 ^t	4.8 ^h ×3.0 ^v	Toroidal	ρ=2000 R=125	72.5°	Pyrex	Au	90 ^h ×50 ^w ×10 ^t	~1φ
BL-11D (CDM)	2m Grazing Incidence Constant Deviation Monochromator α + β = 154°	B & L Hitachi Au-Coated Replica	2400 1200 600	32 116 460	$\lambda/\Delta\lambda \sim 1700$ for 25μ-25μ Slits	80 ~ 150 120 ~ 300 240 ~ 600	Cylindrical Plane Concave	ρ=750 — 4000	86° 86° 86°	SiC Fused Quartz BK-7	Pt Au Au	400 ^h ×60 ^w ×40 ^t 50 ^h ×40 ^w ×10 ^t 50 ^h ×40 ^w ×10 ^t	1.5 ^h ×2.0 ^v	Toroidal	ρ=400 R=3100	77°	BK-7	Au	60 ^h ×40 ^w ×10 ^t	0.5 ^h ×0.5 ^v
BL-12A (GSN)	1m Seya-Namioka Constant Deviation of 70°	B & L Au-Coated Replica	2400 1200	508 536	$\Delta\lambda=0.4 \text{ Å at } 500 \text{ Å}$ for 100μ-100μ Slits	350 ~ 1000 350 ~ 2000	Cylindrical Concave	ρ=1850 6250	80° 45°	SiC Fused Quartz	none Pt	250 ^h ×200 ^w ×40 ^t 100 ^h ×20 ^w ×20 ^t	2.4 ^h ×1.5 ^v	Plane Toroidal Plane	— ρ=340 R=2000 —	80° 70° 80°	Pyrex Pyrex Pyrex	Pt Pt Pt	40 ^h ×40 ^w ×10 ^t 40 ^h ×40 ^w ×10 ^t 40 ^h ×40 ^w ×10 ^t	~1φ
BL-12B (6VOPE)	6.65m Normal Incidence Off-Plane Eagle Mounting	B & L Pt-Coated Replica B & L Os-Coated Replica Hyperfine Os-Coated Replica	1200 1200 4800	1500 5500 900	$\lambda/\Delta\lambda=2.5 \times 10^5 \text{ Å}$ at ~ 800 Å	400 ~ 2500	Plane Concave Concave	— 4321 2188.5	80° 35° 45°	SiC Pyrex Pyrex	none Pt Pt	280 ^h ×100 ^w ×40 ^t 110 ^h ×20 ^w ×20 ^t 110 ^h ×20 ^w ×20 ^t	5.0 ^h ×3.6 ^v							

* nominal value

7. V-32, VI-97, VI-98 in (A)
- (r) Precision X-ray optics.
1. Goniometer assembly dedicated to precision diffraction study such as double-, triple-, and more than triple-crystal diffractometry and topography.
 2. Microcomputer control system.
NaI scintillation detector system.
SSD and MCA.
Ionization chamber for monitoring.
Room temperature controller.
Experimental table with air springs
 3. 1 arc sec accuracy for full rotation.
0.1 arc sec accuracy within 6° using tangential bar system.
Employs super-precision rotation mechanism with elastic torsion and PZT.
 4. Detection of polarization rotation under magnetic diffraction condition.
Structure analysis of epitaxial layer/substrate interfaces with standing wave method. VI-188, VI-189
 5. BL-15C.
 6. T. Ishikawa
 7. V-33 in (A)

Soft X-ray and VUV

- (a) Gas phase angle resolved photoelectron spectrometer
1. Ultimate pressure 5×10^{-8} Torr.
Equipped with a conventional hemispherical electrostatic analyzer and with a position-sensitive parallel-plate electrostatic analyzer.
 2. Sample-gas inlet system.
 3. A sample gas is confined in a gas cell.
 4. The measurements of absolute intensity and polarization of synchrotron radiation from the undulator.
 5. BL-2, BL-12A.
 6. A. Yagishita
 7. V-42 in (A)
- (b) Heat-pipe chamber for photoabsorption measurements of free-metal atoms
1. Ultimate pressure 1×10^{-7} Torr.
The pressure difference between vapor column and differential pumping stage is $\sim 10^7$.
 2. Buffer gas inlet system.
 3. Heated up to about 1000°C .
 4. The measurements of photoabsorption cross sections for 3d electrons of Xe, Cs, and Ba.
 5. BL-11A.
 6. K. Ito
 7. V-41 in (A)
- (c) VUV and Soft X-ray Reflectometer
1. Equipped with a goniometer, insuring accurate incidence angle (30 sec)
Up to 89.4° incidence angle
Ease of optical alignment
Ease of sample exchange
High vacuum (2×10^{-9} Torr)
 - 2.
 3. Equipped with ports for vacuum evaporation.
 4. Optical constants of mirror materials.
Surface roughness.
5. BL-11A
6. T. Miyahara
7. V-41, VI-78 in (A)
- (d) UHV experimental chamber for absorption measurements II.
1. High vacuum (1×10^{-9} Torr)
Mounts up to 5 samples.
 2. Gas cell (160 mm in length)
Vacuum evaporator
Electron multiplier (R595).
 3. 190 mm I.D.
 4. Core level absorption in alkali halides and transition metal compounds.
M4,5 giant resonance absorption in $Z = 49-57$ elements.
Photoefficiency of photocathodes.
Lithography for resist polymer.
 5. BL-11A, BL-12C.
 6. H. Maezawa
 7. V-40, VI-73, VI-74, VI-76, VI-77, VI-79 in (A)
- (e) UHV experimental chamber for absorption measurements I.
1. Ultra-high vacuum (1×10^{-10} Torr)
Equipped with an electron-beam gun for evaporation of samples. Equipped with a quartz oscillator capable of being cooled to LNT.
 2. Sample holder with an adjustable linear motion, capable of being cooled to LNT.
 3. Designed mainly for very reactive metal samples.
 4. Absorption measurement of alkali metals, alkali metal alloys, and rare earth metals.
VI-114
 5. BL-11C, BL-11D.
 6. T. Miyahara
 7. VI-82 in (A)
- (f) Vacuum chamber for performance testing of grating monochromator
1. Equipped a 160 mm length gas cell with 10 mm diameter propylene windows.
 2. A sample-gas inlet system.
 - 3.
 - 4.
 5. BL-11A, BL-12C.
 6. H. Maezawa
 7. V-40 in (A)
- (g) Apparatus for ARPES experiment for solid state
1. Base pressure 5×10^{-11} Torr.
Equipped with a double-pass cylindrical mirror analyzer and with a hemispherical analyzer mounted on a two axis rotation mechanism
 2. Some equipments for sample preparation and characterization
Sample bank and transfer system
Sample gas inlet system
 - 3.
 4. Mainly for angle-resolved photoelectron spectroscopy (ARPES) of single crystals
VI-133, VI-135, VI-136
 5. BL-11D
 6. H. Kato
 - 7.

- (h) Multi-purpose chamber for gas phase experiments
 - 1. Ultimate pressure 1×10^{-7} Torr. Equipped with two turn tables notatable the incident light.
 - 2. Double-ion chamber.
 - 3.
 - 4. The measurements of absolute photoabsorption cross sections of C_3H_6 and C_4H_8 isomers.
 - 5. BL-12A
 - 6. A. Yagishita
 - 7. V-40 in (A)

- (i) Time-of flight spectrometer for photoion measurements
 - 1. Ultimate pressure 5×10^{-8} Torr. Electrostatic lenses satisfying the conditions of single-field space focusing for threshold electrons and double-field space focusing for ions.
 - 2. Furnace to evaporate alkali-and alkaliearth-metals.
 - 3.
 - 4. The measurements of single and double-photoionization cross sections of Ca and Sr.
 - 5. BL-12A
 - 6. A. Yagishita
 - 7. V-40 in (A)

PHOTON FACTORY ACTIVITY REPORT

1986

PHOTON FACTORY ACTIVITY REPORT 1986

#4

#4



NATIONAL LABORATORY FOR HIGH ENERGY PHYSICS, KEK